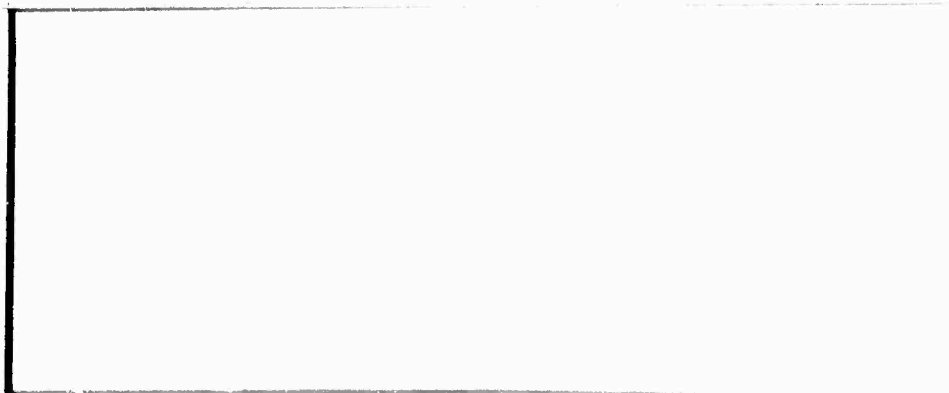


AD 728053

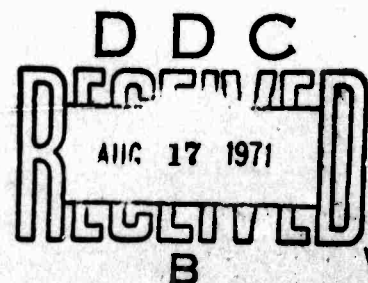
TECHNICAL REPORT



**CENTER FOR
MATERIALS SCIENCE AND ENGINEERING**

**Massachusetts Institute of Technology
Cambridge, Massachusetts 02139**

Reproduced by
NATIONAL TECHNICAL
INFORMATION SERVICE
Springfield, Va. 22151



**BEST
AVAILABLE COPY**

DOCUMENT CONTROL DATA - R&D

(Security classification of title, body of abstract and indexing annotation must be entered when the overall report is classified)

1. ORIGINATING ACTIVITY (Corporate author) Massachusetts Institute of Technology Cambridge, Mass.. 02139		2a. REPORT SECURITY CLASSIFICATION unclassified	
		2b. GROUP	
3. REPORT TITLE Structure and Property Control Through Rapid Quenching of Liquid Metals			
4. DESCRIPTIVE NOTES (Type of report and inclusive dates) Semi-annual Technical Report #2, (Jan. 1, 1971 - June 30, 1971)			
5. AUTHOR(S) (Last name, first name, initial) Grant, Nicholas J.; Pelloux, Regis M.N.; Flemings, Merton C; Argon, Ali S.			
6. REPORT DATE July 1, 1971		7a. TOTAL NO. OF PAGES 180	7b. NO. OF REFS
8a. CONTRACT OR GRANT NO. DAHC15 70 C 0283		8a. ORIGINATOR'S REPORT NUMBER(S)	
b. PROJECT NO. ARPA Order #1608			
c. Program Code #0D10		8b. OTHER REPORT NO(S) (Any other numbers that may be assigned this report)	
d.			
10. AVAILABILITY/LIMITATION NOTICES			
11. SUPPLEMENTARY NOTES		12. SPONSORING MILITARY ACTIVITY Advanced Research Projects Agency 1400 Wilson Blvd. Arlington, Virginia 22209	
13. ABSTRACT This report presents the results and accomplishments of the first year of a three year research program investigating the production of solid bars from rapidly quenched liquid metals. Steam atomization has been used to prepare coarse metal powders of a maraging steel VM 300, a nickel base alloy IN100 and cobalt base alloys. This atomization process can be used successfully with cobalt base alloys but does not appear to be suitable for the nickel base alloys. Improvements will have to be made to control the chemistry and the purity of the maraging steel coarse powders produced by steam atomization. Billets and solid bars have been produced by hot isostatic compaction, or by extrusion of coarse powders. The bond strength between metal powder particles prior to cold or hot working of the compacted bars is strongly dependent upon the presence of impurities such as oxygen, hydrogen and carbon. Hot isostatic compaction followed by extrusion gave the best results in terms of mechanical properties and homogeneity of the billets. The influence of cooling environments and cooling rates on the secondary dendrite arm spacings and the extent of microsegregation within the coarse powder particles has been studied in detail. The mechanical properties and the microstructures of the different alloys produced by the powder process are reported and compared to the properties of the commercially cast and wrought alloys having the same chemistry. In all cases, marked improvement in homogeneity has been achieved with equal or superior mechanical properties over the current commercial grades. (cont'd on page 2)			

14.	Abstract -con'd	LINK A		LINK B		LINK C	
		ROLE	WT	ROLE	WT	ROLE	WT
<p>A theoretical and experimental study of the role of the size, spacing and distribution of inclusions on ductility and mechanical properties has been undertaken. This study will set some guidelines for the cleanliness requirements of the alloys produced by the coarse powder process.</p> <p><u>Key Words</u></p> <p>Rapid Quenching Structure Control Segregation Control</p>							

INSTRUCTIONS

1. **ORIGINATING ACTIVITY:** Enter the name and address of the contractor, subcontractor, grantee, Department of Defense activity or other organization (corporate author) issuing the report.

2a. **REPORT SECURITY CLASSIFICATION:** Enter the overall security classification of the report. Indicate whether "Restricted Data" is included. Marking is to be in accordance with appropriate security regulations.

2b. **GROUP:** Automatic downgrading is specified in DoD Directive 5200.10 and Armed Forces Industrial Manual. Enter the group number. Also, when applicable, show that optional markings have been used for Group 3 and Group 4 as authorized.

3. **REPORT TITLE:** Enter the complete report title in all capital letters. Titles in all cases should be unclassified. If a meaningful title cannot be selected without classification, show title classification in all capitals in parenthesis immediately following the title.

4. **DESCRIPTIVE NOTES:** If appropriate, enter the type of report, e.g., interim, progress, summary, annual, or final. Give the inclusive dates when a specific reporting period is covered.

5. **AUTHOR(S):** Enter the name(s) of author(s) as shown on or in the report. Enter last name, first name, middle initial. If military, show rank and branch of service. The name of the principal author is an absolute minimum requirement.

6. **REPORT DATE:** Enter the date of the report as day, month, year, or month, year. If more than one date appears on the report, use date of publication.

7a. **TOTAL NUMBER OF PAGES:** The total page count should follow normal pagination procedures, i.e., enter the number of pages containing information.

7b. **NUMBER OF REFERENCES:** Enter the total number of references cited in the report.

8a. **CONTRACT OR GRANT NUMBER:** If appropriate, enter the applicable number of the contract or grant under which the report was written.

8b, 8c, & 8d. **PROJECT NUMBER:** Enter the appropriate military department identification, such as project number, subproject number, system numbers, task number, etc.

9a. **ORIGINATOR'S REPORT NUMBER(S):** Enter the official report number by which the document will be identified and controlled by the originating activity. This number must be unique to this report.

9b. **OTHER REPORT NUMBER(S):** If the report has been assigned any other report numbers (either by the originator or by the sponsor), also enter this number(s).

10. **AVAILABILITY/LIMITATION NOTICES:** Enter any limitations on further dissemination of the report, other than those

imposed by security classification, using standard statements such as:

- (1) "Qualified requesters may obtain copies of this report from DDC."
- (2) "Foreign announcement and dissemination of this report by DDC is not authorized."
- (3) "U. S. Government agencies may obtain copies of this report directly from DDC. Other qualified DDC users shall request through _____."
- (4) "U. S. military agencies may obtain copies of this report directly from DDC. Other qualified users shall request through _____."
- (5) "All distribution of this report is controlled. Qualified DDC users shall request through _____."

If the report has been furnished to the Office of Technical Services, Department of Commerce, for sale to the public, indicate this fact and enter the price, if known.

11. **SUPPLEMENTARY NOTES:** Use for additional explanatory notes.

12. **SPONSORING MILITARY ACTIVITY:** Enter the name of the departmental project office or laboratory sponsoring (paying for) the research and development. Include address.

13. **ABSTRACT:** Enter an abstract giving a brief and factual summary of the document indicative of the report, even though it may also appear elsewhere in the body of the technical report. If additional space is required, a continuation sheet shall be attached.

It is highly desirable that the abstract of classified reports be unclassified. Each paragraph of the abstract shall end with an indication of the military security classification of the information in the paragraph, represented as (TS), (S), (C), or (U).

There is no limitation on the length of the abstract. However, the suggested length is from 150 to 225 words.

14. **KEY WORDS:** Key words are technically meaningful terms or short phrases that characterize a report and may be used as index entries for cataloging the report. Key words must be selected so that no security classification is required. Identifiers, such as equipment model designation, trade name, military project code name, geographic location, may be used as key words but will be followed by an indication of technical context. The assignment of links, rules, and weights is optional.

For period - Jan. 1, 1971 to June 30, 1971

Semi-Annual Technical Report No. 2

STRUCTURE AND PROPERTY CONTROL THROUGH
RAPID QUENCHING OF LIQUID METALS

Sponsored by
Advanced Research Projects Agency
Contract No.: DAHC15 70 C 0283

ARPA Order No.: 1608
Program Code No.: OD10

Contractor:

Massachusetts Institute of Technology
Cambridge, Mass. 02139

Principal Investigator:

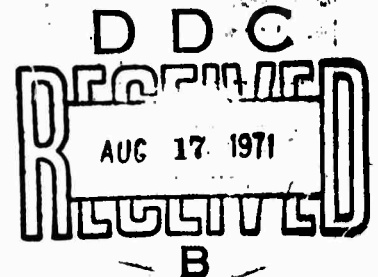
N. J. Grant
(617) 864-6900 Ext. 5638

Effective date of Contract: June 22, 1970
Contract Expiration Date: June 21, 1972

Total Amount of Contract: \$470,300

ARPA Order No. 1608

The views and conclusions contained in this document are those of the authors and should not be interpreted as necessarily representing the official policies, either expressed or implied, of the Advanced Research Projects Agency or the U.S. Government.



Semi-Annual Technical Report #2

TABLE OF CONTENTS

	<u>Page number</u>
TASK I PROCESSING OF ALLOYS	
I. Introduction	1
II. Experimental Work	2
A. Melting & Atomization	2
B. Powder Characterization	3
1. IN-100	3
2. VM-300	4
3. Cobalt Base Superalloy	7
C. Cleaning	8
D. Powder Consolidation	8
1. Objectives	8
2. Hot Isostatic Pressing Runs	9
3. HIP Microstructures	10
4. Extrusion Runs	13
5. Extrusion Microstructures	13
III. Conclusions	15
Tables	16
Figures	29
TASK II SOLIDIFICATION RESEARCH	
Abstract	48
Introduction	49
I. Effect of Cooling Rate on Structure of Maraging 300 Alloy	50
II. Analysis of Structure & Heat Flow of Atomized Powders	53
III. Melting, Casting and Structures of Rapidly Solidified Rods	60
IV. Bonding Characteristics of Rapidly Solidified Rods and Mechanical Properties of Billets Consolidated from these Rods	61

TASK II .con'd

V. 'Conclusions	66
References	67
Tables	68
Figures	73

TASK III	THERMOMECHANICAL TREATMENTS	91
-----------------	------------------------------------	-----------

I. Metallography & Mechanical Properties of 300 Grade Maraging Steels	92
Introduction	92
Heat Treatment	93
Tensile Properties	93
Fatigue Testing	95
Impact Testing	95
Fracture Toughness Testing	96
Tables	97
Figures	101
II. Hot Plasticity of IN-100 Processed by Powder Metallurgy	106
Introduction	106
Stress-Rupture Testing	106
Tables	108
Figures	109
III. Microstructure & Mechanical Properties of Cobalt Alloys	110
Introduction	110
Heat Treatment & Ageing of Cobalt Alloys	111
Thermomechanical Treatment	111
Mechanical Properties	112
Microstructure	113
References	114
Tables	115
Figures	120

TASK IV	MICROSTRUCTURE AND MECHANICAL BEHAVIOR OF COMMERCIAL AND HIP MARAGING STEELS	124
----------------	---	------------

TASK IV con'd

Introduction	124
Part I. Tensile Ductility	125
1.1 Hole Formation from Inclusions	125
1.2 Hole Formation from Widely Separated Large Inclusions	126
1.3 Hole Formation between Interacting Particles of Uniform Size	129
1.4 Hole Formation between Interacting Particles of Different Size	129
II. Experimental Procedure	130
2.1 Material Used	
2.2 Specimen Shape	130
III. Experimental Results	133
3.1 Tensile Behavior	133
3.2 Microstructure	133
3.3 Tensile Ductility	135
3.3.1 Commercial Vascomax 300 Alloy	135
3.3.2 Maraging 300 HIP Alloy with Large Hollow Inclusions	136
IV. Discussion of Results	136
Part II. Stress Corrosion Cracking Experiments	139
I. Design of the Specimen	139
II. Experimental Apparatus	142
III. Experimental Results	142
References	143
Tables	145
Figures	153

LIST OF FIGURES

Figure No.Title

1. IN-100. Heat No. 199, as atomized, steam. 1X.
2. VM-300. Heat No. 218, cleaned 5 cycles + 1600°F, H₂ anneal. Size fractions l. to r. -4/+5, -8/+10, -16/+18, and -25/+30. 1X.
3. VM-300. Heat No. 218, -4/+5 mesh (4.3 mm) unetched l, etched r. Dendrite arm spacing 6.4 microns. 500X.
4. VM-300. Heat No. 218, -8/+10 mesh (2.0 mm) unetched l, etched r. Dendrite arm spacing 6.6 microns. 500X.
5. VM-300. Heat No. 218, -16/+18 mesh (1.0 mm) unetched l, etched r. Dendrite arm spacing 6.6 microns. 500X.
6. VM-300. Heat No. 218, -25/+30 mesh (0.6 mm) unetched l, etched r. Dendrite arm spacing 5.2 microns. 500X.
7. Cobalt-Hafnium Alloy. Heat No. 185, as atomized, no melt additions, left. Heat No. 217, cleaned, Si & B melt additions, right. 1X.
8. Cobalt-Hafnium Alloy. Heat No. 185, left D.A.S. 3.1 microns; Heat No. 217, right, D.A.S. 2.8 microns. Etched. 500X.
9. IN-100. Federal Mogul, -60 mesh. HIP @ 2100°F, 15,000 psi, 2 hours. As pressed. Etched. 500X.
10. IN-100. Federal Mogul, -60 mesh. HIP @ 2200°F, 15,000 psi, 2 hours. As pressed. Etched. 500X.
11. IN-100. Federal Mogul, -60 mesh. HIP @ 2320°F, 29,500 psi, 2 hours. As pressed. Etched. 500X.
12. IN-100. Homogeneous Metals, -20/+40 mesh. HIP @ 2000°F, 25,000 psi, 2 hours. As pressed. Etched. 500X.
13. IN-100. Homogeneous Metals, -20/+40 mesh. HIP @ 2000°F, 25,000 psi, 2 hours + 2100°F solution, 4 hours. A.C. Etched. 500X.
14. IN-100. Homogeneous Metals, -20/+40 mesh. HIP @ 2000°F, 25,000 psi, 2 hours + 2200°F solution, 4 hours. A.C. Etched. 500X.

LIST OF FIGURES

<u>Figure No.</u>	<u>Title</u>
15.	IN-100. Homogeneous Metals, -20/+40 mesh. HIP @ 2300°F, 25,000 psi, 2 hours. As pressed. Etched. 500X.
16.	IN-100. Homogeneous Metals, -20/+40 mesh. HIP @ 2300°F, 25,000 psi, 2 hours + 2200°F solution, 4 hours. A.C. Etched. 500X.
17.	IN-100. Homogeneous Metals, -20 mesh. HIP @ 2300°F, 15,000 psi, 1 1/4 hours. As pressed. Unetched. 100X.
18.	IN-100. Homogeneous Metals, -20 mesh. HIP @ 2300°F, 15,000 psi, 1 1/4 hours + 2300°F solution, 4 hours. A.C. Unetched. 100X.
19.	VM-300. IMT 136, -4/+14 mesh. Cleaned. HIP @ 2300°F, 25,000 psi, 2 hours. As pressed. Etched. 100X.
20.	VM-300. IMT 137, -4/+14 mesh. Cleaned. HIP @ 2000°F, 25,000 psi, 2 hours. As pressed. Etched. 100X.
21.	VM-300. Homogeneous Metals, -20 mesh. HIP @ 2300°F, 14,500 psi, 1 hour. As pressed. Etched. 100X.
22.	VM-300. Nuclear Metals, -35 mesh. HIP @ 2200°F, 14,500 psi, 1 hour. As pressed. Etched. 100X.
23.	MAR M 509. IMT 111, -8/+14 mesh, cleaned. HIP @ 2175°F, 15,000 psi, 1 hour. As pressed. Etched. 100X.
24.	MAR M 509. IMT 111, -8/+14 mesh, cleaned. HIP @ 2175°F, 15,000 psi, 1 hour. As pressed. Interparticle boundaries. Etched. 500X.
25.	MAR M 509 "+". IMT 112, -8/+14 mesh, cleaned. HIP @ 2175°F, 15,000 psi, 1 hour. As pressed. Etched. 100X.
26.	MAR M 509. IMT 111, -4/+8 mesh, cleaned. HIP @ 2300°F, 15,000 psi, 1 hour. As pressed. Etched. 100X.
27.	Cobalt-Hafnium Alloy. IMT 217, -4/+14 mesh, cleaned. HIP @ 2100°F, 14,500 psi, 1 hour. As pressed. Etched. 100X.
28.	MAR M 509 "+". IMT 112, -4/+8 mesh, cleaned. HIP @ 2100°F, 14,500 psi, 1/2 hour. As pressed. Etched. 100X.

LIST OF FIGURES

<u>Figure No.</u>	<u>Title</u>
29.	IN-100. HIP compact No. 10, Table III. Extruded 14.3 x @ 2000°F. As extruded. Longitudinal section. 100X.
30.	VM-300. IMT 148. -4/+35 mesh cleaned and H ₂ annealed. Extruded 10.5 x @ 2050°F. As extruded. Longitudinal section. 100X.
31.	VM-300. HIP compact No. 11, Table III. Extruded 14.3 x @ 2000°F. As extruded. Longitudinal section. 100X.
32.	VM-300. Homogeneous Metals. -20 mesh. Extruded 14.3 x @ 2000°F. As extruded. Longitudinal section. Etched. 100X.
33.	VM-300. HIP compact No. 13, Table III. Extruded 11.5 x @ 2000°F. As extruded. Longitudinal section. Etched. 100X.
34.	VM-300. Nuclear Metals -35 mesh. Extruded 11.5 x @ 2000°F. As extruded. Longitudinal section. Etched. 100X.
35.	MAR M 509. HIP compact No. 12, Table III. Extruded 15.2 x @ 2000°F. As extruded. Longitudinal section. Etched. 100X.
36.	MAR M 509. HIP compact No. 12, Table III. Extruded 15.2 x @ 2000°F. As extruded. Longitudinal section. Etched. 500X.
37.	Cobalt-Hafnium Alloy. HIP compact No. 14, Table III. Extruded 16 x @ 2000°F. As extruded. Longitudinal section. Etched. 100X.
38.	MAR M 509 "+". HIP compact No. 15, Table III. Extruded 11.1 x @ 2000°F. As extruded. Longitudinal section. Etched. 100X.

TASK I

Processing of Alloys

I. INTRODUCTION

Technical background of the current project on structure and property control of alloys by utilization of the process step of rapid quenching of the liquid has been fully described in the introduction to Semi-Annual Technical Report No. 1, June to December 1970. The general process flow sheet for production of "structure and property controlled" material includes, in general, production of powder, either coarse or fine; cleaning, if the powder is coarse and was water quenched; canning, evacuation, and sealing; and finally consolidation by hot isostatic pressing, direct extrusion or hot isostatic pressing followed by extrusion ("double consolidation").

Choice of a process route for production of consolidated material generally implies "selection" of problems or "tradeoff" alternatives. Coarse powder technique for example, while cheap, entails exposure of liquid metal droplets to an oxidizing environment with significant effects on chemistry and morphology. Oxidized surfaces generally require cleaning before consolidation, and totally effective cleaning has proven to be difficult. On the other hand, fine powders produced by contemporary state of the art processes previously described¹ are expensive and may have their own problems such as oxygen, nitrogen and carbon surface contamination with consequent effects on interparticle bonding in the consolidation process. With fine powders in research scale lots "cross contamination" in production and handling is a very real problem and occurred in at least one case in the present program. Finally in the consolidation step, selection of hot isostatic pressing conditions, time, temperature, and pressure for full densification in general appears to require one or more iterations.

¹ Introduction to Semi-Annual Technical Report No. 1.

In the first year program, coarse powder techniques were applied to IN-100, a high strength nickel base superalloy; Vascomax 300, a high strength maraging steel, and cobalt base alloys. Process limitations for specific alloys became evident and experimental work aimed at process improvement was carried out. Cobalt base alloys were added to the program in the last half year to take advantage of promising earlier experience with steam atomization of these materials.

Supplementary consolidation of commercial fine powders was carried out in cases where coarse powder techniques did not produce "state of the art" powders. Results in the process step of consolidation of powders revealed that this operation requires careful consideration and analysis if the maximum potential of powder is to be realized. The chemistry of metal powders, particularly with respect to contaminants, both interior and surface, has been identified as critical to the microstructure of the consolidated powders.

II. EXPERIMENTAL WORK

A. Melting and Atomization

The melting and atomization equipment and arrangements used for coarse powder production at the start of the program and after improvement have been fully described.¹ One additional modification to the quench tank not previously reported was made which permitted the quench water level to be raised within 6 inches of the atomization point in argon atomization.

A summary of all melting and atomization runs carried out to date is given in Table I. From Heat No. 185 on, screen analysis was not carried out except to obtain specific size particles for chemical analysis. Emphasis in these later heats was primarily on metal chemistry.

The very high water quench experiment with maraging steel (VM-300) was carried out in Heat No. 218. Results are discussed later under Powder Characterization.

¹ Semi-Annual Technical Report No. 1.

Efficiency of the melting and tapping operation in maintaining alloy element levels and low oxygen level was defined by the results of Ht. No. 173 (maraging steel, VM-300) wherein the tundish nozzle metal stream was sampled with a chill mold during interrupted atomization. Chemistry results for this sample indicate that reactive alloy elements (Ti, Al) have maintained substantially their furnace melt values right up to the actual point of atomization. Oxygen pick up is also very low.

During the 2nd half year, some high speed photographs of steam atomization of tool steel were taken (not as a direct part of the current program). This study indicated that in steam atomization the basic coarse of events is formation of liquid metal "sheets" and "ligaments" under impact of the "second fluid". The falling sheets and ligaments break up under presumed surface tension forces and the smallest droplets are seen to break off the "edges" and "corners" of sheets. It would appear possible but not proven that "involution" might take place under the highly dynamic conditions of droplet formation. In such a process an exterior "surface" could be surrounded by interior liquid while surface tension forces are acting to shape the droplets. Origination of the smallest droplets at the edges of sheets also is consistent with the general picture of highest oxygen level and largest oxide inclusions in the smallest particles since liquid metal sheet "edges" would have had the greatest surface to volume ratio and consequent prior exposure to oxidation.

B. Powder Characterization

Coarse powders produced by steam, argon and nitrogen atomization were characterized by shape, size analysis, packing density and chemistry. Findings for each of the three types of alloy atomized in the program (IN-100, VM-300, and cobalt base) are summarized below. Data are related to Tables I and II covering Atomization Runs and Chemistry.

1. IN-100 (Nickel Base Alloy)

a. Morphology

Three atomizations of IN-100 were carried out, Ht. Nos. 149, 175,

and 199. In all cases the coarse powder produced was sharp and flaky with a thin adherent oxide film. Ht. No. 199, for example, (see Table I) was tapped at a very high temperature of 3140°F giving $\sim 700^\circ\text{F}$ superheat. This tap temperature, which represents a practical extreme, did not result in modification of liquid metal surface tension or oxide film formation to a sufficient degree to produce rounded particles. As in previous heats, sharp flaky powder was produced, Figure 1.

b. Chemistry

Because of the unsatisfactory particle morphology generally obtained with IN-100 coarse powder, powder chemistry was not obtained.

c. Microstructure

Structure refinement in coarse powder IN-100 has already been shown¹. Since the rate of homogenization of a cast structure is proportional to $1/l^2$ ($l = 1/2$ dendrite arm spacing or concentration "half wave length")², a major goal of the coarse powder technique in increasing the ease of homogenization of IN-100 has been achieved in spite of poor particle morphology.

2. VM-300 (Maraging Steel)

a. Morphology

A total of 25 atomizations of VM-300 were run during the first year. With the exception of large particles ~ 4 mm in Ht. No. 171 which were flake-like due to a high titanium level in the melt, all particles in each atomization were essentially rounded. Figure 2 shows the morphology of four separate size fractions of Ht. No. 218 after cleaning and hydrogen anneal. The shape of these fractions is typical of all maraging steel heats atomized to date.

b. Chemistry

In spite of nearly ideal coarse powder morphology, control of

¹ Semi-Annual Technical Report No. 1, Task I Section, Figures 2 and 3.

² P. G. Shewmon, Physical Metallurgy, Ed. by R. W. Cahn, John Wiley & Sons, N. Y. 1965, p 370-372.

powder chemistry proved to be very difficult and success has been limited to date with VM-300 maraging steel. Oxygen pick up and titanium and aluminum losses proved to be two major problems. The chemical analysis data for Ht. No. 173 (see Table II) indicate that with improved melting, tapping and tundish practice the liquid metal stream arriving at the atomization point has low oxygen and substantially correct titanium and aluminum levels. As atomized powder is oxidized¹ and analysis of cleaned powder fractions (see Table II) revealed the consistent result that oxygen pickup increases with decreasing particle size and that most titanium and aluminum has been lost in particles which are -25/+30 mesh ($\sim .6$ mm).

Atomization fluid was varied; steam Ht. Nos. 136, 145, 146, 147, 148, 150, 151, 152, 153, 166, 167, 168, 169, 170, 171 and 176; argon Ht. Nos. 137, 172, 173, 195, 196, 197, 198 and 218; and nitrogen Ht. No. 174, without substantial decrease in oxygen pickup or reactive element loss. Quenching conditions were varied including water at 6", 8" and 36" below the atomization point (Ht. Nos. 218 (6"), 195 (8") and all other heats (36") respectively except for an oil quench of liquid metal droplets, Ht. No. 197. There is some indication that high quench water level (low free fall distance from atomization point to water) decreases titanium loss and oxygen pickup particularly for large particles ~ 4 mm. Selection of a narrow size range for further processing unfortunately results in only a ~ 10 -20% yield of useful powder from the melt². Oil quenching, Ht. No. 197, did reduce oxygen pickup and titanium loss but with accompanying carbon pickup in the .1 - .3 wt % range. Since maraging steels require low carbon martensite (.03C max.) for formability and heat treating response, oil quench to prevent oxygen pickup is not feasible.

Melt additions of Ti, Al and C were made in several heats in attempts to control powder chemistry. In Ht. No. 196 where .15% C was added to the melt,

¹ Semi-Annual Technical Report No. 1, Task I Section, Figure 4.

² Semi-Annual Technical Report No. 1, Task I, Figure 13.

successively finer size fractions again showed increasing Ti and Al losses as well as increasing oxygen pickup. In the smallest fraction analyzed, -25/+30, the carbon level had been reduced to $\sim .09\%$ from $\sim .18\%$ presumably through oxidation. Ti and Al were nearly completely lost and the final $\sim .09\%$ C level was high for a "low carbon" martensite.

Titanium and/or aluminum additions were made in Ht. Nos. 167, 170, 171 and 198. The basic finding was that recovery of titanium and aluminum depended on particle size so that a given metal chemistry could be obtained only for a narrow particle size range. Table II shows analytical results for separate size fractions in various heats. Recovery of Ti and Al in the -25/+30 mesh particle range in Ht. No. 198, for example, was only $\sim 10\%$ of the concentrations in the melt before tap. Obtaining a predictable reactive element level by utilizing a large unavoidable loss to lower a high initial level, is not metallurgically practical.

Low tap temperature was tested in Ht. No. 169. With this heat, superheat at tap was only $\sim 100^{\circ}\text{F}$. This is a practical limit below which freeze up in the tundish is a recurring problem. Analysis of Ti and Al in the -14 mesh fraction powder, Table II, showed substantial losses.

In summary, control of the reactive elements Ti and Al in maraging steel VM-300 proved difficult. Under the exposure to oxidizing conditions during steam, argon or nitrogen atomization no effective mechanism was found to limit oxidation. In other types of alloy this might be accomplished by high carbon level, high chromium, or in nickel base alloys, high aluminum levels. These alternatives were not feasible in the present case because of the careful composition balance required in maraging steels.

c. Microstructure

The unetched and etched structures of four separate mesh fractions (-4/+5, 4.3 mm; -8/+10, 2.0 mm; -16/+18, 1.0 mm; and -25/+30, 0.6 mm) of Ht. No. 218 are shown in Figures 3, 4, 5 and 6. Powder fractions

of this heat had, except for Ht. No. 197, oil quench, substantially the lowest oxygen levels obtained for VM-300. Oxide inclusions persisted nevertheless, with generally the largest inclusions occurring in the smallest particles similarly to Ht. No. 172.¹ Secondary dendrite arm spacings are also noted in the captions for each fraction. These values are comparable to those determined previously for maraging steel.²

3. Cobalt Base Superalloy

a. Morphology

Two heats of a cobalt base alloy with nominal composition 20% Cr, .25% C, 10% Ni, 7.5% Mo, 5% Hf and bal. Co were steam atomized. The first Ht. No. 185 was steam atomized without any melt additions (see Table I). Resulting powder was "sharp" and "flaky", Figure 7, left, with great similarity to IN-100 powder (see Figure 1). The reactive metal hafnium is considered to strongly influence thin oxide skin formation leading to the non-rounded morphology. The second Ht. No. 217 was made with additions to the melt of 0.83% Si and 0.04% B. These elements were added on the basis of previous experience with cobalt base alloys as well as the fact that oxides of boron and silicon are "glass formers" and frequently decrease the melting point of higher melting oxides. Figure 7, right, (powder in cleaned condition) shows the distinct improvement in particle morphology for the cobalt hafnium alloy when steam atomized after these additions. Table I shows that tap temperature for Ht. No. 217 was higher (3100°F) than for Ht. No. 185 (2850°F). This difference is not considered the cause of increased

¹Semi-Annual Technical Report No. 1, Task I, Figures 5 - 8.

²Ibid, Task II, Figure 4.

particle roundness, since with IN-100 with no melt additions and the presence of substantial titanium and aluminium, very high tap temperature did not eliminate flake-like coarse powder.

b. Chemistry

In the case of Ht. No. 217, cleaned powder was forwarded to MIT, Task III, for chemical analysis.

c. Microstructure

Figure 8 shows the fine carbide dispersion generated in Ht. Nos. 185 and 217. In spite of differing particle morphology, dendritic structure is substantially identical for both heats and of the same order of magnitude as that of IN-100¹ and VM-300, Figures 3 to 6.

C. Cleaning

Coarse powder produced by steam, argon or nitrogen atomization which is, in turn, water quenched generally has an oxide coat regardless of the alloy system. The cleaning method previously described² has been found useful for iron, nickel and cobalt base alloys. Where clean coarse powder has been required for consolidation, this method was applied and "recycle" performed up to five times. In the case of iron base alloys, which tarnish on drying from a water rinse, a final hydrogen reduction step, again as described, has been used.

D. Powder Consolidation

1. Objectives

The advantages of chemical homogeneity and structure refinement attained by rapid quenching of liquid metals can only be realized if the metal powder can

¹ Semi-Annual Technical Report No. 1, Task I, Figure 2.

² Semi-Annual Technical Report No. 1, Task I, Pg. 6.

be "put together again" by appropriate process "consolidation" steps.

Therefore, in the present program two objectives were established:

1. production of material for test in Tasks III and IV, and 2. understanding of the fundamental steps in consolidation.

For consolidation hot isostatic pressing, extrusion, and hot isostatic pressing followed by extrusion were used in the present program. In the cases of IN-100 and VM-300 where the coarse powder process was not successful in producing "state of the art" powders, the consolidation processing was carried out with fine powders produced by current commercial processes.

2. Hot Isostatic Pressing Runs

A summary of all hot isostatic pressing runs carried out in the present program for production of material for Tasks III and IV or for study of consolidation is given in Table III. For HIP processing powders were sealed in mild steel cans which had been degreased and hydrogen or vacuum annealed, cans were heated in the range 600-800°F, vacuum evacuated and sealed by welding. Selection of an appropriate hot isostatic pressing cycle for a given alloy depends on some or all of the following factors:

1. Minimum temperature, pressure and time for interparticle bonding.
2. Temperature at which unacceptable structure coarsening occurs.
3. Temperature at which incipient melting occurs.
4. Time and temperature for homogenization of dendritic cast structure of powder.
5. Nature and extent of further hot or cold processing after hot isostatic pressing.
6. Nature of phase transformations available for structure refinement; in the case of steels this would be "normalization".

7. Application of alloy for low, intermediate or high temperatures, fatigue requirements, fracture toughness, etc.
8. Nature and concentration of surface and internal contaminants in powder.

Experience may show additional factors which must be considered.

The "as pressed" microstructures of each of the three types of alloy processed are discussed below. In some cases heat treatment response of the "as pressed" structure was also studied and where this amplifies the understanding of the HIP process, results are included.

a. IN-100

Figures 9, 10, and 11 show the first hot isostatically pressed structures of IN-100 investigated in this program. Successively higher process temperatures of 2100, 2200, and 2320°F have resulted in gradual elimination of the "cast" powder structure, grain growth particularly at 2320°F, and coarsening of the interparticle boundary structure. With coarser powder, Figure 12, and lower HIP temperature of 2000°F, the "cast" grain size of powder is revealed within larger particles. Grain boundaries appear to be pinned by carbides (upper left, Figure 12). Complete solutioning and homogenization of the pressed structure of Figure 12 is not achieved after 4 hours @ 2100°F, Figure 13. Cast dendritic structure persists and the particle boundary structure coarsens. Solutioning at 2200°F, Figure 14, eliminates dendritic structure and further coarsens interparticle boundary structure. Segments of this structure appear to be carbides. Grain growth has been inhibited at particle boundaries. The same -20/+40 mesh Homogeneous Metals powder HIP processed at 2300°F, Figure 15, shows complete elimination of dendrite structure, grain growth and well defined interparticle films. Additional solutioning of this structure, Figure 16, causes little change but clearly shows the limiting effect of what are apparently carbides on grain growth, particularly at particle boundaries. One extrusion billet 3 1/4" x 14" of Homogeneous Metals IN-100 powder was processed at 2300°F, No. 10. The processing temperature was selected on the basis of expected homogenization as

shown by previous data. In this case, however, pressure was only 15,000 psi as opposed to 25,000 psi for No. 4 and 5, Table III. The unetched structure showed some porosity, Figure 17. Solution heat treatment at 2300°F and 1 atmosphere pressure (normal furnace operation), of the 2300°F, 15,000 psi compact generated numerous voids at particle boundaries, Figure 18. This data clearly showed for the first time a significant effect of HIP process pressure on interparticle bonding since higher pressure bonding (25,000 psi) of the same type of powder showed no void generation on heat treatment. Cause of this behavior is suspected (but not yet proven) to originate in residual gas content of the compact or the powder due to the hydrogen gas used in the atomization process.¹ In brief summary, HIP processing of IN-100 powders has indicated that besides oxygen content, which has been established as a "fundamental" measure of purity, both carbon and "other" gas levels warrant future detailed investigation.

b. VM-300

Figures 19 and 20 (No. 6 and 7, Table III) show structures of the first hot isostatic pressings made of coarse powder VM-300. The 2300°F pressing, Figure 19, shows no traces of particle boundaries and a high degree of homogeneity, but a few oxide inclusions which have persisted in VM-300 coarse powder. The 2000°F pressing, Figure 20, shows traces of interparticle boundaries. In maraging steel, coarse prior austenite grain size may decrease fracture toughness but if the HIP compact were to be further worked, it would appear that 2300°F would be a preferred pressing temperature. Fine powder VM-300 made by the Homogeneous Metals "vacuum" process was hot isostatically pressed at 2300°F (No. 11, Table III) for an extrusion billet. This structure, Figure 21, shows no evidence of banding² but a coarse martensite indicating large prior austenite grain size. A fourth HIP compact for extrusion (No. 13, Table III) was made by VM-300 using Nuclear Metals rotating electrode process powder. Figure 22 shows the structure which

¹Semi-Annual Technical Report No. 1, Task I, Introduction.

²Semi-Annual Technical Report No. 1, Task III, Figures 1 & 2.

has no detectable particle boundaries, excellent homogeneity and again a coarse martensite structure reflecting probable large prior austenite grain size due to the 2200°F pressing temperature. The martensite structure of steam atomized coarse powder pressed at 2300°F (Figure 19) is finer than that of the two commercial powders, Figures 21 and 22. This may be due to grain boundary pinning by inclusions. For competitive powder processes structure coarsening in HIP processing might be used as a "purity" indicator.

c. Cobalt Alloys

Figures 23 and 24 show the first HIP compact of steam atomized Mar M 509 (No. 8, Table III). Prior particle boundaries are identifiable as carbide free curved bands. This effect may originate in decarburization during atomization in an oxidizing atmosphere. Compositions of the cobalt base alloys are given in Table V. In the case of Mar M 509 "+" (No. 9, Table III) prior particle boundaries are outlined in some areas by both oxide inclusions and voids, Figure 25. This finding indicates that a powder must be cleaned more stringently and that a temperature $> 2175^{\circ}\text{F}$ should be used in HIP processing. Incipient melting for Mar M 509 occurs at $\sim 2350^{\circ}\text{F}$ which establishes an upper limit for HIP processing unless liquation is purposely desired. Mar M 509 was pressed at 2300°F in billet form (No. 12, Table III) for extrusion. Figure 26 shows the as pressed microstructure. Prior particle boundaries are less evident in this structure than in Figure 23. A cobalt-hafnium coarse powder was HIP processed for an extrusion billet (No. 14, Table III). In this case a poor structure with voids resulted, Figure 27. Process temperature was 2100°F. Higher temperature, perhaps $\sim 2300^{\circ}\text{F}$, clearly is required. A final billet of Mar M 509 "+" was processed (No. 15, Table III). Structure is shown in Figure 28. Voids at (see Figure 28) the particle boundaries indicate that the process temperature of 2100°F was too low. The total experience with cobalt base alloys to date indicates that HIP process temperature should be $\sim 2300^{\circ}\text{F}$ for 15,000 psi minimum pressure and 1 hr. minimum dwell time.

In the cobalt alloys the preference of carbides for intragranular sites apparently has prevented continuous carbide film formation at particle boundaries during hot isostatic pressing, see Figure 24, for example. This behavior is in direct contrast to that of what are assumed to be carbides in the IN-100 HIP compacts Figures 11, 13, 14, 15 and 16 where interparticle films are prevalent. In cast or wrought nickel base alloys, carbide films are undesirable and may lead to loss of ductility and decreased rupture life.¹ Powder compacts of cobalt base alloys may ultimately prove to have advantages in certain applications because of this freedom from interparticle carbide film formation.

4. Extrusion Runs

A summary of all extrusion runs is given in Table IV. In the case of direct extrusion of powder, canning was done in evacuated and sealed mild steel tubing. For HIP billets, the solid billet was in some cases provided with a mild steel tubular sleeve to bring the billet diameter to the working range of the extrusion press liner. Structures of the extrusions are discussed below.

a. IN-100

One HIP compact (No. 10, Table III) was extruded. Porosity which was apparent in the HIP compact (Figure 17) persisted through extrusion, Figure 29. Porosity is again primarily at particle boundaries. With this particular powder (Homogeneous Metals - 20 mesh) full density by HIP processing clearly appears desirable before extrusion.

b. VM-300

Steam atomized and cleaned coarse powder was direct extruded early in the program, No. 3, Table IV. Structure is shown in Figure 30. Reduction was 10.5 x in extrusion and proved insufficient to eliminate all porosity (upper right, Figure 30). The first HIP compact of VM-300 extruded was No. 5, Table IV. Compared to the HIP structure, Figure 21, the extruded structure shows substantial grain refinement. As in the HIP structure, banding has been eliminated, and no clear evidence of particle boundaries is present.

¹R. F. Decker, Strengthening Mechanisms in Nickel Base Superalloys. Market Development Dept., International Nickel Company, 1969, pg. 15-19.

This material unfortunately proved to be contaminated with a second alloy powder. Direct powder extrusion, No. 6, Table IV, of the same Homogeneous Metals -20 mesh, VM-300 powder as above shows, beside the unfortunate contamination, some evidence of prior particle boundaries, Figure 32. These boundaries are indicated as faint lines of co-linear grain boundaries and may be seen more easily by viewing micro at a low angle along the extrusion direction. Extrusion of a HIP compact of Nuclear Metals Powder, No 10, Table IV and a billet of the same powder uncompacted, No. 11, Table IV, shows improved elimination of particle boundaries in the HIP compact after extrusion, Figure 33 vs Figure 34. The particle boundary structure may prove to have significant effects on fracture toughness and transverse properties of high strength alloys such as VM-300.

c. Cobalt Alloys

Three cobalt alloys were extruded, each after HIP compaction. Mar M 509, No. 9, Table IV, Figure 35 showed break-up of the coarse powder dendrite structure, shown in Figure 26 after hot isostatic pressing. The extruded structure appeared void free. At 500X, Figure 36, the extruded structure is totally different than that of conventional cast Mar M 509.¹ Chinese script and lamellar eutectic carbides have been replaced completely by spheroidal carbides. The extruded structure is surprisingly analogous to those of carbide dispersion strengthened cobalt base tool alloys produced by atomization and studied by Reen.² The second HIP compact extruded was coarse powder cobalt-hafnium alloy, No. 12, Table IV. In this case porosity was known to exist in the HIP compact but it was assumed extrusion would eliminate it. Figure 37 shows

¹ A.M. Beltran, C. T. Sims, and N. T. Wagenheim, The High Temperature Properties of Mar-MAlloy 509. *Journal of Metals*, September 1969, pg. 39-47.

² Reen, O. W., Development of Dispersion-Hardened Cobalt-Base Cutting Tool Alloys from Atomized Powders, *Modern Developments in Powder Metallurgy*, Vol. 2, Ed. H. H. Hausner, Plenum Press, N. Y. 1966, pg. 182-201.

a large void in the extruded bar. This finding suggests preference for full densification by HIP processing of coarse powder before extrusion, since extrusion does not necessarily close all voids. A HIP billet of Mar M 509 "+" (see Table V for composition) was extruded, No. 13, Table IV. The extruded structure, Figure 38, shows oxide stringers and in some cases associated voids. These appear as black stringers and indicate requirement for greater cleaning of powder .

III. CONCLUSIONS

Significant findings from the program for production of solid bars from rapidly quenched liquid metals include the following:

1. Steam atomization at its present stage of development can be used successfully for cobalt base alloys.
2. The effects of impurities on the bonding of metal powder particles in hot isostatic pressing and extrusion are generally harmful with mechanisms depending on the alloy system. Aside from oxygen, hydrogen, carbon, and probably nitrogen may have detectable effects at powder particle boundaries.
3. Extrusion does not necessarily close all voids in a powder or HIP billet. This finding suggests that the best process route for solid material production requires full densification by hot isostatic pressing before extrusion.

Atomization Runs

Heat No.	Alloy	Weight/lbs.	Atomization, Steam, Argon, Nitrogen	Nozzles, Pressures		Tundish	Tap Temperature	Objective	Result	Median Particle Size, Microns. Standard Deviation σ = 84%Point/50%Point
				Top Pressure	Side Pressure					
136	VM-300	13.4	S	60 mmg 8 psig	2.5 x 100 mmf 10 psig	10 mm	3200	Preliminary test of VM-300 atomization	Coarse rounded powder. Oxidized.	1650; σ = 2.18
137	VM-300	13.0	Ar	-----	Unijet "U" 50 psig	10 mm	3150	Preliminary test of VM-300 atomization.	Coarse rounded powder. Oxidized.	2330; σ = 1.48
145	VM-300	17.2	S	60 mmg 9 psig	2.5 x 100 mmf 12 psig	10 mm	3040	Test reduced tap temp.	Coarse rounded powder. Tundish freeze up.	1700; σ = 1.94
146	VM-300	16.2	S	60 mmg 9 psig	2.5 x 100mmf 12 psig	11.9 mm	3035	Test increased tundish nozzle to reduce freeze up.	Coarse rounded powder. Freeze up of last ~ 3 lbs. in tundish.	2000; σ = 1.85
147	VM-300	34.0	S	60 mmg 9 psig	2.5 x 100 mmf 12 psig	11.9 mm	3090	Produce material for cleaning and extrusion.	Coarse rounded powder. Oxidized.	2050; σ = 1.90
148	VM-300	34.2	S	60 mmg 9 psig	2.5 x 100 mmf 12 psig	11.9 mm	3080	Produce material for cleaning and extrusion.	Coarse rounded powder. Oxidized.	2250; σ = 1.91
149	IN-100	22.1	S	60 mmg 9 psig	2.5 x 100 mmf 12 psig	11.9 mm	3070	Preliminary test of IN-100 atomization.	Sharp flaky powder Thin adherent oxide.	Not Determined
150	VM-300	33.9	S	60 mmg 9 psig	2.5 x 100 mmf 12 psig	11.9 mm	3060	Produce material for hot isostatic pressing and extrusion.	Coarse rounded powder. Oxidized.	2000; σ = 1.95
151	VM-300	33.8	S	60 mmg 9 psig	2.5 x 100 mmf 12 psig	11.9 mm	3095	Produce material for hot isostatic pressing and extrusion.	Coarse rounded powder. Oxidized.	151, 152, 153 combined heats: 2350; σ 1.92

Heat No.	Alloy	Weight/lbs.	Atomization S, A, N ₂	Nozzles, Pressures		Tundish Nozzle	Top Temperature	Objective	Result	Median Particle Size, Microns. Standard Deviation σ = 84%Point/50%Point
				Top Pressure	Side Pressure					
152	VM-300	33.8	S	60 mmg 9 psig	2.5 x 100 mmf 12 psig	11.9 mm	3110	Produce material for hot isostatic pressing and extrusion.	Coarse rounded powder. Oxidized.	151, 152, 153 combined heats: 2350; σ = 1.92
153	VM-300	33.9	S	60 mmg 9 psig	2.5 x 100 mmf 12 psig	11.9 mm	3085	Produce material for hot isostatic pressing and extrusion.	Coarse rounded powder. Oxidized.	
166	VM-300	17.0	S	60 mmg 9 psig	2.5 x 100 mmf 12 psig	12.7 mm	2870	Test effect of lower tap temperature on losses of Ti and Al.	Coarse rounded powder. Black oxide coat.	Not determined
167	VM-300+ 0.25%Al, 0.30%Ti	17.0	S	60 mmg 9 psig	2.5 x 100 mmf 12 psig	12.7 mm	2900	Test recovery of late melt additions of Ti and Al.	Coarse rounded powder. Black oxide coat. See Table II.	Not determined
168	VM-300	17.2	S	60 mmg 9 psig	2.5 x 100 mmf 12 psig	12.7 mm	2910	Test tap temp. of 2750°F.	Temperature overshot. Tapped @ 2910. Coarse rounded powder.	2000; σ = 1.90
169	VM-300	16.9	S	60 mmg 9 psig	2.5 x 100 mmf 12 psig	12.7 mm	2760	Test effect of lower tap temp. on losses of Ti and Al.	Rounded powder. Black oxide coat. See Table II.	1700; σ = 1.58
170	VM-300* 0.06%Al, 0.74% Ti	17.0	S	60 mmg 9 psig	2.5 x 100 mmf 12 psig	12.7 mm	2775	Test recovery of Ti and Al additions with low tap temp.	Coarse rounded powder. Large particles elongated. See Table II.	2150; σ = 2.21
171	VM-300+ 0.09%Al 1.10%Ti,	17.0	S	60 mmg 9 psig	2.5 x 100 mmf 12 psig	12.7 mm	2765	Test recovery of Ti and Al additions with low tap temp.	Small fractions rounded. Larger particles flake like. See Table II.	2800; σ = 2.50

172	VM-300	25.2	Ar	----	Unijet "U" 60 psig	10 mm	2845	Test improved tundish practice and Argon atomization on oxygen pickup. Ti, Al recovery.	Coarse rounded powder. Black oxide coat. See Table II.	3100; σ = 2.06
173	VM-300	25.2	Ar	----	Unijet "U" 70 psig	10 mm	2830	Reduce size range. Test oxygen pickup and Ti, Al recovery. Sample liquid metal stream out of tundish.	Coarse rounded powder. Black oxide coat. See Table II.	2350; σ = 1.70
174	VM-300	25.5	N ₂	----	Unijet "U" 70 psig	10 mm	2815	Test N ₂ atomization on oxygen pickup and Ti, Al recovery.	Coarse rounded powder. Black oxide coat. See Table II.	1750; σ =2.17
175	IN-100	22.8	Ar	----	Unijet "U" 60 psig	10 mm	2650	Test Argon atomization of IN-100 with improved tundish practice.	Sharp pointed, twisted flakes.	Not determined
176	VM-300	26.6	S	60 mmg 9 psig	2.5 x 100 mmf 12 psig	10 mm	2790	Test steam atomization on oxygen pickup and Ti, Al recovery with improved tundish practice.	Medium rounded powder. Black oxide coat. See Table II.	1200; σ = 2.0
185	Cobalt-Hf	22.95	S	60 mmg 9 psig	2.5 x 100 mmf 12 psig	10 mm	2850	Produce coarse powder for cleaning and compaction.	Sharp flaky powder.	Not determined
95	VM-300	17.4	A	----	Unijet "U" 52 psig	13/32 [#]	2900	Determine effect of very high water level in quench tank on <u>O</u> , Ti, & Al levels in powder.	Coarse rounded powder. Black oxide coat.	Not determined

Heat No.	Alloy	Weight/lbs.	Atomization S, A, N ₂	Nozzles, Pressures		Tundish Nozzle	Tap Temperature	Objective	Result	Median Particle Size, Microns. Standard Deviation $\sigma = 84\%$ Point/50% Point
				Top Pressure	Side Pressure					
196	VM-300 +.15% C	16.9	A	----	Unijet "U" 55 psig	13/32" ϕ	2840	Determine effect of .15% carbon addition to melt on \bar{Q} pickup and Ti & Al losses.	Coarse rounded powder. Black oxide coat. See Table II.	Not determined
197	VM-300	16.8	A	----	Unijet "U" 52 psig	13/32" ϕ	2880	Determine effect of oil quench of liquid metal droplets on \bar{Q} pickup and Ti & Al losses.	Coarse rounded powder. Black oxide coat. See Table II.	Not determined
198	VM-300	17.0	A	----	Unijet "U" 54 psig	13/32" ϕ	2900	Determine effect of 0.6% excess Al on \bar{Q} pickup and Ti & Al losses.	Coarse rounded powder. Black oxide coat. See Table II.	Not determined
199	IN-100	22.9	S	60 mmHg 8 psig	2 1/2 x 100 mm 12 psig	13/32" ϕ	3140	Determine effect of very high tap temperature on particle geometry.	Sharp flaky powder. Substantially the same morphology as for previous IN-100 atomizations. Fig. I	Not determined
217	Cobalt-Hf +.83% Si, 0.04% B	22.5	S	60 mmHg 5 psig	2 1/2 x 100 mm 8 psig	13/32" ϕ	3100	Produce coarse rounded powder suitable for cleaning. Modify surface chemistry with B & Si additions.	Coarse rounded powder. Some shells. See Figure 7.	Not determined
218	VM-300	27.9	A	----	Unijet "U" 56 psig	13/32" ϕ	2910	Modify conditions of 30-195 to give minimum (6") free fall of metal droplets before water quench.	Coarse rounded powder. Some oxide coat but otherwise "bright". See Table II.	Not determined

Table II
Chemistry

Heat No.	Alloy	Sample Description	Q ppm	Ti Wt. %	Al Wt. %	C Wt. %
147	VM-300	1. Melt dip sample (all melt dip samples taken just before tap)	37	.52	.03	.014
		2. Coarse powder, 1 chem. cleaning cycle. "Large" particles	1500	N.D.*	N.D.	N.D.
		3. Coarse powder, 2 chem. cleaning cycles. "Small" particles	1500	N.D.	N.D.	N.D.
		4. Coarse powder, 3 chem. cleaning cycles. "Large" particles	990	N.D.	N.D.	N.D.
		5. Coarse powder, 3 chem. cleaning cycles. "Small" particles	1500	N.D.	N.D.	N.D.
		6. Duplicate analysis of (5)	1200	N.D.	N.D.	N.D.
		7. Extruded bar; center of extrusion length	1500	N.D.	N.D.	N.D.
148	VM-300	1. Melt dip sample	1100	.04	.01	.0086
		2. Coarse powder, 3 chem. cleaning cycles + 1600°F H ₂ reduction	1600	N.D.	N.D.	N.D.
		3. Duplicate analysis of (2)	1600	N.D.	N.D.	.0087
		4. Extruded bar; center of extrusion length	2000	N.D.	N.D.	N.D.
		5. Melt dip sample	1500	N.D.	N.D.	N.D.
		6. Coarse powder, 3 chem. cleaning cycles + 1600°F H ₂ reduction	20	.58	.04	.014
		7. Duplicate analysis of (6)	900	.06	.02	.012
150	VM-300	1. Melt dip sample	1400	N.D.	N.D.	.011
		2. Coarse powder, 3 chem. cleaning cycles + 1600°F H ₂ reduction	710	N.D.	N.D.	N.D.
		3. Duplicate analysis of (2)	1100	N.D.	N.D.	N.D.
		4. Extruded bar; center of extrusion length	1400	N.D.	N.D.	N.D.
151	VM-300	1. Melt dip sample	19	.40	.03	.021
		2. Coarse powder, 3 chem. cleaning cycles + 1600°F H ₂ reduction	28	.46	.03	.018
152	VM-300	1. Melt dip sample	50	.46	.03	.026

*N.D. = Not Determined

Table II

Chemistry

Heat No.	Alloy	Sample Description	\bar{Q} ppm	Ti Wt. %	Al Wt. %	C Wt. %
153	VM-300	1. Melt dip sample	26	.48	.03	.026
166	VM-300	1. Melt dip sample 2. Coarse powder, -4/+14 mesh, 1 chem. cleaning cycle "Large" particles "Small" particles 3. Coarse powder, -14 mesh, 1 chem. cleaning cycle	14 1800 1600 2400	.56 N.D. N.D. .11	.14 N.D. N.D. .04	N.D. N.D. N.D. N.D.
167 Ti, Al Additions	VM-300	1. Melt dip sample 2. Coarse powder, -4/+14 mesh, 1 chem. cleaning cycle 3. Coarse powder, -14 mesh, 1 chem. cleaning cycle "Large" particles "Small" particles	36 1100 950 2200	.91 N.D. .30 N.D.	.95 N.D. .30 N.D.	N.D. N.D. N.D. N.D.
168 High tap Temperature	VM-300	1. Melt dip sample 2. Coarse powder, -14 mesh, 1 chem. cleaning cycle	37 1800	.63 .11	.21 .01	N.D. N.D.
169 Low tap Temperature	VM-300	1. Melt dip sample 2. Coarse powder, -14 mesh, 1 chem. cleaning cycle	13 2400	.53 .11	.03 .01	N.D. N.D.
170 Ti, Al Additions	VM-300	1. Melt dip sample 2. Coarse powder, -14 mesh, 1 chem. cleaning cycle	24 2500	1.14 .27	.06 .01	N.D. N.D.
171 Ti, Al Additions	VM-300	1. Melt dip sample 2. Coarse powder, -14 mesh, 1 chem. cleaning cycle	28 2400	1.46 .48	.13 .03	N.D. N.D.

Table II

Chemistry

Heat No.	Alloy	Sample Description	O ppm	Ti Wt. %	Al Wt. %	C Wt. %
I72 Improved Tundish Practice	VM-300	1. Melt dip sample	21	.43	.056	N.D.
		2. Coarse powder, -4/+5 mesh, 2 chem. cleaning cycles + HCl etch	630	.13	.022	N.D.
		3. Coarse powder, -16/+18 mesh, 2 chem. cleaning cycles + HCl etch	2800	.10	.011	N.D.
I73 Argon Atomization	VM-300	1. Melt dip sample	10	.50	.11	N.D.
		2. Tundish stream sample	45	.52	.08	N.D.
		3. Coarse powder, -4/+5 mesh, 2 chem. cleaning cycles + HCl etch	800	.23	.04	N.D.
		4. Coarse powder, -8/+10 mesh, 2 chem. cleaning cycles + HCl etch	2000	N.D	N.D	N.D.
		5. Coarse powder, -16/+18 mesh, 2 chem. cleaning cycles + HCl etch	2600	.34	.01	N.D.
		6. Coarse powder, -25/+30 mesh, 2 chem. cleaning cycles + HCl etch	3600	N.D	N.D	N.D.
I74 N2 Atomization	VM-300	1. Melt dip sample	18	.48	.09	N.D.
		2. Coarse powder, -4/+5 mesh, 2 chem. cleaning cycles + HCl etch	980	.36	.04	N.D.
		3. Coarse powder, -8/+10 mesh, 2 chem. cleaning cycles + HCl etch	2400	N.D	N.D	N.D.
		4. Coarse powder, -16/+18 mesh, 2 chem. cleaning cycles + HCl etch	4700	.20	.03	N.D.
		5. Coarse powder, -25/+30 mesh, 2 chem. cleaning cycles + HCl etch	4200	N.D	N.D	N.D.
I76 Steam Atomization	VM-300	1. Melt dip sample	240	.68	.23	N.D.
		2. Coarse powder, -4/+5 mesh, 2 chem. cleaning cycles + HCl etch	2100	.59	.18	N.D.
		3. Coarse powder, -8/+10 mesh, 2 chem. cleaning cycles + HCl etch	2000	N.D	N.D	N.D.
		4. Coarse powder, -16/+18 mesh, 2 chem. cleaning cycles + HCl etch	2600	.48	.17	N.D.
		5. Coarse powder, -25/+30 mesh, 2 chem. cleaning cycles + HCl etch	2800	N.D	N.D	N.D.
Note: Results questionable due to possible crucible contamination from previous Heat No. I75, IN-100 Alloy, high Ti, high Al.						
I95 High water	VM-300	1. Melt dip sample	20	.47	.078	N.D.
		2. Coarse powder, -4/+5 mesh, 3 chem. cleaning cycles + HCl etch	490	.334	.036	N.D.
		3. Coarse powder, -8/+10 mesh, 3 chem. cleaning cycles + HCl etch	1220	.186	.03	N.D.
		4. Coarse powder, -25/+30 mesh, 3 chem. cleaning cycles + HCl etch	1470	.17	.03	N.D.
		5. Coarse powder, -25/+30 mesh, 3 chem. cleaning cycles + HCl etch	1570	.12	.02	N.D.

Table II

Chemistry

Heat No.	Alloy	Sample Description	O ppm	Ti Wt. %	Al Wt. %	C Wt. %
196 Carbon Addition	VM-300	1. Melt dip sample	19	.50	.067	.178
		2. Coarse powder, -4/+5 mesh, 3 chem. cleaning cycles + HCl etch	910	.14	.032	.115
		3. Coarse powder, -8/+10 mesh, 3 chem. cleaning cycles + HCl etch	1010	.06	.020	.103
		4. Coarse powder, -16/+18 mesh, 3 chem. cleaning cycles + HCl etch	1530	.05	.010	.090
		5. Coarse powder, -25/+30 mesh, 3 chem. cleaning cycles + HCl etch	2920	.05	Tr.	.086
197 Oil quench	VM-300	1. Melt dip sample	19	.56	.15	.0119
		2. Coarse powder, -4/+5 mesh, 3 chem. cleaning cycles + HCl etch	560	.40	.06	.281
		3. Coarse powder, -8/+10 mesh, 3 chem. cleaning cycles + HCl etch	537	.34	.07	.327
		4. Coarse powder, -16/+18 mesh, 3 chem. cleaning cycles + HCl etch	990	.22	.06	.220
		5. Coarse powder, -25/+30 mesh, 3 chem. cleaning cycles + HCl etch	1280	.07	Tr.	.103
198 Al Addition	VM-300	1. Melt dip sample	10	.68	.97	N.D.
		2. Coarse powder, -4/+5 mesh, 3 chem. cleaning cycles + HCl etch	1220	.40	.64	N.D.
		3. Coarse powder, -8/+10 mesh, 3 chem. cleaning cycles + HCl etch	1330	.28	.43	N.D.
		4. Coarse powder, -16/+18 mesh, 3 chem. cleaning cycles + HCl etch	2480	.07	.11	N.D.
		5. Coarse powder, -25/+30 mesh, 3 chem. cleaning cycles + HCl etch	2750	.139	.098	N.D.
218 High water	VM-300	1. Melt dip sample	37	.54	.085	N.D.
		2. Coarse powder, -4/+5 mesh, 5 chem. cleaning cycles + 1600°F H ₂ anneal	510	.41	.04	N.D.
		3. Coarse powder, -8/+10 mesh, 5 chem. cleaning cycles + 1600°F H ₂ anneal	690	.15	Tr.	N.D.
		4. Coarse powder, -16/+18 mesh, 5 chem. cleaning cycles + 1600°F H ₂ anneal	1300	.14	Tr.	N.D.
		5. Coarse powder, -25/+30 mesh, 5 chem. cleaning cycles + 1600°F H ₂ anneal	1500	.092	Tr.	N.D.

Table III
Hot Isostatic Pressing Runs (Chronological)

No.	Powder	Billet Size at Start	Pressing Conditions	Microstructure
1.	IN-100 Federal-Mogal -50 mesh	~1" ϕ x 3"	2100°F, 15,000 psi 2 hrs.	As pressed. Figure 9 500x
2.	IN-100 Federal-Mogal -60 mesh	~1" ϕ x 3"	2200°F, 15,000 psi 2 hrs.	As pressed. Figure 10 500x
3.	IN-100 Federal-Mogal -60 mesh	3/4" ϕ x 9"	2320°F, 29,500 psi 2 hrs.	As pressed. Figure 11 500x
4.	IN-100 Homogeneous Metals -20/+40 mesh	3/4" ϕ x 9"	2000°F, 25,000 psi 2 hrs.	1. As pressed. Figure 12 500x 2. HIP + 2100°F 4 hrs. AC Figure 13 500x 3. HIP + 2200°F 4 hrs. AC Figure 14 500x
5.	IN-100 Homogeneous Metals -20/+40 mesh	1" ϕ x 9"	2300°F, 25,000 psi 2 hrs.	1. As pressed. Figure 15 500x 2. HIP + 2200°F 4 hrs. AC Figure 16 500x
6.	VM-300 IMT 136 Cleaned -4/+14 mesh	1 1/2" ϕ x 9"	2300°F, 25,000 psi 2 hrs.	As pressed. Figure 19 100x
7.	VM-300 IMT 137 Cleaned -4/+14 mesh	1" ϕ x 11"	2000°F, 25,000 psi 2 hrs.	As pressed. Figure 20 100x
8.	Mar M 509 IMT III Cleaned -8/+14 mesh	1" ϕ x 6"	2175°F, 15,000 psi 1 hr.	As pressed. Figure 23 100x Figure 24 500x
9.	Mar M 509 "4" IMT II2 Cleaned, -8/+14 mesh	1" ϕ x 6"	2175°F, 15,000 psi 1 hr.	As pressed. Figure 25 100x

Table III (cont)

No.	Powder	Billet Size at Start	Pressing Conditions	Microstructure
10.	IN-100 Homogeneous Metals -20 mesh	3 1/4" ϕ x 14"	2300°F, 15,000 psi 1 1/4 hrs.	1. As pressed. Figure 17 Unetched 100x 2. HIP + 2300°F 4 hrs. Fig. 18 Unetched 100x
11.	VM-300 Homogeneous Metals -20 mesh	3 1/4" ϕ x 14"	2300°F, 14,500 psi 1 hr.	As pressed. Figure 21 100x
12.	Mar M 509 IMT III Cleaned, -4/+8 mesh	3 1/4" ϕ x 14"	2300°F, 15,000 psi 1 hr.	As pressed. Figure 26 100x
13.	VM-300 Nuclear Metals -35 mesh	3 1/4" ϕ x 14"	2200°F, 14,500 psi 1 hr.	As pressed. Figure 22 100x
14.	Cobalt-Hafnium Alloy IMT 217 Cleaned -4/+14 mesh	3 1/4" ϕ x 12"	2100°F, 14,500 psi 1 hr.	As pressed. Figure 27 100x
15.	Mar M 509 "A" IMT II2 Cleaned -4/+8 mesh	3 1/4" ϕ x 12"	2100°F, 14,500 psi 1/2 hr.	As pressed. Figure 28 100x
16.	IN-100 VM-300 Stacked 1/4" bars, Task II	2" ϕ x 12"	2050°F 1/4 hr., +2150°F 1 hr. 14,500 psi	All material forwarded to Task II.

Table IV

-26-

Extrusion Runs (Chronological)

Ext. No.	Powder and/or Billet Description	Billet Size	Ext. Temp.	Ext. Ratio	Microstructure	Remarks
1.	IMT Ht. No. 147 and 148 blend Cleaned, H ₂ annealed, -4/+35	3 1/2" ϕ x 10"	2050°F	10.5x		
2.	IMT Ht. No. 147 Cleaned, H ₂ annealed, -4/+35	3 1/2" ϕ x 10"	2050°F	10.5x		
3.	IMT Ht. No. 148 Cleaned, H ₂ annealed, -4/+35	3 1/2" ϕ x 10"	2050°F	10.5x	As extruded Figure 30 Long. 100x	Forwarded to Task III for test.
4.	IN-100 HIP Compact Item 10, Table III	3.18" ϕ x 10"	2000°F	14.3x	As extruded Figure 29 Long. 100x	Forwarded to Task III.
5.	VM-300 HIP Compact Item 11, Table III	3.18" ϕ x 10"	2000°F	14.3x	As extruded Figure 31 Long. 100x	Contained 2nd alloy powder contamination. Forwarded to Task IV for test.
6.	VM-300 Homogeneous Metals Pwd. -20 mesh.	3.18" ϕ x 10"	2000°F	14.3x	As extruded Figure 32 Long. 100x	Contained 2nd alloy powder contamination. Forwarded to Task III for test.
7.	VM-300 Homogeneous Metals Pwd.	3.18" ϕ x 10"	2000°F	14.3x	Duplicate of No. 6	Contained 2nd alloy powder contamination. Forwarded to Task III for test.
8.	IN-100 Homogeneous Metals Pwd.	3.18" ϕ x 10"	2000°F	14.3x	Not determined.	Stalled in extrusion on three successive attempts. Ram compacted billet forwarded to Task III.

Table IV (cont)

Ext. No.	Powder and/or Billet Description	Billet Size	Ext. Temp.	Ext. Ratio	Microstructure	Remarks
9.	IMT Ht. No. III Mar M 509 Item 12, Table III	2.6" ϕ x 10"	2000°F	15.2x	As extruded Figure 35 Long. 100x Long 500x	Forwarded to Task III for test.
10.	VM-300 Nuclear Metals Powder Item 13, Table III	3.12" ϕ x 10"	2000°F	11.5x	As extruded Figure 33 Long. 100x	Forwarded to Task III for test.
11.	VM-300 Nuclear Metals Powder -35 mesh.	3.12" ϕ x 10"	2000°F	11.5x	As extruded Figure 34 Long. 100x	Forwarded to Task III for test.
12.	IMT Ht. No. 217. Cobalt-Hafnium alloy. Cleaned powder. -4/+14 mesh Item 14, Table III	2.6" ϕ x 10"	2000°F	16x	As extruded Figure 37 Long. 100x	Forwarded to Task III.
13.	IMT Ht. No. 112 Mar M 509 "+" Cleaned powder. -4/+8 mesh Item 15, Table III	2.6" ϕ x 10"	2000°F	11.1x	As extruded Figure 38 Long. 100x	Forwarded to Task III for test.

Table V
Composition of Cobalt Base Alloys
Composition, Wt. %

Alloy	C	Cr	Ni	W	Ta	Ti	Zr	Hf	Mo	O	Co
1. Mar M 509 IMT III Powder Analysis	0.62	25.6	12.4	6.87	2.75	0.14	0.35	---	---	0.019	Bal
2. Mar M 509 "+" IMT II2 Powder Analysis	0.76	26.6	12.5	6.51	3.07	0.16	2.24	---	---	0.071	Bal
3. Cobalt-Hafnium IMT 217 Nominal Comp.	0.25	20	10	---	---	---	---	5.0	7.5	---	Bal

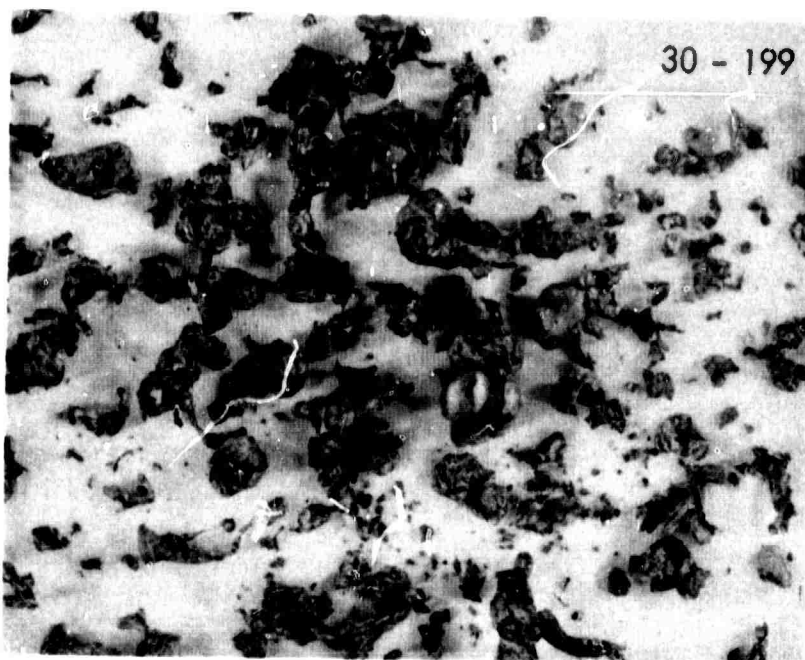


Figure 1. IN-100. Heat No. 199, as atomized, steam. 1X.

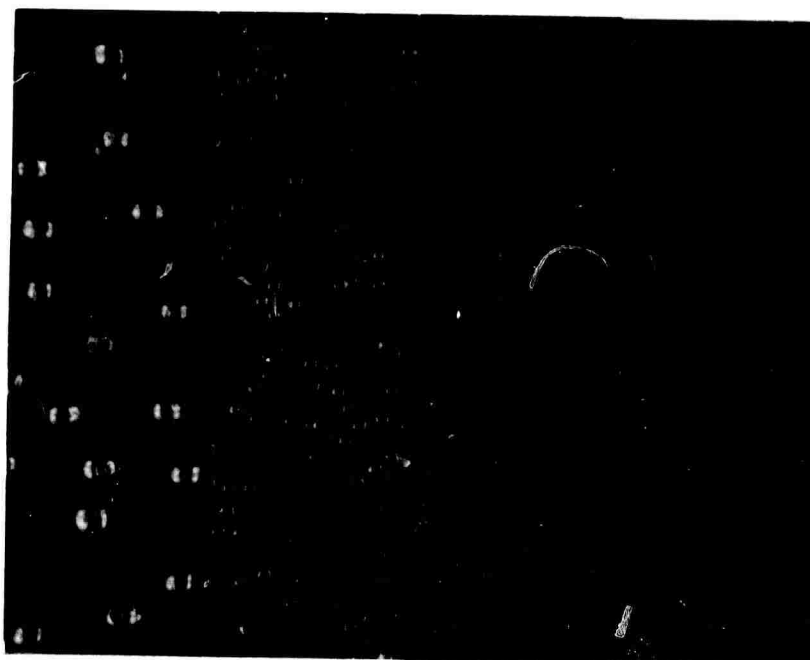


Figure 2. VM-300. Heat No. 218, cleaned 5 cycles +1600°F H₂ anneal. Size fractions l. to r. -4/+5, -8/+10, -16/+18, and -25/+30. 1X.

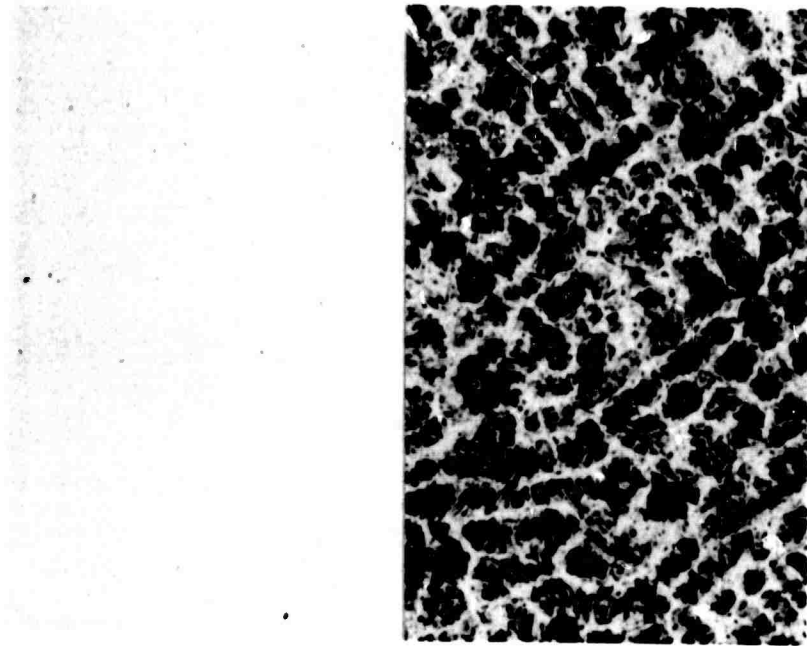


Figure 3. VM-300. Heat No. 218, -4/+5 mesh (4.3 mm)
unetched l, etched r. Dendrite arm spacing
~ 6.4 microns. 500X.

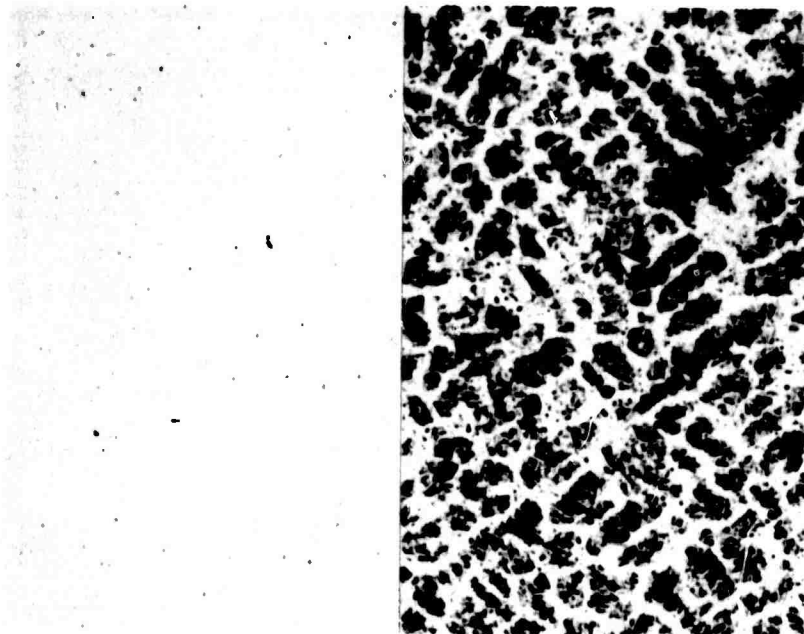


Figure 4. VM-300. Heat No. 218, -8/+10 mesh (2.0 mm)
unetched l, etched r. Dendrite arm spacing
~ 6.6 microns. 500X.

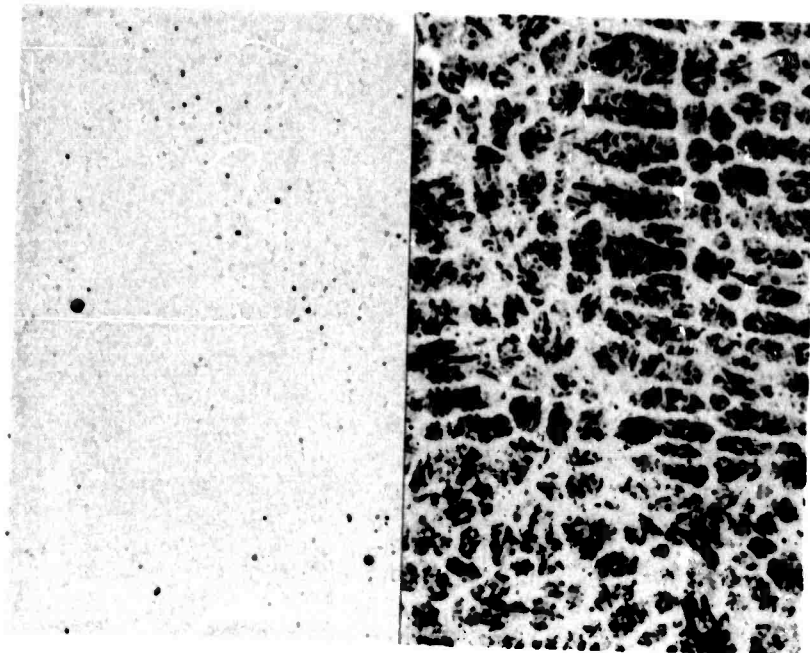


Figure 5 VM-300. Heat No. 218, -16/+18 mesh (1.0 mm)
unetched l, etched r. Dendrite arm spacing
~ 6.6 microns. 500X.

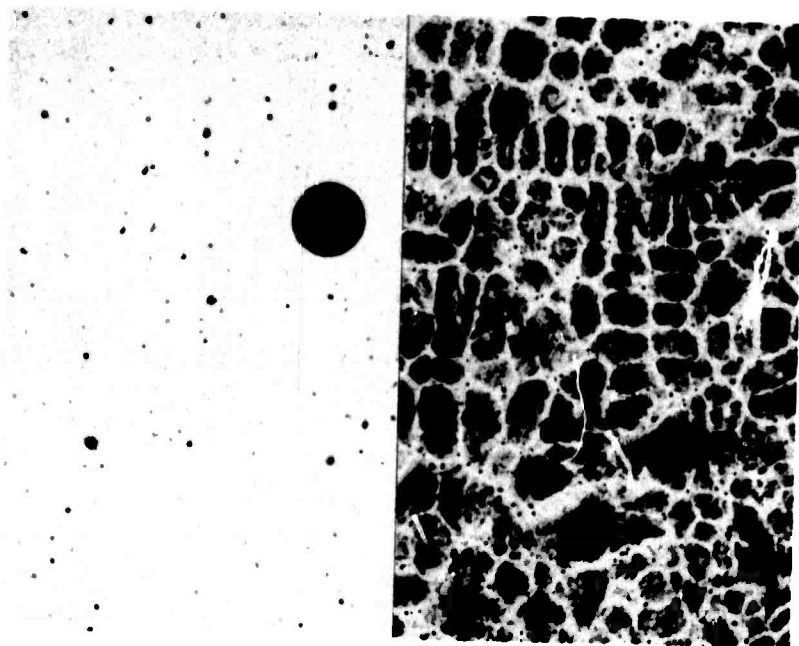


Figure 6. VM-300. Heat No. 218, -25/+30 mesh (0.6 mm)
unetched l, etched r. Dendrite arm spacing
~ 5.2 microns. 500X.

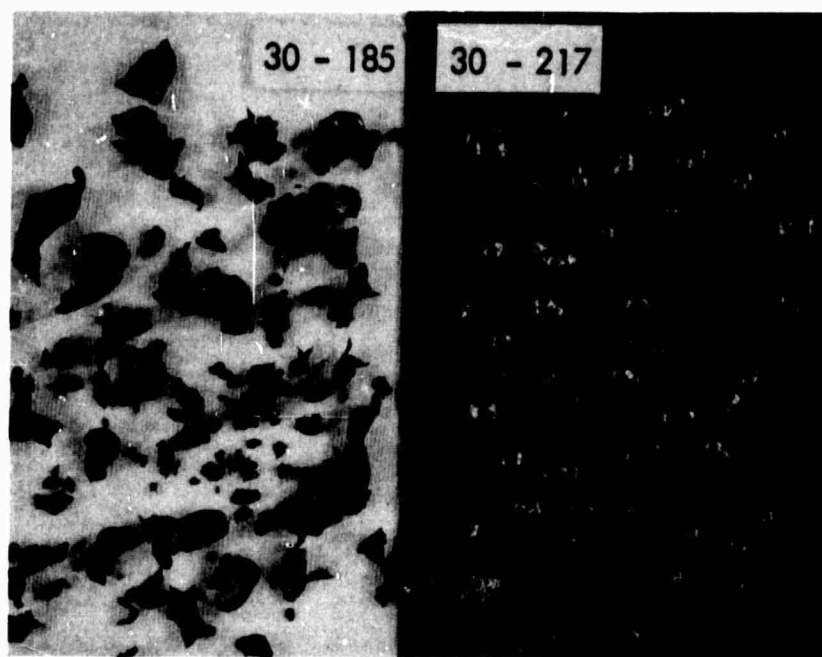


Figure 7. Cobalt-Hafnium Alloy. Heat No. 185 as atomized, no melt additions, left. Heat No. 217, cleaned, Si & B melt additions, right. 1X.

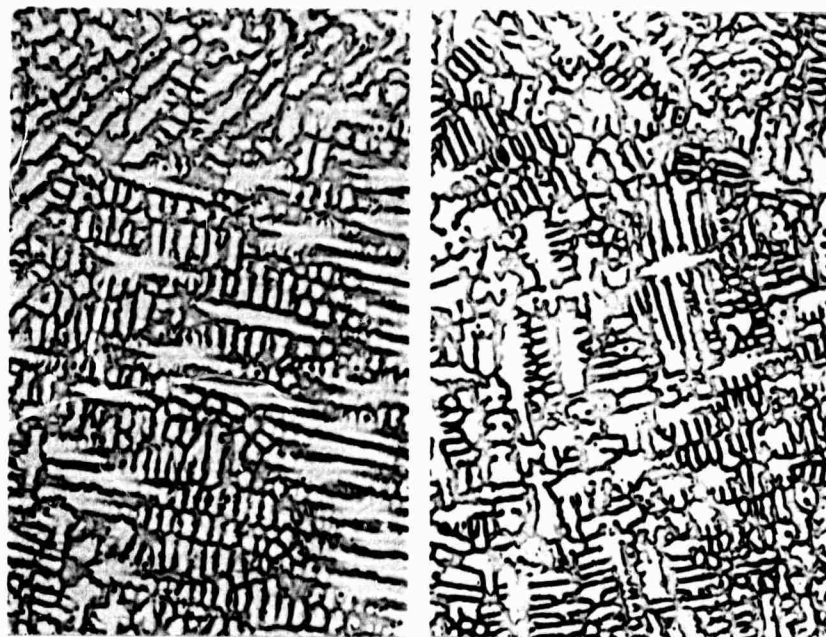


Figure 8. Cobalt-Hafnium Alloy. Heat No. 185, left D.A.S. ~ 3.1 microns; Heat No. 217 right, D.A.S. ~ 2.8 microns. Etched 500X.



Figure 9. IN-100. Federal Mogul, -60 mesh. HIP @ 2100°F, 15,000 psi, 2 hours. As pressed. Etched. 500X.

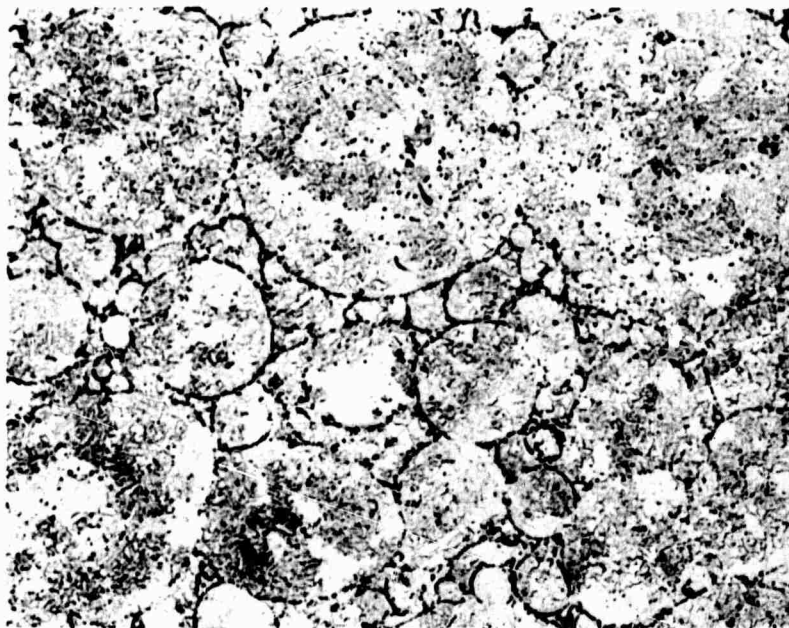


Figure 10. IN-100. Federal Mogul, -60 mesh. HIP @ 2200°F, 15,000 psi, 2 hours. As pressed. Etched. 500X.

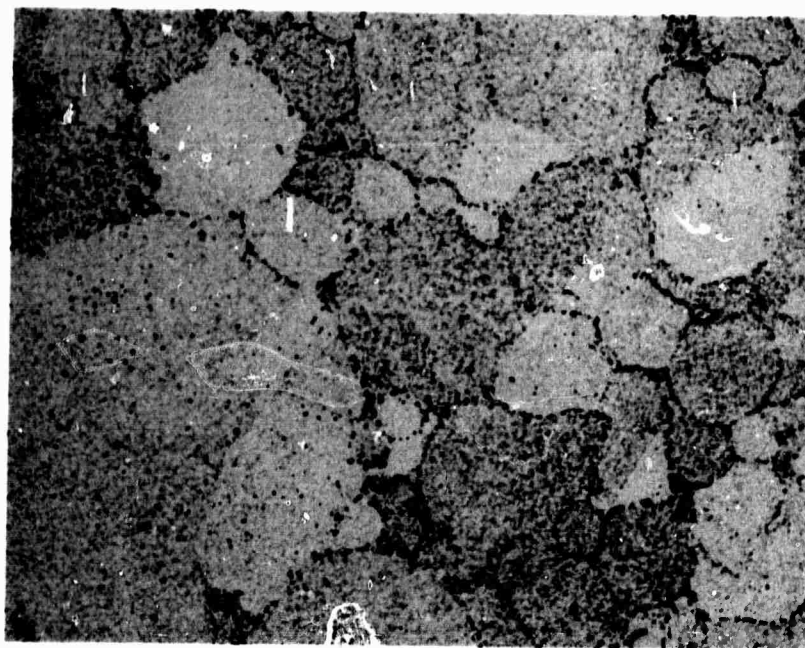


Figure 11. IN-100. Federal Mogul, -60 mesh. HIP @ 2320°F, 29,500 psi, 2 hours. As pressed. Etched. 500X.

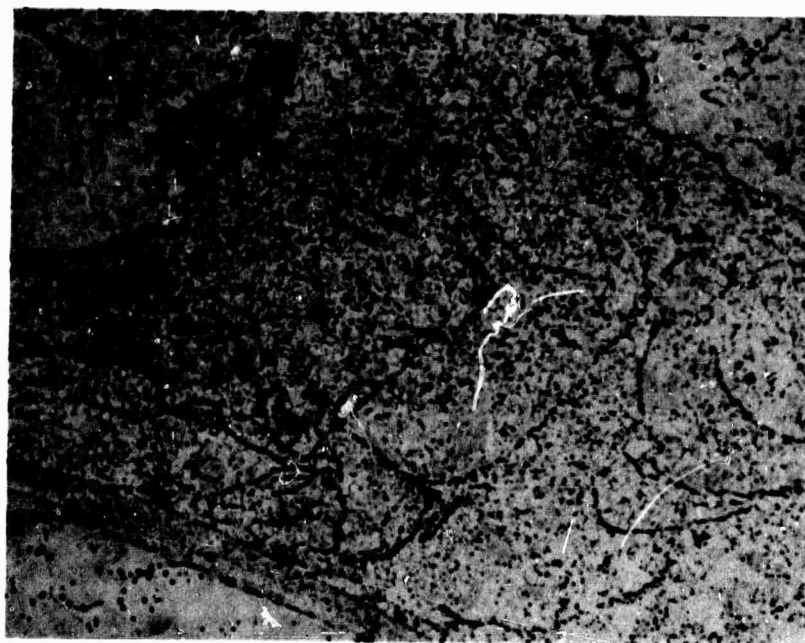


Figure 12. IN-100. Homogeneous Metals, -20/+40 mesh. HIP @ 2000°F, 25,000 psi, 2 hours. As pressed. Etched. 500X.

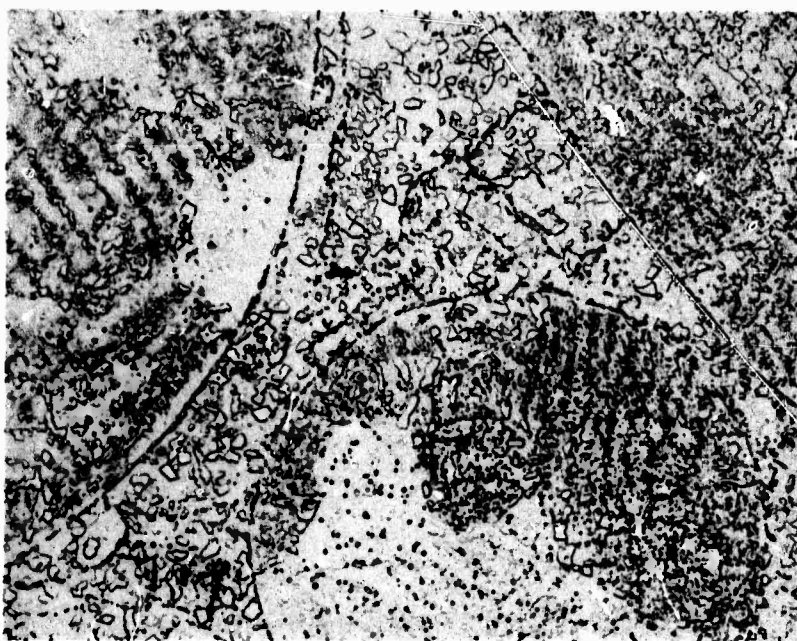


Figure 13. IN-100. Homogeneous Metals, -20/+40 mesh.
HIP @ 2000°F, 25,000 psi, 2 hours + 2100°F
solution, 4 hours. A.C. Etched. 500X.

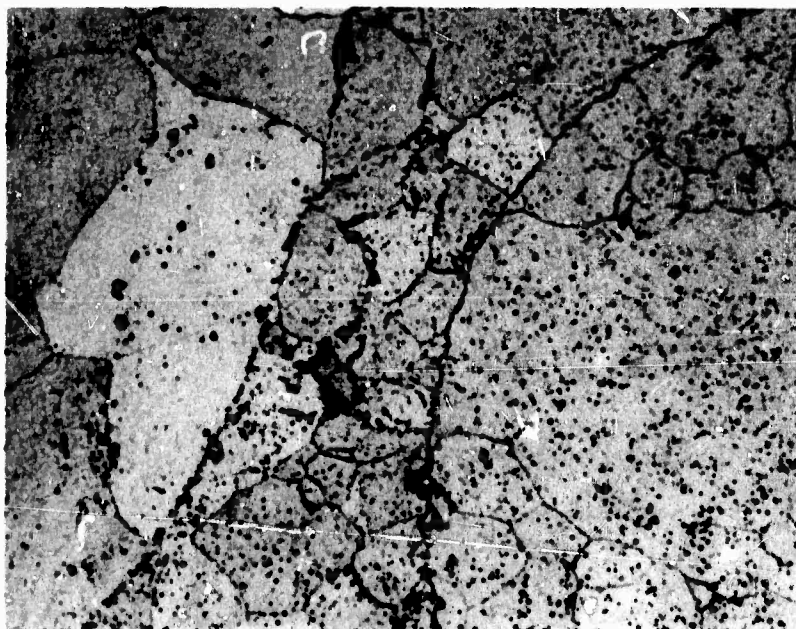


Figure 14. IN-100. Homogeneous Metals, -20/+40 mesh.
HIP @ 2000°F, 25,000 psi, 2 hours + 2200°F
solution, 4 hours. A.C. Etched. 500X.

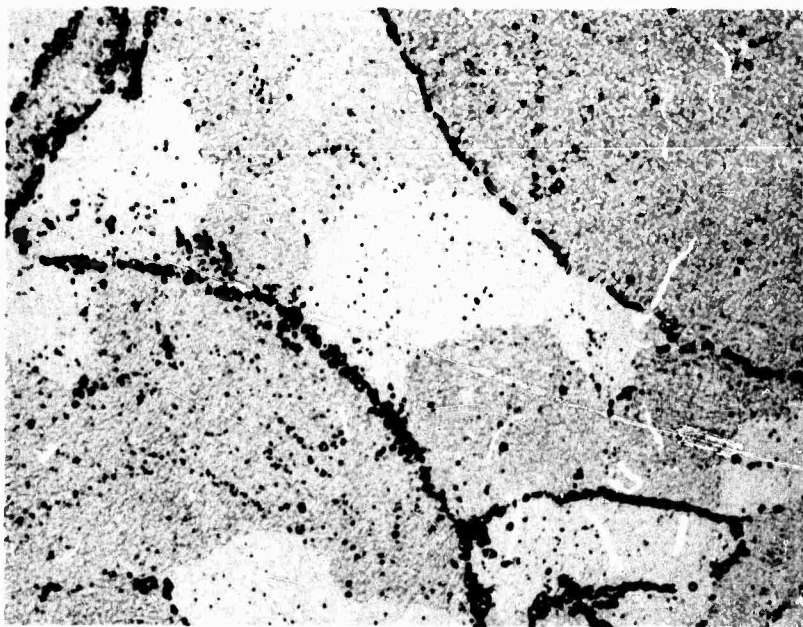


Figure 15. IN-100. Homogeneous Metals, -20/+40 mesh.
HIP @ 2300°F, 25,000 psi, 2 hours. As pressed.
Etched. 500X.



Figure 16. IN-100. Homogeneous Metals, -20/+40 mesh.
HIP @ 2300°F, 25,000 psi, 2 hours + 2200°F
solution, 4 hours. A.C. Etched. 500X.

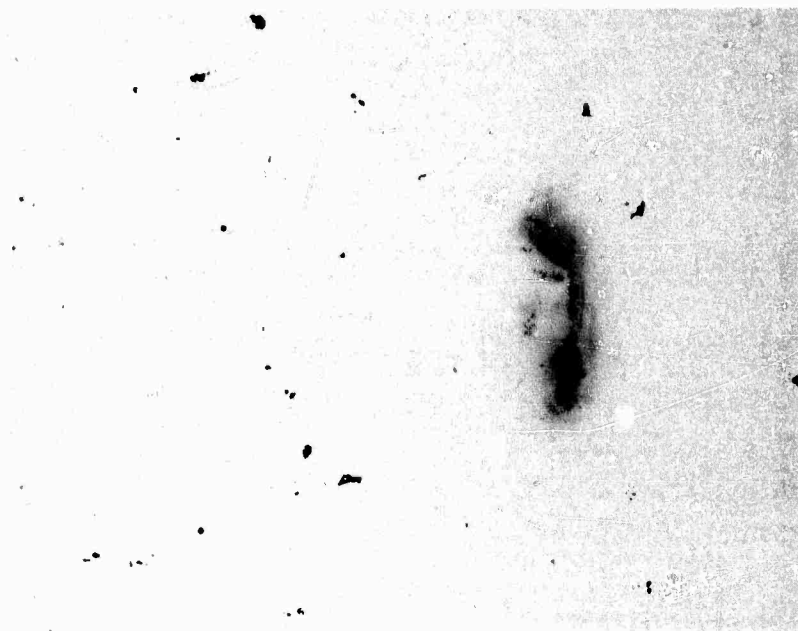


Figure 17. IN-100. Homogeneous Metals, -20 mesh.
HIP @ 2300°F, 15,000 psi, 1 1/4 hours. As
pressed. Unetched. 100X.

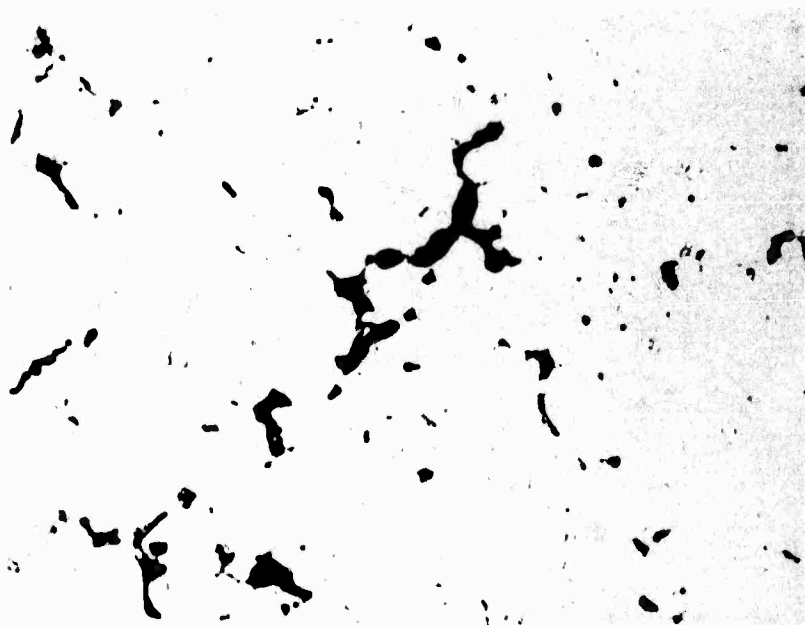


Figure 18. IN-100. Homogeneous Metals, -20 mesh.
HIP @ 2300°F, 15,000 psi, 1 1/4 hours +
2300°F solution, 4 hours. A.C. Unetched.
100X.

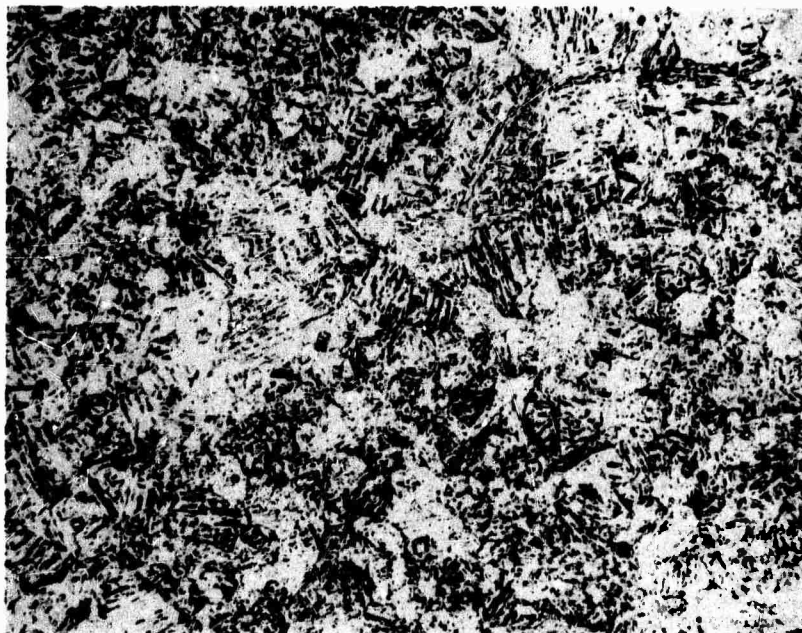


Figure 19. VM-300. IMT 136, -4/+14 mesh. Cleaned.
HIP @ 2300°F, 25,000 psi, 2 hours. As pressed.
Etched. 100X.

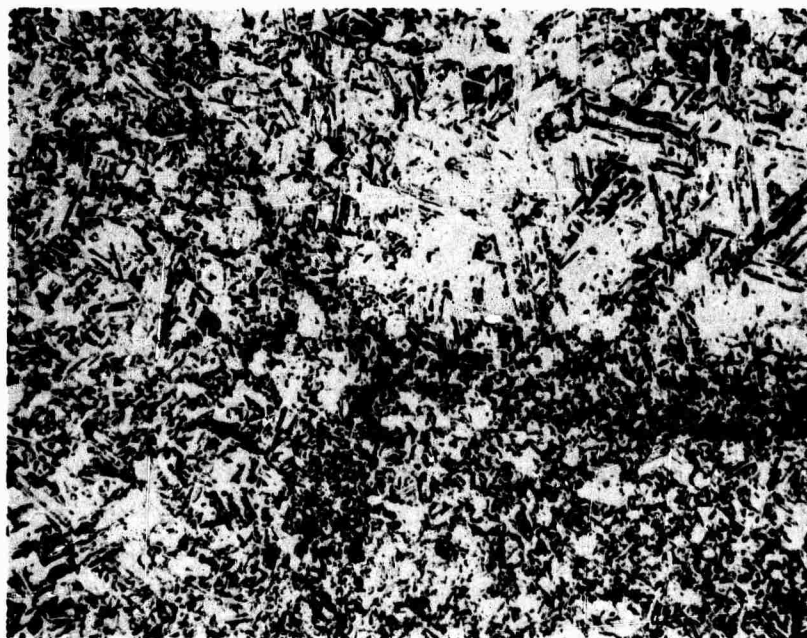


Figure 20. VM-300. IMT 137, -4/+14 mesh. Cleaned.
HIP @ 2000°F, 25,000 psi, 2 hours. As pressed.
Etched. 100X.



Figure 21. VM-300. Homogeneous Metals, -20 mesh. HIP @ 2300°F, 14,500 psi, 1 hour. As pressed. Etched. 100X.



Figure 22. VM-300. Nuclear Metals, -35 mesh. HIP @ 2200°F, 14,500 psi, 1 hour. As pressed. Etched. 100X.

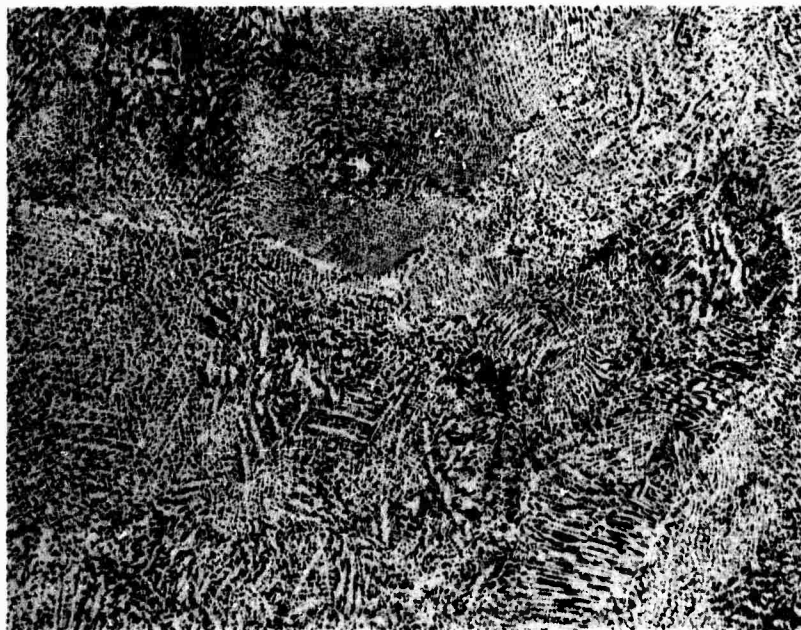


Figure 23. MAR M 509. IMT 111, -8/+14 mesh, cleaned.
HIP @ 2175°F, 15,000 psi, 1 hour. As pressed.
Etched. 100X.



Figure 24. MAR M 509. IMT 111, -8/+14 mesh, cleaned.
HIP @ 2175°F, 15,000 psi, 1 hour. As pressed.
Etched. Interparticle boundaries. 500X.



Figure 25. MAR M 509 "+". IMT 112, -8/+14 mesh, cleaned. HIP @ 2175°F, 15,000 psi, 1 hour. As pressed. Etched. 100X.



Figure 26. MAR M 509. IMT 111, -4/+8 mesh, cleaned. HIP @ 2300°F, 15,000 psi, 1 hour. As pressed. Etched. 100X.



Figure 27. Cobalt-Hafnium Alloy. IMT 217, -4/+14 mesh, cleaned. HIP @ 2100°F, 14,500 psi, 1 hour. As pressed. Etched. 100X.



Figure 28. MAR M 509 "+". IMT 112, -4/+8 mesh, cleaned. HIP @ 2100°F, 14,500 psi, 1/2 hour. As pressed. Etched. 100X.

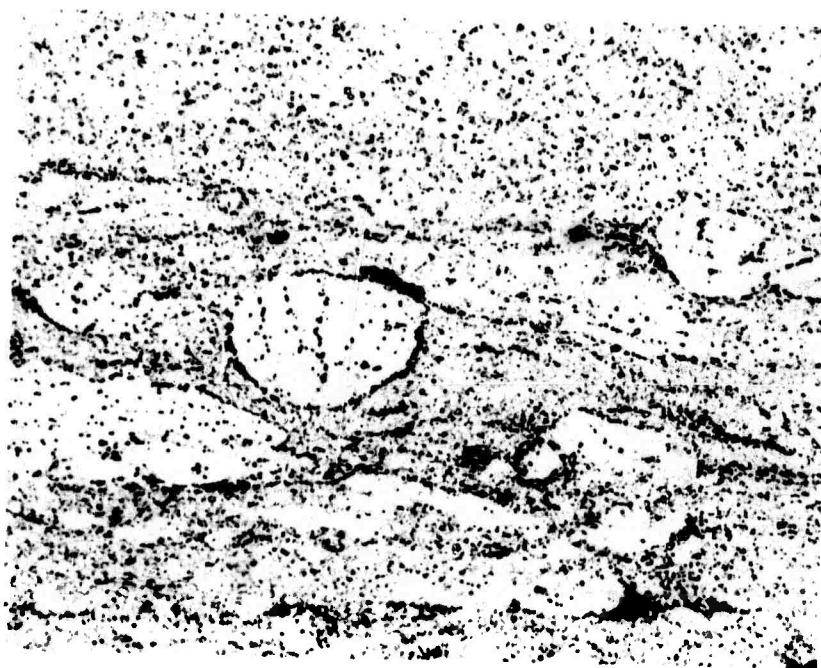


Figure 29. IN-100. HIP compact No. 10, Table III. Extruded 14.3 x @ 2000°F. As extruded. Longitudinal section. 100X.

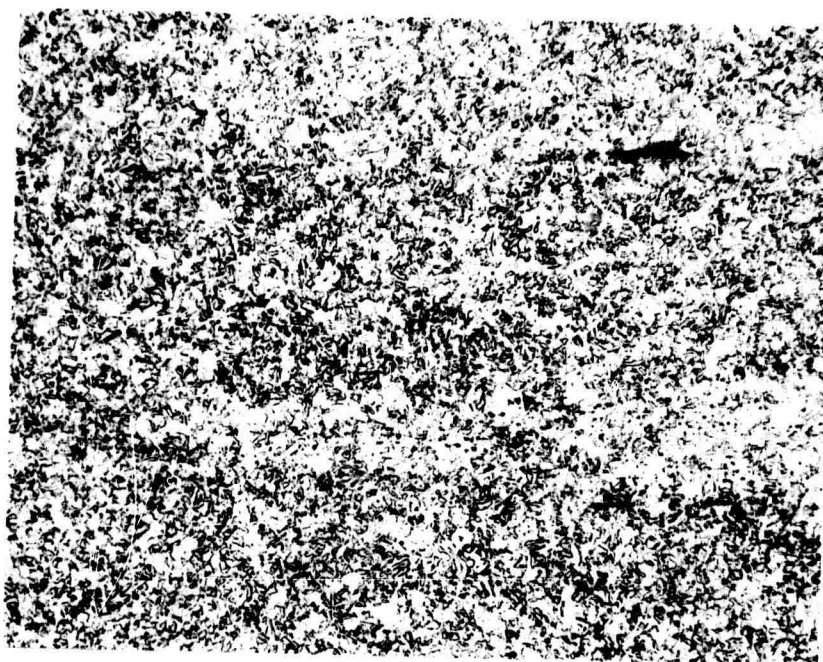


Figure 30. VM-300. IMT 148. -4/+35 mesh, cleaned and H₂ annealed. Extruded 10.5 x @ 2050°F. As extruded. Longitudinal section. 100X.

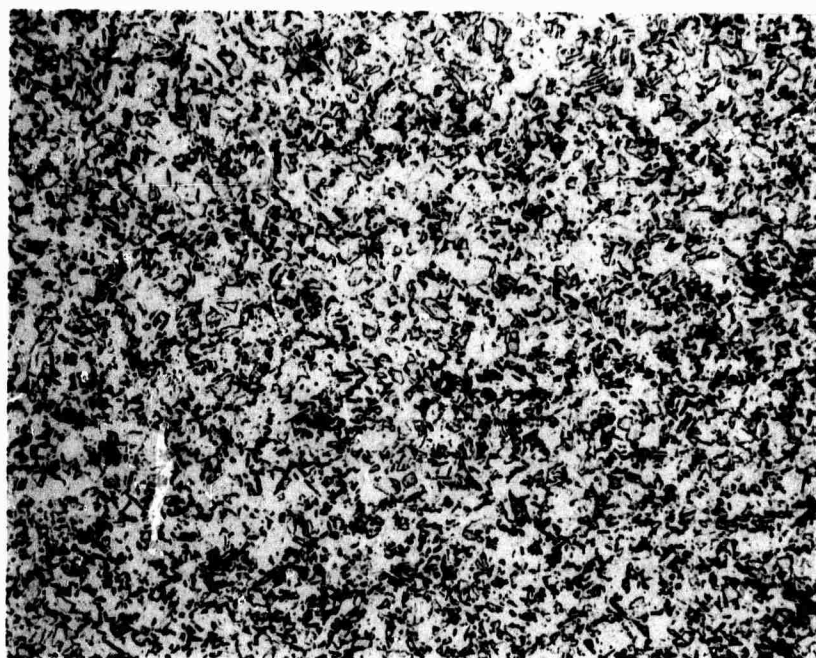


Figure 31. VM-300. HIP compact No. 11, Table III.
Extruded 14.3 x @ 2000°F. As extruded.
Longitudinal section. 100X.

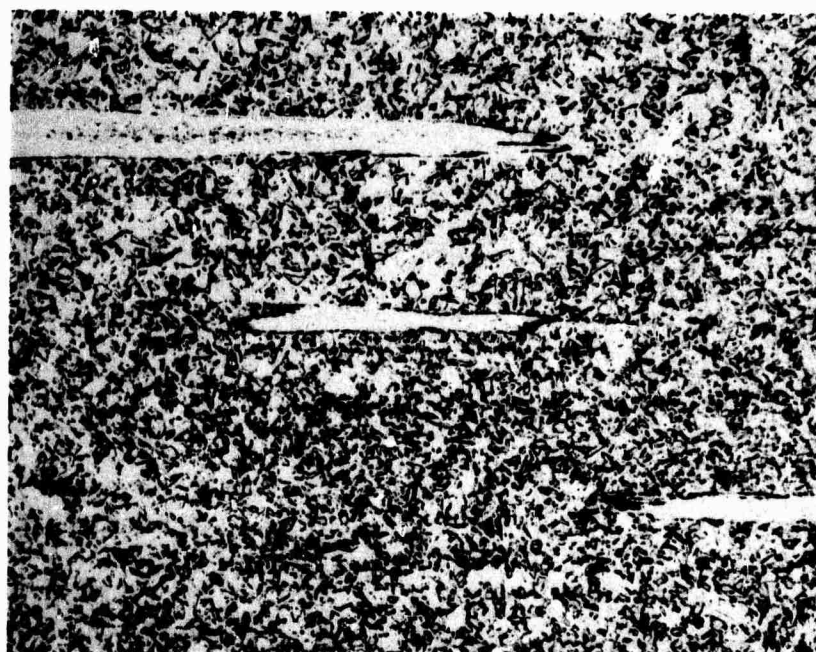


Figure 32. VM-300. Homogeneous Metals. -20 mesh.
Extruded 14.3 x @ 2000°F. As extruded.
Longitudinal section. Etched. 100X.

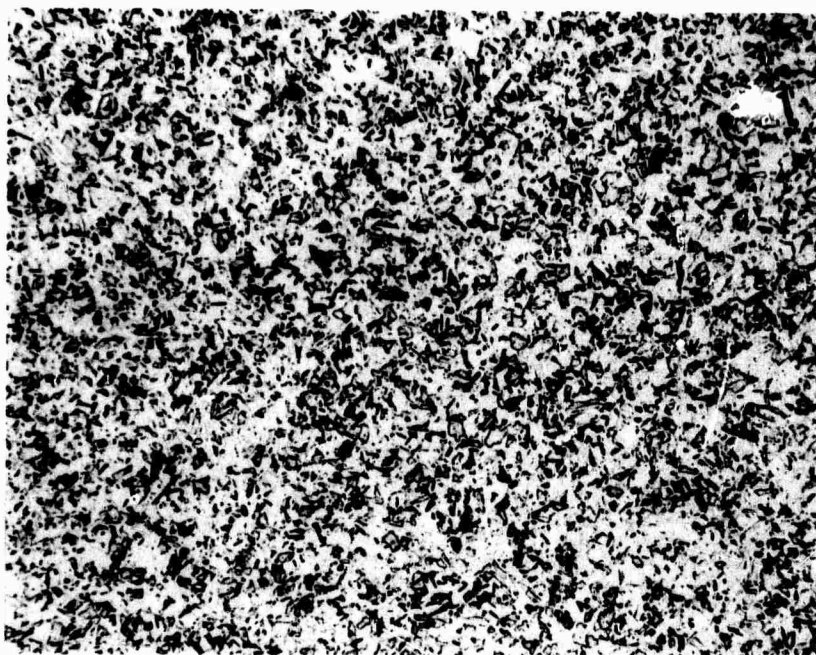


Figure 33. VM-300. HIP compact No. 13, Table III. Extruded 11.5 x @ 2000°F. As extruded. Longitudinal section. Etched. 100X.

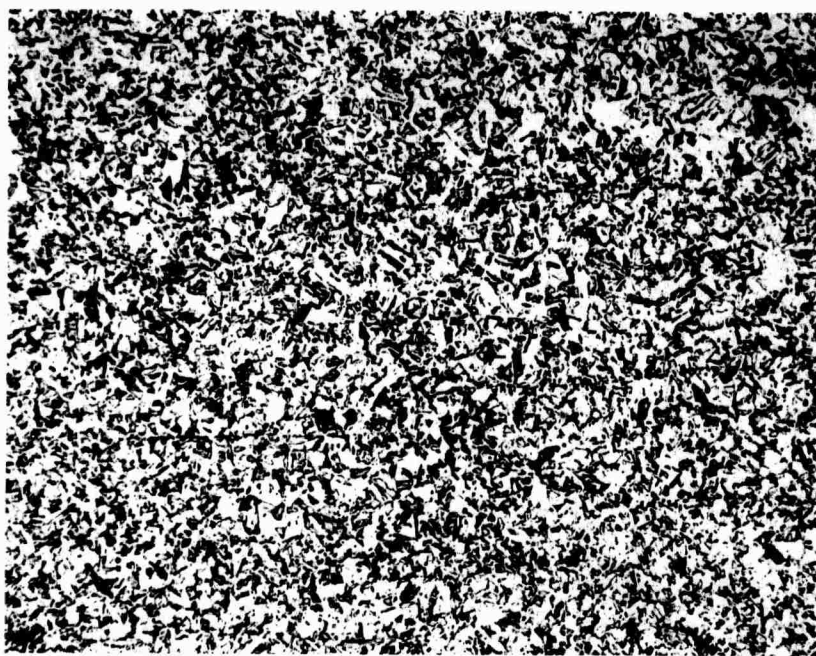


Figure 34. VM-300. Nuclear Metals, -35 mesh. Extruded 11.5 x @ 2000°F. As extruded. Longitudinal section. Etched. 100X.



Figure 35. MAR M 509. HIP compact No. 12, Table III.
Extruded 15.2 x @ 2000°F. As extruded.
Longitudinal section. Etched. 100X.

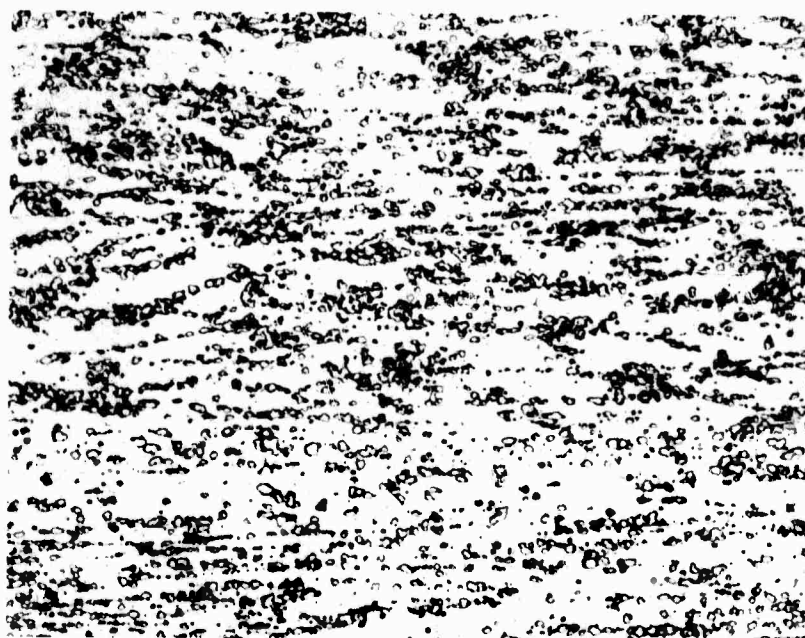


Figure 36. MAR M 509. HIP compact No. 12, Table III.
Extruded 15.2 x @ 2000°F. As extruded.
Longitudinal section. Etched. 500X.

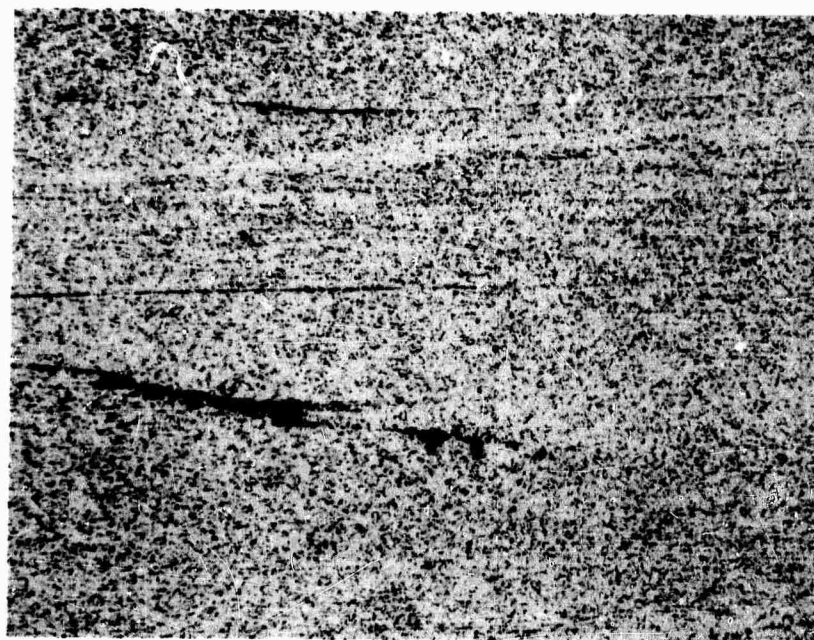


Figure 37. Cobalt-Hafnium Alloy. HIP compact No. 14, Table III. Extruded 16 x @ 2000° F. As extruded. Longitudinal section. Etched. 100X.

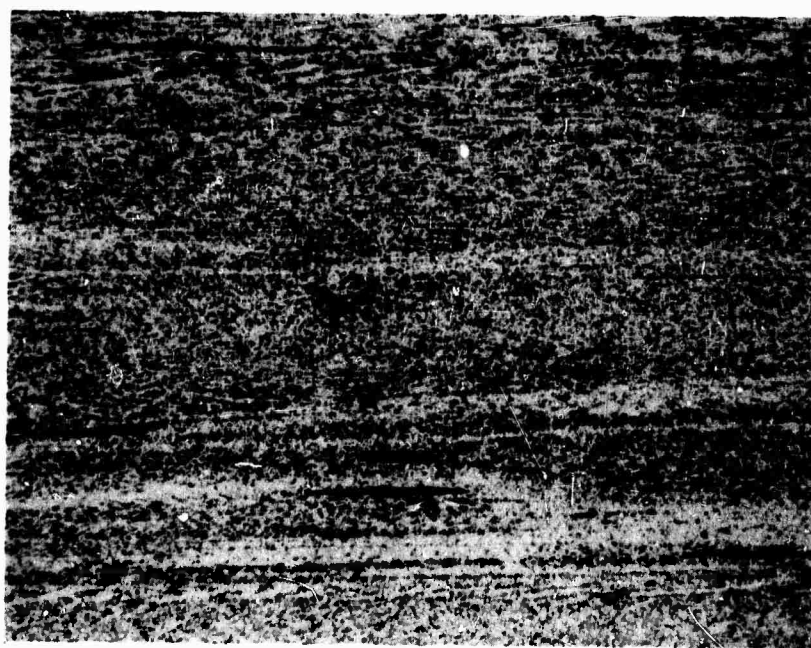


Figure 38. MAR M 509 "+". HIP compact No. 15, Table III. Extruded 11.1 x @ 2000° F. As extruded. Longitudinal section. Etched. 100X.

(1)

TASK II - SOLIDIFICATION RESEARCH

by

P. A. Joly
R. G. Riek
R. Mehrabian
M. C. Flemings

ABSTRACT

The effect of a wide range of cooling rates (0.1 to 10^{50} C/sec) on the dendritic structure of Maraging 300 alloy is determined, and the relationship $d = 39\epsilon^{-0.25}$ between secondary dendrite arm spacing, d , and cooling rate, ϵ , is established. Structures of atomized powders of Maraging 300 and IN-100 alloys are studied. Cooling rates during atomization of Maraging 300 alloy are 10^2 to 10^{30} C/sec with resulting secondary dendrite arm spacings of 5 to 12 microns, in particles of 0.5 to 4.5 mm in diameter. A heat flow analysis is given to predict solidification time during atomization.

A method for rapid solidification of rods of Maraging 300 and IN-100 alloys is described. Dendritic structures and measured secondary dendrite arm spacings of these rods are presented. In 5/16" by 5/16" cross section rods of Maraging 300 and IN-100 alloys, the largest secondary dendrite arm spacings are 15 and 17 microns respectively.

A process for consolidation of the rapidly solidified rods into billets is developed which entails nickel plating the rods before hot extrusion. Mechanical properties of samples machined from consolidated billets are as high as 276 ksi U.T.S., 268 ksi Y.S., 46% reduction in area, and 6.5% elongation. It is proposed that continuously cast small cross-section rods of Maraging 300 or IN-100 alloys could be used as an alternate starting material to obtain sound large billets with very fine segregate spacings.

INTRODUCTION

In the first year of this program, Task II (solidification group) has conducted research on heat flow, microsegregation of maraging 300 and IN-100 alloys and on consolidation of rapidly solidified rods of maraging 300 alloy. The general aim of the program has been, (a) the study of heat flow and structure of the atomized particles (flakes, droplets, pellets) produced at IMT, (b) the production of rapidly solidified rods of metal alloys, (c) the study of consolidation of these rods by hot extrusion or hot gas isostatic pressing.

Specific aspects of the work have included:

1. Determination of the relationship between cooling rate and secondary dendrite arm spacing for maraging 300 alloy.
2. Detailed study of heat flow and metallography of atomized powders of maraging 300 alloy and the effects of atomization medium and temperature on their structure.
3. Development of melting and casting techniques for rapid solidification of rods of maraging 300 and IN-100 alloys.
4. Study of bonding characteristics of the rapidly solidified rods during consolidation into billets by hot extrusion and hot gas isostatic pressing. Finally, measurement of mechanical properties of these consolidated billets.

1. EFFECT OF COOLING RATE ON STRUCTURE OF MARAGING 300 ALLOY

Cooling rate during solidification has a pronounced effect on cast structures, particularly on fineness of dendrite structure and of associated inclusions and microporosity. In order to ascertain the influence of processing variables on cooling rates and solidification structures of maraging 300 alloy, the following study was undertaken.

The effect of cooling rate on secondary dendrite arm spacing over a wide range of cooling rates, $0.1^{\circ}\text{C}/\text{sec}$ to $10^5^{\circ}\text{C}/\text{sec}$, was determined. The various cooling rates were obtained by levitation melting and casting of small droplets (1 to 2 grams), unidirectional solidification of a 2.5 Kg. ingot, and vacuum melting of 700 gm charge in an alumina crucible and furnace cooling.

Levitation Melting and Casting

Figure 1 is a sketch of the levitation melter and associated apparatus. The details of this apparatus have previously been described(1). Droplets of the maraging 300 alloy were levitated inside the glass tube in an atmosphere of helium. The temperature of the droplets was continuously monitored using a two-color optical pyrometer. The molten levitated droplets were solidified and cooling rates measured using the following techniques:

(a) Gas Quenching. With sufficiently high flow rates of hydrogen or helium, droplets were solidified while levitated. Measured cooling rates, via the two-color optical pyrometer were of the order of $1 - 15^{\circ}\text{C}/\text{sec}$,

(b) Oil Quenching. Somewhat higher cooling rate was obtained by liquid quenching. The liquid quench tank was placed where the splat cooler is shown in Figure 1; the power to the levitation coil was turned off, and the charge dropped through the plastic seal into the liquid. A cooling rate of $140^{\circ}\text{C}/\text{sec}$ has been calculated for oil quenching(2).

(c) Chill Casting. Chill castings in a copper mold with plate shaped mold cavity of 0.08" thickness, inserted in the turntable in the enclosure in Figure 1, were made and cooling rates on the order of $10^3^{\circ}\text{C}/\text{sec}$ were measured as previously described.(1)

(d) Splat Cooling. Maximum cooling rates (on the order of $10^5^{\circ}\text{C}/\text{sec}$) were obtained using the hammer and anvil type splatter shown in Figure 1. The details of this technique have again been described elsewhere(1).

Unidirectional Casting

A 2" by 2" by 5" tall unidirectional ingot of maraging 300 was cast using a composite mold of CO_2 sand and insulating molding material, fiberchrome. A water-cooled stainless steel chill was located at the base opening of the mold. Thermal measurements were made by

utilization of four Pt-Pt/10% Rh silica shielded thermocouples located along the length of the ingot mold. Measured cooling rates and secondary dendrite arm spacings at different locations in this ingot are shown in Figure 2.

Vacuum Melting and Furnace Cooling

Several specimens of maraging 300 alloy weighing approximately 700 grams were vacuum melted in an alumina crucible in a Balzer furnace. These samples were solidified inside the crucible by decreasing the power input to the furnace at different rates and temperature profiles were recorded with a Pt-Pt/10% Rh thermocouple inserted in the melt. Results of cooling rates versus dendrite arm spacings are again shown in Figure 2.

The microstructure of maraging 300 alloy is shown qualitatively to be refined by increased cooling rates in Figure 3. Figure 2 is a plot of the secondary dendrite arm spacing versus cooling rates. Secondary dendrite arm spacing varies linearly with cooling rate on this log-log plot over the range of cooling rates studied. Equation of the experimentally determined relationship is:

$$d = 39\epsilon^{-0.25}$$

where d is secondary dendrite arm spacing in microns and ϵ is the cooling rate dT/dt in $^{\circ}\text{C}/\text{sec}$,

2. ANALYSIS OF STRUCTURE AND HEAT FLOW OF ATOMIZED POWDERS

During the course of this investigation, several batches of atomized coarse powder samples of maraging 300 alloy were received from IMT. A detailed study of the structures coupled with data developed in the previous section have facilitated a simple heat flow analysis during atomization.

Structure of Atomized Powders

The structures of steam, argon, nitrogen, and vacuum atomized powders were evaluated using fineness of dendritic structure and porosity as criteria. Table I shows the different series of coarse powders received from IMT and Table II and Figure 4 give results of measured secondary dendrite arm spacings versus diameters of atomized powders. The results show that:

- (a) average secondary dendrite arm spacings increase with increasing size of atomized powders,
- (b) in the maraging 300 alloy, different types of dendritic morphologies were observed: (i) some of the steam or gas atomized powders show many colonies of dendrites, whose primary axis is perpendicular to the surface. This type of morphology corresponds to a high rate of heat extraction due to good heat transfer at the surface of the droplets during

atomization, Figure 5. (ii) A second type of dendritic morphology observed is shown in Figure 6. The center of the dendrite arms appears to be white, indicating high nickel content. This same type of structure has previously been observed in undercooled specimens of Fe-25%Ni alloys(3). (iii) In steam atomized coarse powders, there is a tendency towards a duplex dendritic structure, Figure 7. The finer dendrites are on the outside layer of the pellets and the coarser on the inside. It appears that these larger pellets were only partially solidified during flight; thus the finer spacings on the outside edges of the samples. The coarser structures must have resulted from quenching in the water bath below. The steam formation around each pellet in the water bath must cause a reduction in the heat transfer coefficient, hence the coarse structures. (iv) A typical structure of a vacuum atomized powder of maraging 300 alloy is shown in Figure 8.

- (c) In general, steam atomized powders exhibit a larger amount of gas porosity than argon atomized powders, Figure 9.
- (d) Figure 10 shows a typical structure of vacuum atomized powder of IN-100 alloy.

Effect of Atomization Medium on Secondary D.A.S.

A careful examination of secondary D.A.S. measurements of maraging 300 alloy in Heats No. 30-137, 30-147, 30-148, 30-172, 30-173, 30-174, and 30-176 shows that there is no direct correlation for a given size particle between the three atomization media used and resulting dendrite

arm spacings. As example, Table III gives the values of measured secondary D.A.S. for droplets in the size range -16/+18 quenched in three different atomization media.

On the other hand, vacuum atomized droplets of maraging steel, obtained from Homogeneous Material, have slightly larger secondary D.A.S. than steam, argon, or nitrogen atomized droplets of the same size range, Table II.

The slower cooling rates obtained in vacuum atomization is due to the absence of convective heat flow. Even though convective heat flow is only a small part of the overall heat flow process in atomization, it does manifest itself by the larger segregate spacings of powders atomized in vacuum.

Effect of Tap Temperature on Secondary D.A.S.

There is a definite relationship between tap temperature and secondary dendrite arm spacings, especially for the coarser particles as shown in Figure 11. Lowering tap temperature leads to finer dendrite arm spacings.

Heat Flow During Atomization

Newton's Law of cooling for a spherical droplet with "h controlled" heat transfer is written:

$$hA(T - T_o) = C_p \rho V \frac{dT}{dt} \quad (1)$$

where:

T_o = medium temperature, $^{\circ}\text{C}$

T = temperature of droplet, $^{\circ}\text{C}$

A = area of the specimen, cm^2

V = volume of the specimen, cm^3

ρ = density of the specimen, gcm^{-3}

C_p = specific heat of the specimen, $\text{cal.g}^{-1}\text{C}^{-1}$

h = heat transfer coefficient, radiation plus convection, $\text{cal.cm}^{-2}\text{sec.}^{-1}\text{C}^{-1}$

$dT/dt = \epsilon$ = cooling rate at temperature T , $^{\circ}\text{Csec.}^{-1}$

Using the above expression, a value for the combined heat transfer coefficient of radiation and forced convection during atomization may be calculated from cooling rates obtained from Figure 2, using measured secondary dendrite arm spacings of atomized droplets. For example, measured secondary dendrite arm spacing of an atomized droplet, of maraging 300 alloy 1mm in diameter, is about 7 microns, Figure 4. From Figure 2 we can estimate a corresponding cooling rate of 10^{30}C/sec during atomization. Using the values of heat capacity and density, of Fe-25% Ni alloy* and atomization temperature of 1500°C , the value of $h = 0.0095 \text{ cal/cm}^2\text{sec}^{\circ}\text{C}$ is calculated.

* For Fe-25% Ni alloy, the following values have been reported (1,2):
 $C_p = 0.107 \text{ cal/g } ^{\circ}\text{C}$, $\rho = 8\text{g/cm}^3$, Latent heat of fusion, $H = 72 \text{ cal/g}$,
 and thermal conductivity, $k = 0.115 \text{ cal/cm.sec}^{\circ}\text{C}$.

Ranz and Marshall (4) in studies of forced convection around a sphere derived the following equations for the Nusselt number, Nu:

$$Nu = \frac{hD}{k_f} = 2.0 + 0.6 \sqrt{Re Pr^{2/3}} \quad (2)$$

where:

$$\text{Prandtl number } Pr = \left(\frac{C_p \mu}{k_f} \right)$$

and

$$\text{Reynolds number } Re = \frac{Dv\rho_f}{\mu_f}$$

"f" refers to properties of the film around the sphere.

D = diameter of sphere, cm

v = velocity of fluid stream away from sphere, cm.sec⁻¹

μ_f = viscosity of fluid film, poise

k_f = thermal conductivity of fluid film, cal.sec⁻¹ cm⁻¹ °K⁻¹

C_p = specific heat of fluid film, cal.grm.⁻¹ °K⁻¹

h = heat transfer coefficient, cal.cm⁻² sec⁻¹ °C⁻¹

ρ_f = density of fluid film g cm⁻³

Assuming a velocity of 80 cm/sec during steam atomization and a droplet diameter of 1mm, calculated value of heat transfer coefficient from equation (2) is 0.9×10^{-3} cal. cm⁻² sec⁻¹ °C⁻¹. This value of heat transfer coefficient is in good agreement with that calculated in the previous page using data obtained from Figure 2 and equation (1).

Solidification times can also be calculated from the information available. Cooling rates of the order of 10^3 °C/sec were obtained in the thin plate chill castings made from molten levitated droplets.

These measurements were made by embedding a small Pt-Pt/10% Rh thermocouple (No. 38 wire) in the side of the plate casting. The output was recorded on an oscilloscope giving cooling curves over a temperature range of 1425°C to 1300°C. It is assumed that the rate of heat extraction during solidification is equal to the rate of heat extraction over this temperature range. A heat balance for the "h controlled" heat flow is made and solidification time computed from:

$$q = C_p \rho V \frac{dT}{dt} = H_p \frac{V}{t_f} \quad (3)$$

where dT/dt is measured cooling rates in the temperature range above, in the solid, and t_f = solidification time, seconds, thus

$$t_f = \left(\frac{H}{C_p} \right) / \left(\frac{dT}{dt} \right) \quad (4)$$

Using the predicted cooling rate of 10^{30} C/sec for a 1mm droplet of maraging 300 alloy, a solidification time of $t_f = 0.67$ seconds is calculated from equation (4).

A second method of predicting solidification time theoretically has been outlined in a recent publication by Szekely and Fisher⁽⁵⁾. They have considered solidification of a metal droplet due to thermal radiation alone. A very simple asymptotic solution is given, which is valid for the size range of atomized droplets under consideration here. The equations of interest are:

$$2R/D = (1 - Ct)^{1/3} \quad (5)$$

$$C = - \frac{6 \sigma E}{DH\rho} [T_e^4 - (T_{mp} + 273)^4] \quad (6)$$

where:

T_{mp} = melting temperature of droplets, °C

R = position of the solidification front, cm

D = diameter of droplet, cm

σ = Boltzmann's constant = 1.35×10^{-2} cal/cm²sec.K⁴

E = total emissivity of the droplet

T_e = temperature of the environment, °K

When $2R/D = 0.28$, 98% of the spherical droplet is solidified. Therefore, we have used this ratio and an emissivity value of 0.5 in our calculations, with all other data same as above.

The calculated value is $C = 0.7 \text{ sec}^{-1}$ and the resulting solidification time $t_f = 1.4$ seconds. This calculated value is twice as large as that estimated from measured dendrite arm spacings and cooling rates. However, considering the fact that only heat flow by radiation is considered here and the uncertainty of the data used, the discrepancy is acceptable.

3. MELTING, CASTING, AND STRUCTURES OF RAPIDLY SOLIDIFIED RODS

(a) Melting and Casting

The starting material for melting and casting was maraging 300 and IN-100 alloys purchased in rod form. The castings were prepared in a Balzer VSG 10 vacuum induction unit with a 30 KW, 10 KC power source. A set of copper chill molds were designed and constructed to fit in this furnace. Figure 12a shows the melting and casting arrangement inside the Balzer furnace. Figure 12b shows a section of the mold used in casting of rapidly solidified alloy rods of 5/16" by 5/16" by 5" long. The charge was melted in an alumina crucible, vacuum degassed and poured at 175°C superheat. Temperatures were recorded using a Pt/Pt-10% Rh thermocouple which was shielded in an alumina protection tube.

(b) Structures

The cast product in each heat was a set of 6 rods. The structures of these rods were examined in detail and secondary dendrite arm spacings measured. Figure 13 shows the cross-sectional structure of a rapidly solidified rod of maraging 300 alloy. Figures 14 and 15 show the measured secondary dendrite arm spacings along the small dimension of the rods of maraging 300 and IN-100 alloys respectively. Our results show that chill cast rods of maraging 300 and IN-100 alloys exhibit secondary dendrite arm spacings consistently less than 15 and 17 microns, respectively. These fine structures are comparable with structures of coarse powder obtained from the atomization process.

4. BONDING CHARACTERISTICS OF RAPIDLY SOLIDIFIED RODS AND MECHANICAL PROPERTIES OF BILLETS CONSOLIDATED FROM THESE RODS

The as cast rods of maraging 300 alloy were machined to remove surface imperfections and polished down to 600 grit paper. Three billets were consolidated, each from a set of 12 rapidly solidified rods. These three billets were processed using the following techniques:

- (i) The as-cast rods were polished, canned, and hot isostatically pressed.
- (ii) The as-cast rods were polished, nickel plated, hot isostatically pressed, and finally extruded at 2000°F.
- (iii) The as-cast rods were polished, nickel plated and extruded at 2000°F.

Table IV shows the various methods used in consolidation of each set of rods and subsequent heat treatments of eight tensile specimens machined from these three billets.

(a) Nickel Plating of Rods

Surface preparation to remove imperfections was done on a milling machine and all samples were subsequently polished down to 600 grit paper. Chemical cleaning of surfaces consisted of 5 steps:

- (i) The rods were immersed in an ultrasonic bath of acid solution of 40% $H_2SO_4 + H_2O$ first as anodes for 10 seconds and subsequently as cathodes for 5 seconds at 4 volts.
- (ii) The rods were immersed in an ultrasonic bath of acid solution of 40% $HNO_3 + 10\% HF + H_2O$ for 5 seconds at zero voltage.
- (iii) The rods were immersed back in the ultrasonic bath of (i) above, as cathodes for 5 seconds at 4 volts.
- (iv) The rods were rinsed in deoxidized water for 10 seconds.

- (v) A 0.0002" layer of nickel sulphamate was deposited on the rods by electroplating.

Rods thus prepared were stored in acetone or freon for subsequent canning before hot isostatic pressing and/or hot extrusion.

(b) Hot Isostatic Pressing

After surface preparation the rods were wrapped in a mild steel foil, placed in a 1/8" thick wall steel can, and surrounded with maraging 300 alloy powder. The material was then degassed at 500°F for 3 hours to a pressure of 2×10^{-5} mm Hg and sealed in the can.

Two different treatments were used during hot isostatic pressing. The first unplated set of rods were pressed for 1 hour at 2250°F under 30,000 psi pressure of helium. The next set of rods, which were nickel plated, were pressed for 1-1/2 hours at 2150°F under 15,000 psi pressure of helium and subsequently hot extruded.

(c) Hot Extrusion

The two billets that were hot extruded were:

- (i) The nickel plated rods that had already been hot isostatically pressed.
- (ii) The nickel plated rods that were directly hot extruded.

In each of these two billets the starting material was wrapped in a mild steel foil placed in Shelby seamless tubing (1.500" I.D. x 1.975" O.D.), surrounded by mild steel powder, degassed at 0.1 mm Hg at room temperature and sealed. The liner and the die used during hot extrusion were 2.050" and 1.00" in diameter, respectively, giving a reduction ratio of 4.2.

The billets were heated up to 2000°F for 1/2 hour in an argon atmosphere and placed on the liner which was heated to 600°F and lubricated

with Delta 31. The extrusion conditions are reported in Table IV.

(d) Structures and Mechanical Properties of Billets

Cross-sectional structures of billets consolidated from the rapidly solidified rods were studied to determine the bonding characteristics of the material in the four different conditions reported. Figure 16 shows the junctions of rods after consolidation. Figure 16a shows the nonplated, hot isostatically pressed material. The cracks observed between the rods lead to poor ductility in the billets after heat treatment. Figure 16b shows the bonding obtained after plating and hot isostatic pressing. No cracks were observed between the rods. Figure 16c shows the bonding obtained after plating and hot extrusion. Finally, Figure 16d shows the bonding obtained after plating, hot isostatic pressing and hot extrusion. The width of nickel plating still observable between the rods decreased significantly after both hot isostatic pressing and extrusion due to the diffusion of the nickel to the interior of the rods. Thus it appears that a high temperature homogenization treatment after consolidation of plated rods would be a method of reducing the weaker areas between the rods. Finally, the bonds shown in Figure 16c, plated and hot extruded, have a central dark region that seems to be oxidized. This could be eliminated by canning the rods at high temperatures and better vacuum conditions, as in the case of the hot isostatically pressed samples.

Grain size measurements of the billets are reported in Table V. Hot extrusion reduced the grain size of the maraging 300 alloy from about 1 mm to 10 microns.

The mechanical properties of tensile bars machined from the three

billets are reported in Table V. The heat treatment and consolidation conditions of each of the samples are reported in Table IV. The non-plated rods did not possess any ductility due to existing cracks between the rods after hot isostatic pressing. Samples Nos. 2, 3 and 6 were machined from the plated, hot isostatically pressed and extruded rods. Samples 2 and 3 yielded U.T.S. of 276 and 270 ksi and 48.4% reduction in area each, respectively. The slightly lower properties of sample No. 6 from the same billet can be attributed to the different heat treatment given this sample. Samples machined from the billet made of the plated and hot extruded rods possessed comparable mechanical properties as shown in Table V. It appears, from the results obtained thus far, that the intermediate step of hot isostatic pressing is unnecessary in consolidation of plated rods of maraging 300 alloy by hot extrusion.

Scanning electron micrographs of the fractured surfaces of three samples taken from each of the three billets are shown in Figure 17. Figure 17a shows the brittle fracture of the large grained, nonplated, and hot isostatically pressed rods. Figure 17b shows the ductile fracture of the plated and hot extruded sample. Figures 17c and d show the fractured surfaces of the plated, hot isostatically pressed, and hot extruded sample at two different magnifications. The junctions of the rods seem to be the weakest areas in each billet. It appears that a high temperature homogenization treatment should be included in the heat treatment cycle to facilitate diffusion of the plated nickel to the interior of each rod.

Presently research is continuing on the effect of high temperature

homogenization treatment on the redistribution of the plated nickel and elimination of microsegregation in the as-cast and consolidated rods.

CONCLUSIONS

1. Secondary dendrite arm spacing in Maraging 300 alloy varies proportionally to cooling rate to an exponent of $-1/4$.
2. Cooling rates during steam, argon, nitrogen or vacuum atomization of powders of Maraging 300 alloy are in the range of 10^2 to 10^3 °C/sec with resulting secondary dendrite arm spacings of 5 to 12 microns, in particles of 0.5 to 4.5 mm in diameter.
3. There is no observable difference in segregate spacing for a given size particle among the three gas atomization media of steam, argon, and nitrogen. On the other hand, vacuum atomized powders exhibit slightly larger segregate spacings in the absence of convective heat flow during atomization.
4. Lowering tap temperature leads to finer segregate spacings in coarse powders of Maraging 300 alloy.
5. Rapidly solidified, chill cast, 5/16" by 5/16" by 5" long rods of Maraging 300 and IN-100 alloys exhibit secondary dendrite arm spacings consistently less than 15 and 17 microns, respectively. These fine structures are comparable to structures of coarse powders obtained by atomization.
6. Hot extrusion of nickel plated, continuously cast, rapidly solidified rods of Maraging 300 alloy is an alternate method of producing sound large billets with fine segregate spacings.
7. A short high temperature homogenization treatment will be a method of diffusing the nickel plating to the interior of the rods and eliminating microsegregation in the billets.
8. Samples from a consolidated billet of rapidly solidified rods of Maraging 300 alloy possess mechanical properties as high as 276 ksi U.T.S., 268 ksi Y.S., 46% reduction in area, and 6.5% elongation.

REFERENCES

1. W. E. Brower, Jr., R. Strachan, M. C. Flemings, "Effect of Cooling Rate on Structure of Ferrous Alloys," Cast Metals Research Journal, V. 6, No. 4, 1970, pp. 176-180.
2. W. E. Brower, Jr., "Solidification-Structure-Fracture Relations in Inclusion Bearing Iron," Ph.D. Thesis, Department of Metallurgy and Materials Science, Massachusetts Institute of Technology 1969.
3. T. Z. Kattamis, M. C. Flemings, "Solidification of Highly Undercooled Castings," Trans. A.F.S., V. 75, 1967, pp. 191-198.
4. W. E. Ranz and N. R. Marshall, Jr., Chem. Eng. Prog., V. 48, 1952, pp. 141-146, 173-180.
5. S. Szekely and R. S. Fisher, "On the Solidification of Metal Spheres Due to Thermal Radiation at the Bounding Surface," Metallurgical Transactions, V. 1, 1970, pp. 1480-1482.

Table I
Samples of Atomized Coarse Powders
of Maraging 300 Alloy and Inconel 100

material	heat number	tap temperature	atomization	particle size
V4-300 IMT	30-137	3150°F	argon	-4/+5, -12/+14, -14/+30
" "	30-147	3090°F	steam	-4/+5, -8/+10, -16/+18, -25/+30
" "	30-148	3080°F	steam	-4/+5, -8/+10, -16/+18, -25/+30
" "	30-172	2845°F	argon	-4/+5, -8/+10, -16/+18, -25/+30
" "	30-173	2830°F	argon	-4/+5, -8/+10, -16/+18, -25/+30
" "	30-174	2815°F	nitrogen	-4/+5, -8/+10, -16/+18, -20/+25 -20/+25, -25/+30, -30/+35
" "	30-176	2790°F	steam	-4/+5, -8/+10, -16/+18, -20/+25 -25/+30, -30/+35
" "	Hom Mat.	—	vacuum	-20/+25, -25/+30, -30/+35
IN-100	Hom. Mat.	—	vacuum	-20/+25, -25/+30, -30/+35

Table II

Secondary Dendrite Arm Spacing Versus Diameter
of Atomized Powders of VM-300 and IN-100 Alloy

Atomization	Mesh Size	-4/+5	-8/+10	-16/+18	-20/+25	-25/+30	-30/+35
Medium	Droplet diameter in mm	4.0/4.7	1.9/2.3	1.0/1.2	.71/.83	.59/.71	.50/.59
Argon	IMT 30-137 VM-300	12.0 ± 1.0	8.5 ± 1.0	7.0 ± .3	—	—	—
	" 30-172 "	7.3 ± .4	6.8 ± .3	6.6 ± .2	—	5.1 ± .4	—
	" 30-173 "	8.5 ± .2	8.3 ± .2	7.0 ± .6	6.2 ± .6	5.4 ± .6	5.2 ± .4
Steam	" 30-147 "	11.7 ± 1.0	8.0 ± 1.0	7.2 ± .5	—	5.7 ± .6	—
	" 30-148 "	11.0 ± 1.0	7.9 ± 1.0	7.7 ± .4	—	6.9 ± .4	—
	" 30-176 "	7.8 ± .2	7.3 ± .4	6.6 ± .3	5.7 ± .6	5.3 ± .6	4.6 ± .5
Nitrogen	" 30-174 "	9.1 ± .3	8.5 ± .3	7.5 ± .7	6.5 ± .7	6.6 ± .6	5.4 ± .3
Vacuum	Hom. Met. "	—	—	—	7.0 ± .5	6.7 ± .5	6.3 ± .4
Vacuum	Hom. Met. IN-100	—	—	—	7.6 ± .7	5.9 ± .6	4.9 ± .3

Table III
Secondary Dendrite Arm Spacing (in microns)
of -16/+18 Mesh Size Droplet

Heat No.	30-148	30-174	30-137	30-173	30-176	30-172
Atomization Medium						
Argon	—	—	7.0μ	7.0μ	—	6.6μ
Nitrogen	—	7.5μ	—	—	—	—
Steam	7.7μ	—	—	—	6.6μ	—

Table IV
Bonding processes and heat treatments
for the different samples of VM-300

Sample number	Material	Plating	H.I.P.	Extrusion	Annealing	Aging	Cooling
1	VM-300	none	30,000 psi 2250°F 1hr	none	1500°F 1hr	900°F 3hr	air
2	"	.0002"Ni	15,000 psi 2150°F 1 1/2hr	135 tons 70-80"/min	"	850°F 3hr	"
3	"	"	" "	" "	"	"	"
4	"	"	none none	" "	"	"	"
5	"	"	none none	" "	"	"	"
6	"	"	15,000 psi 2150°F 1 1/2hr	" "	"	810°F 3hr	"
7	"	"	none none	" "	"	"	"
8	"	"	none none	" "	"	900°F 3 1/2hr	"

Table V
Mechanical properties of the different
samples of VM-300

Sample number	U.T.S. ksi	.2% offset yield strength ksi	reduction in area %	elongation %	hardness R _c	grain size
1	275.0	262.0	none	none	—	1mm
2	276.1	271.1	48.4	6.40	—	—
3	270.8	264.9	48.4	6.00	51.1	—
4	264.8	259.8	44.5	4.85	—	10μ
5	278.0	274.1	43.7	4.10	51.5	"
6	251.0	245.0	44.5	6.00	46.1	"
7	243.5	234.0	44.0	6.50	—	"
8	276.0	268.0	46.0	6.50	51.6	"

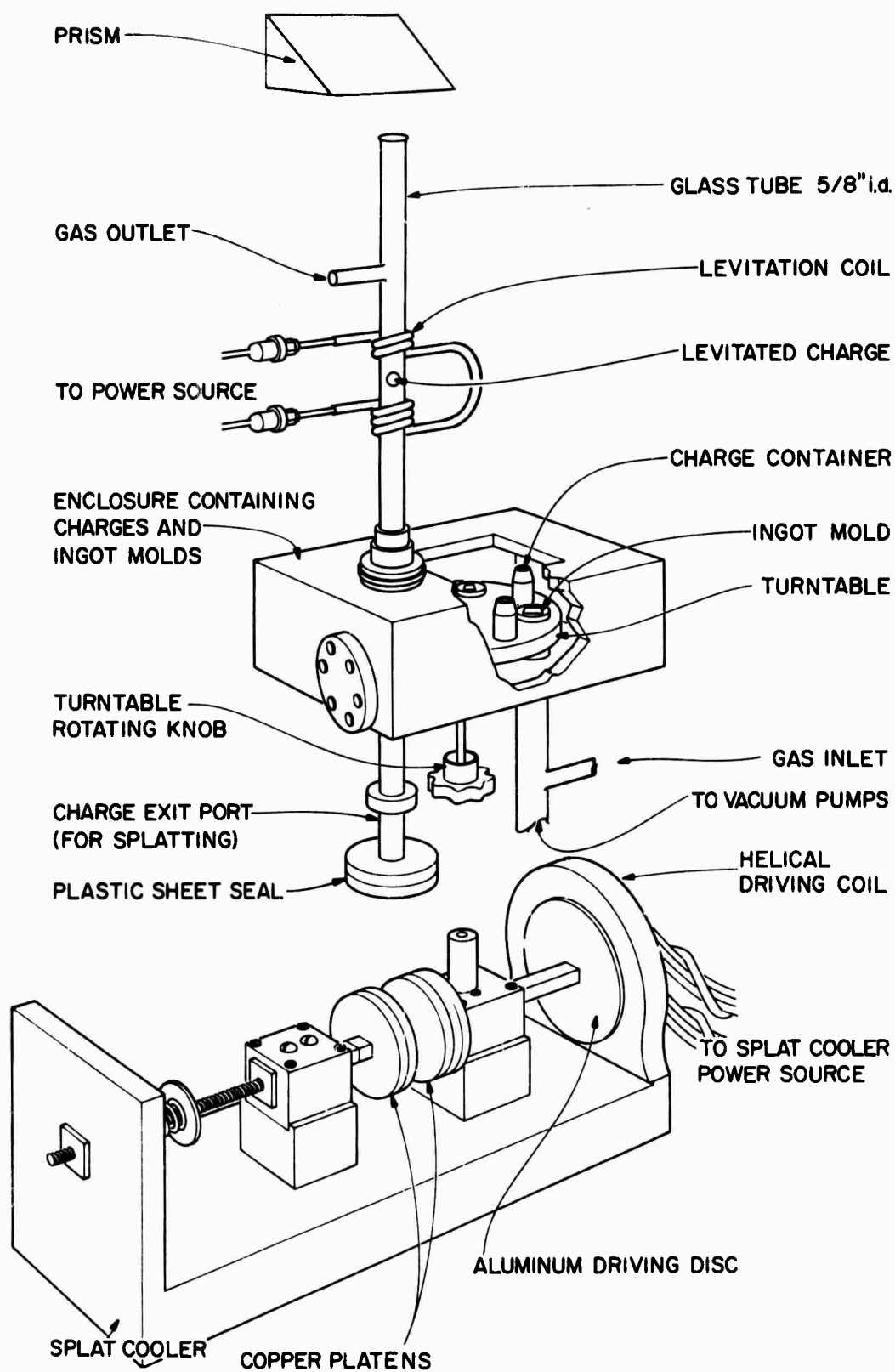


Figure 1. Sketch of levitation melting and casting apparatus.

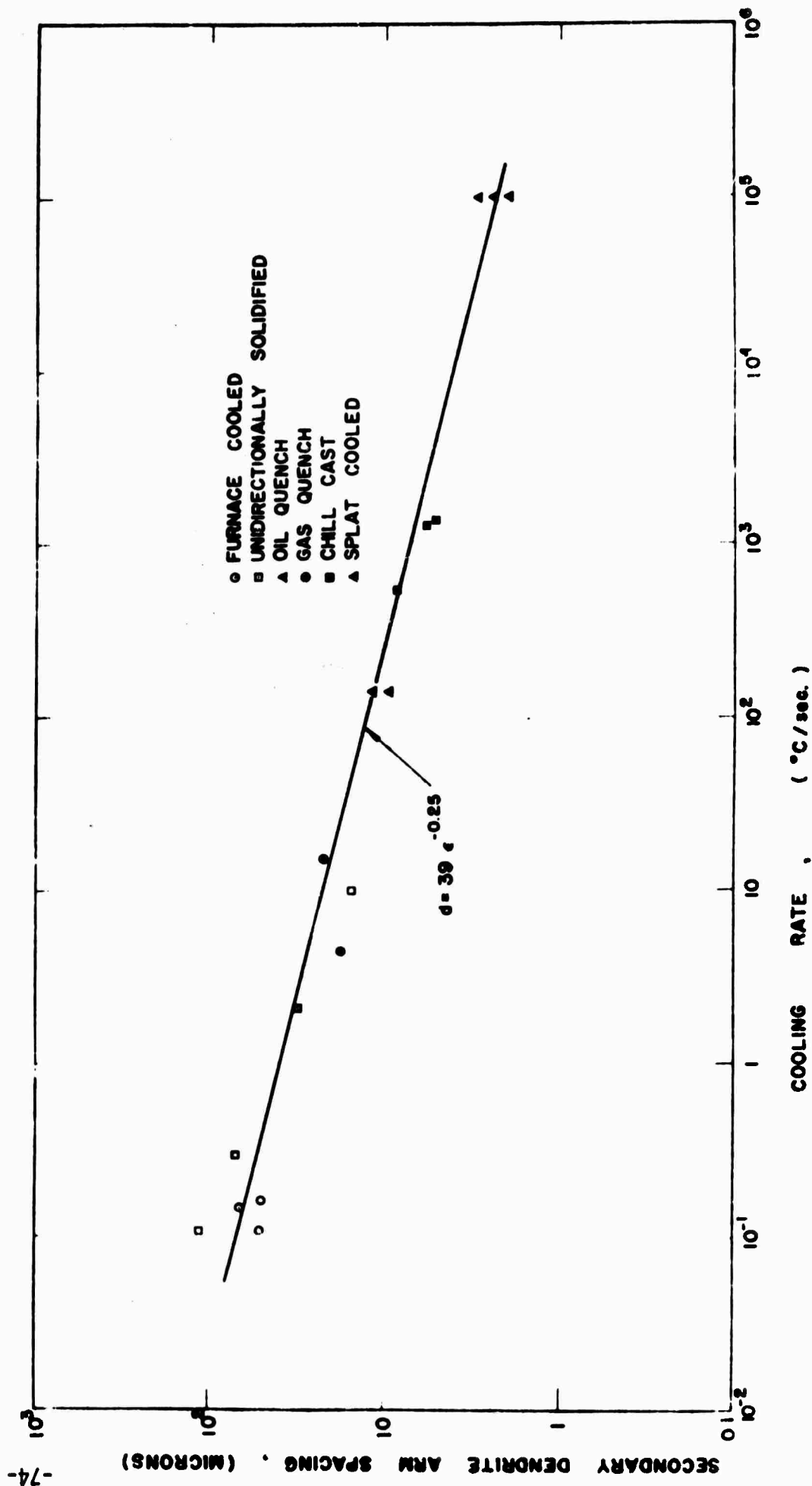


Figure 2. Secondary dendrite arm spacing versus cooling rate, maraging 300 alloy.

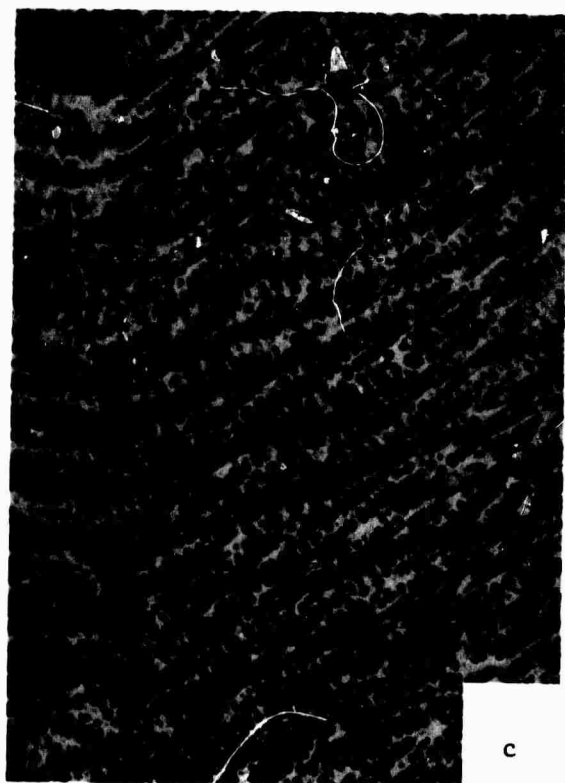


Figure 3. Variation of microstructure with cooling rate for maraging 300 alloy. (a) Gas quench, (b) liquid quench, (c) chill cast, (d) splat-cooled. Magnification 200X.

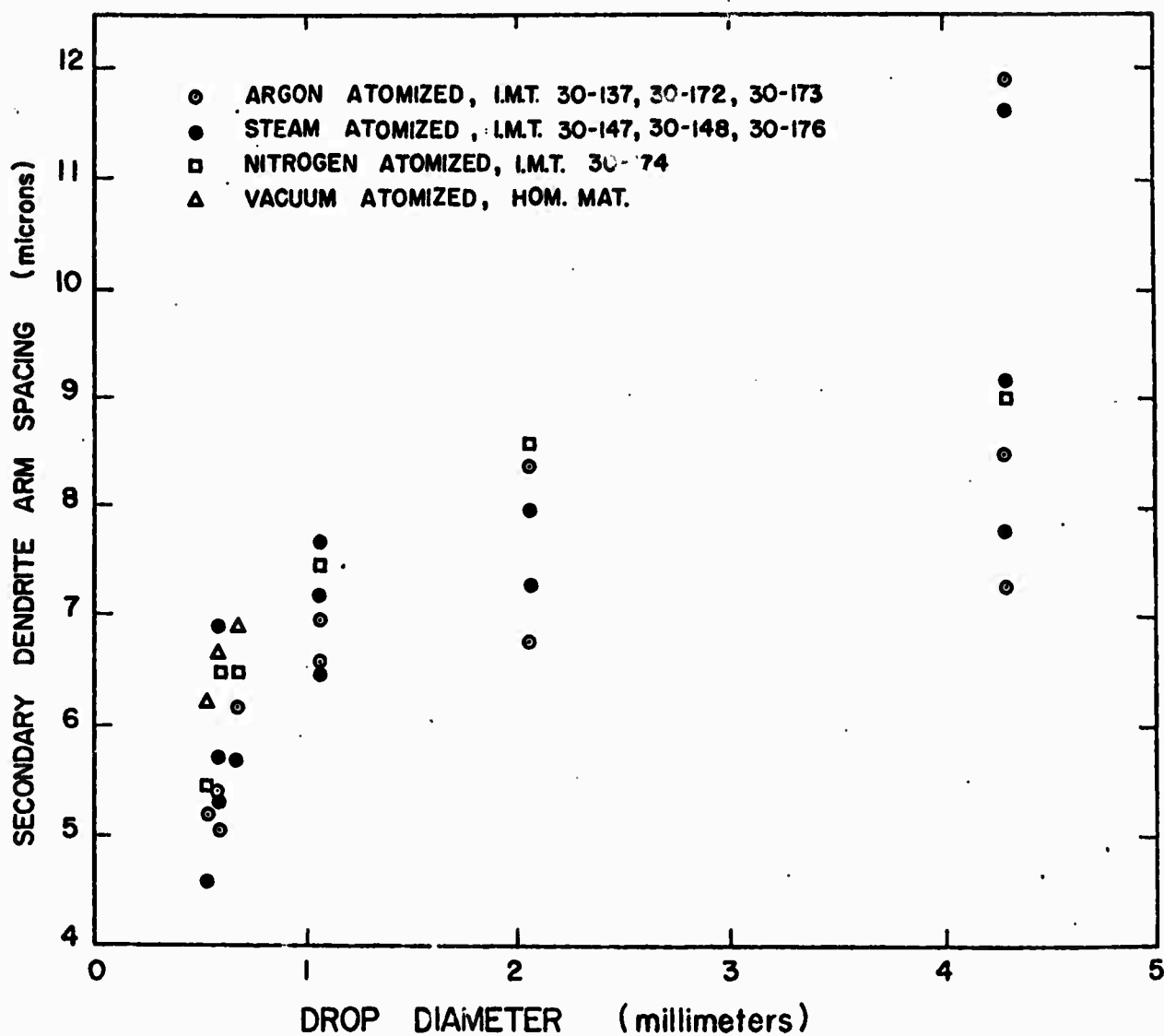


Figure 4. Secondary dendrite arm spacing versus diameter of coarse powders of atomized maraging 300 alloy.

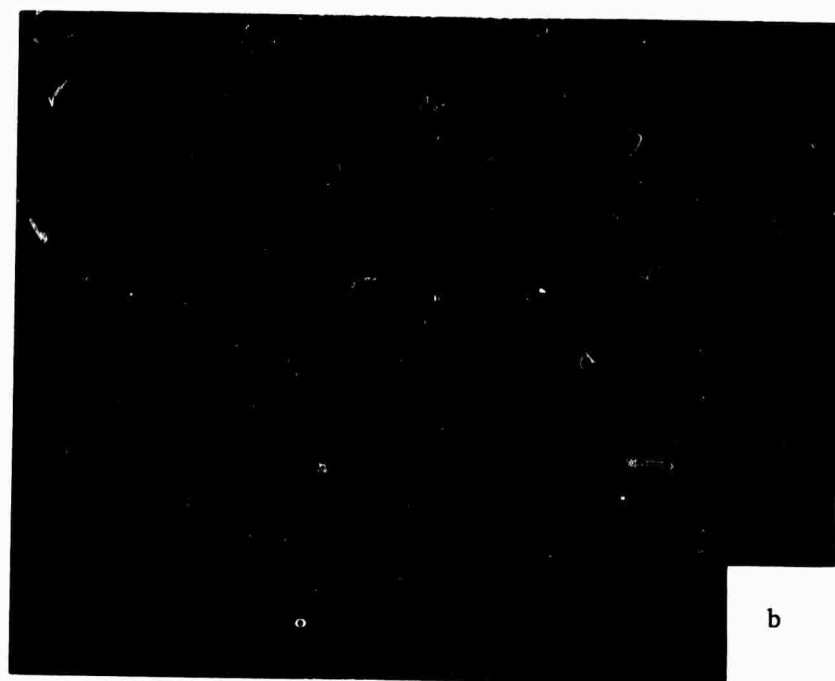
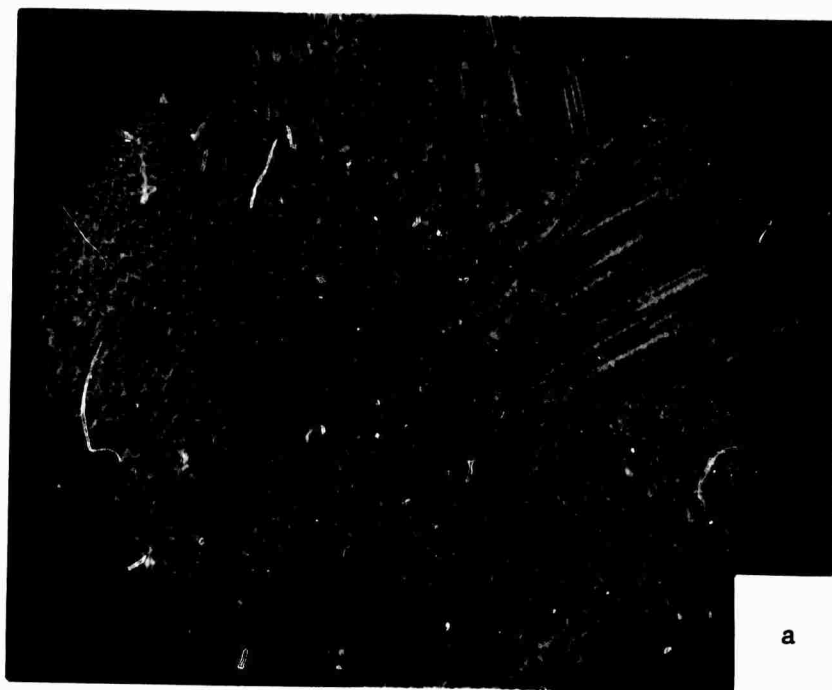


Figure 5. Photomicrographs of steam atomized powders of maraging 300 alloy. (a) mesh size -16/+18, Mag. 100X, (b) mesh size -30/+35, Mag. 200X.

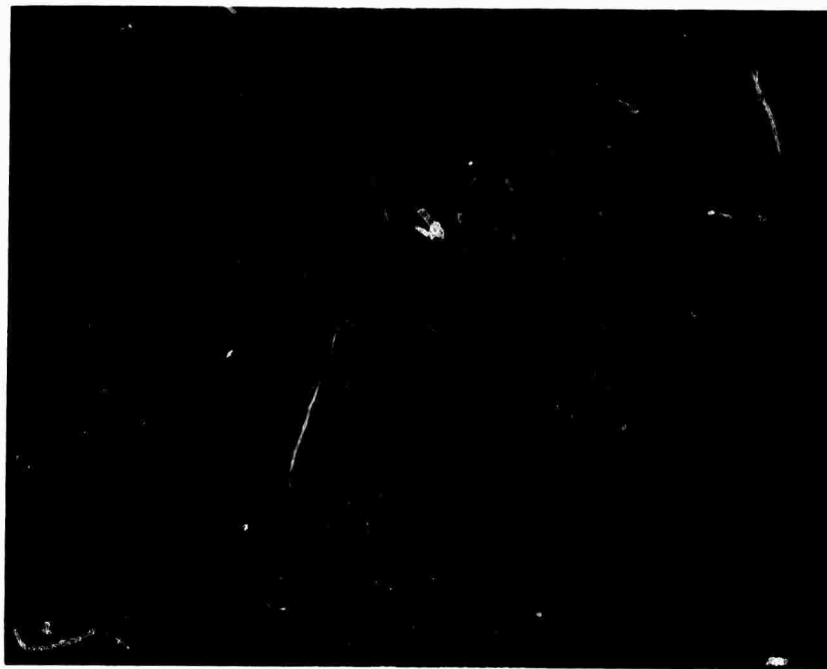


Figure 6. Photomicrograph of steam atomized powder of maraging 300 alloy, mesh size -30/+35. Mag. 200X.

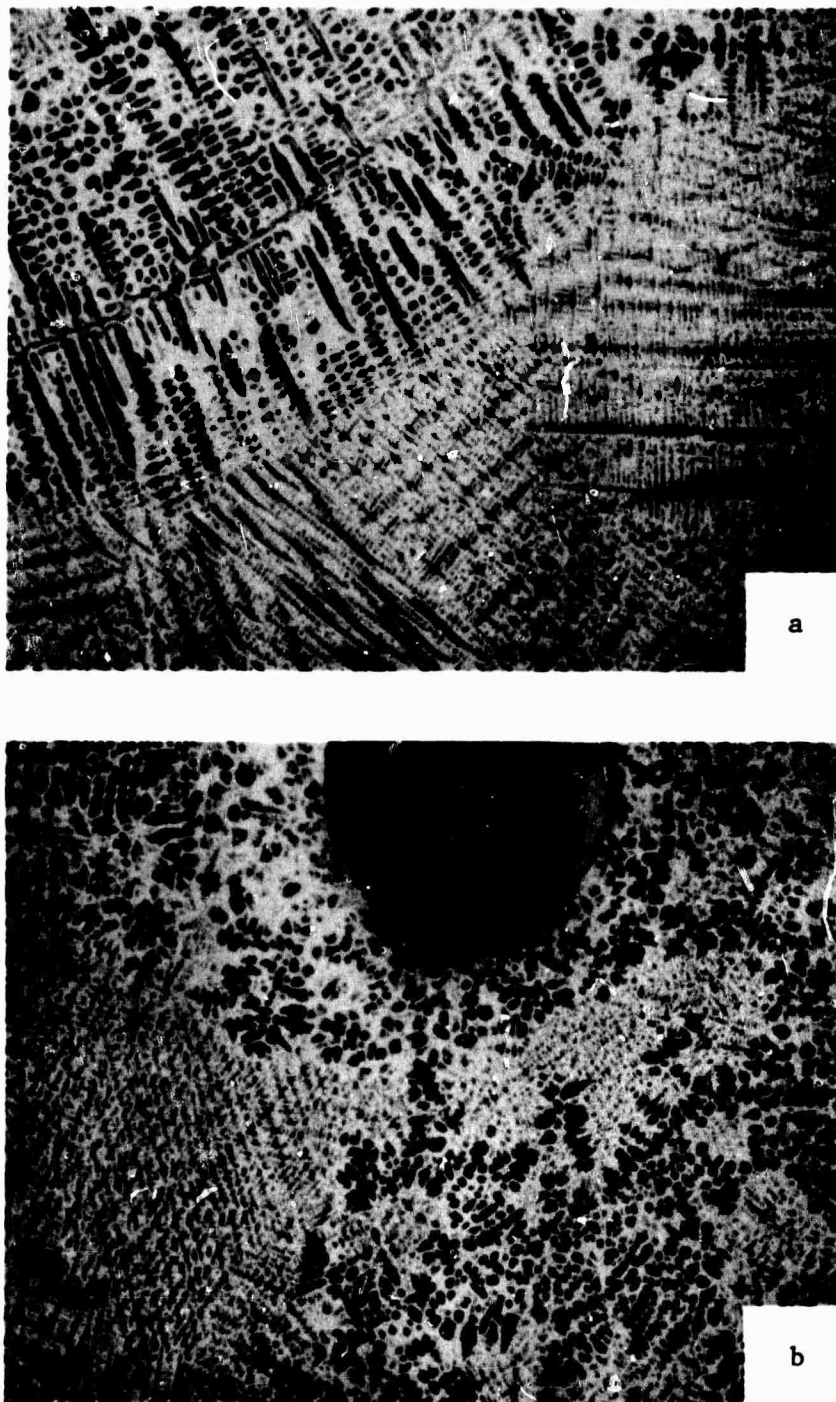


Figure 7. Duplex dendritic structure of steam atomized coarse powders of maraging 300 alloy. (a) IMT Heat# 30-148, mesh size -4/+5, (b) IMT# 30-148, mesh size -8/+10. Mag. 75X.



Figure 8. Photomicrograph of a vacuum atomized powder of maraging 300 alloy, mesh size -30/+35, Mag. 200X.

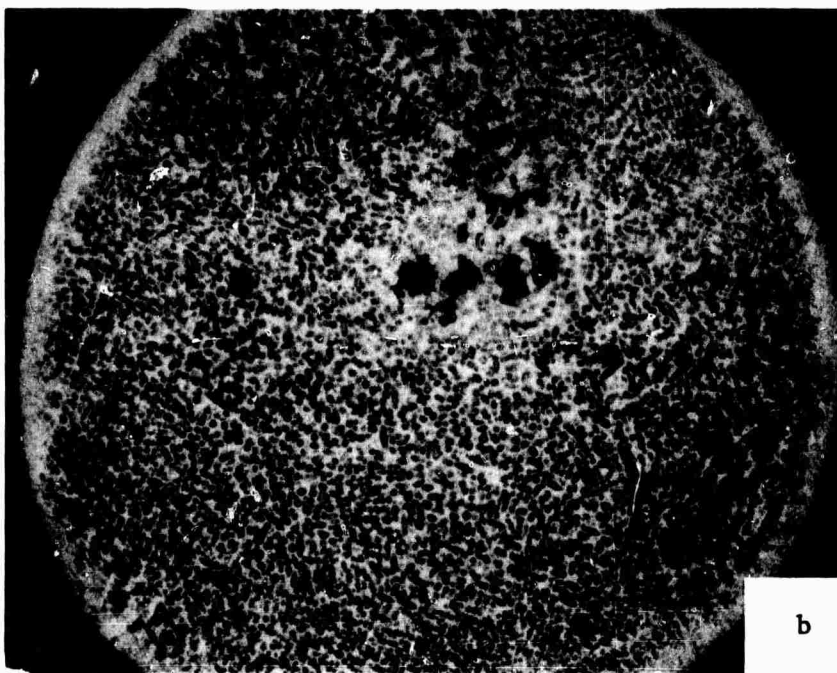
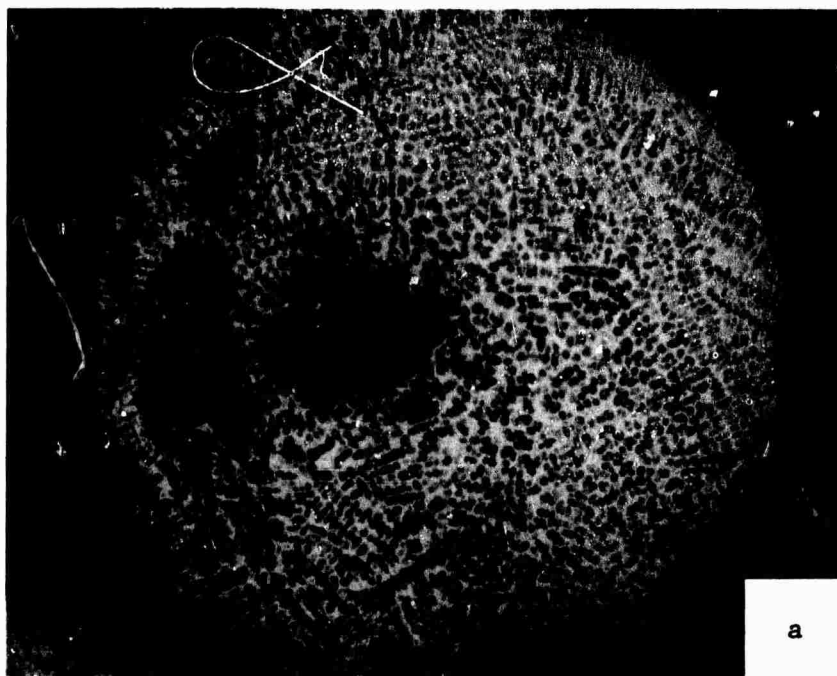
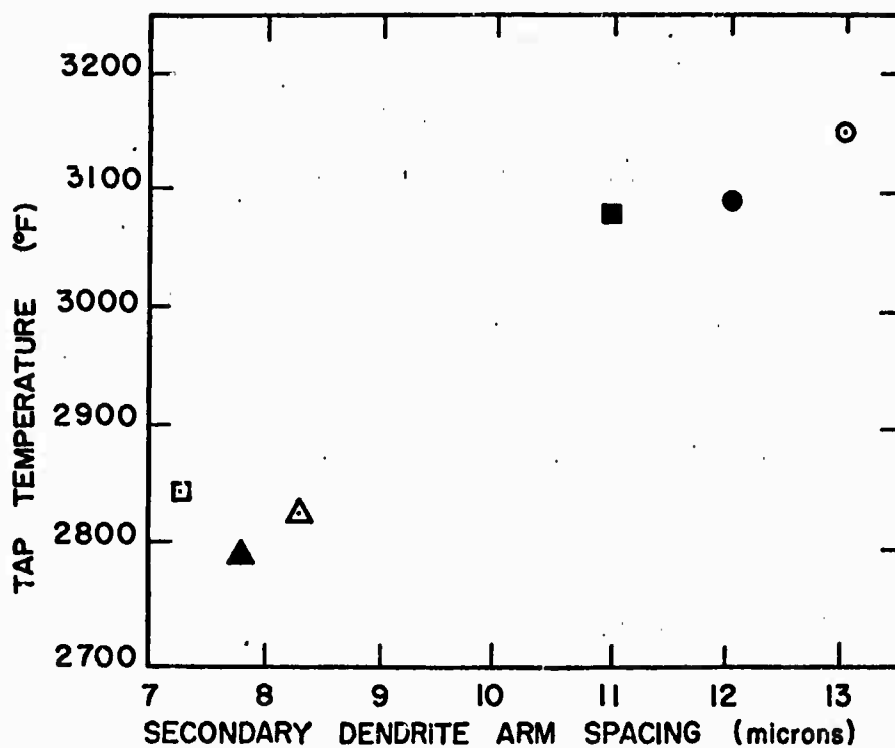


Figure 9. Photomicrographs of atomized coarse powders of maraging 300 alloy, mesh size -16/+18. (a) IMT Heat#30-148 steam atomized, (b) IMT Heat#30-172, argon atomized. Mag. 100X.



Figure 10. Photomicrograph of vacuum atomized powder of IN-100 alloy, mesh size -25/+30. Mag. 200X.



- Maraging 300 alloy, argon atomized, Heat No. 30-137
- Maraging 300 alloy, argon atomized, Heat No. 30-172
- △ Maraging 300 alloy, argon atomized, Heat No. 30-173
- Maraging 300 alloy, steam atomized, Heat No. 30-147
- Maraging 300 alloy, steam atomized, Heat No. 30-148
- ▲ Maraging 300 alloy, steam atomized, Heat No. 30-176

Figure 11. Secondary D.A.S. versus top temperature of maraging 300 alloy powders, mesh size -4/+5.

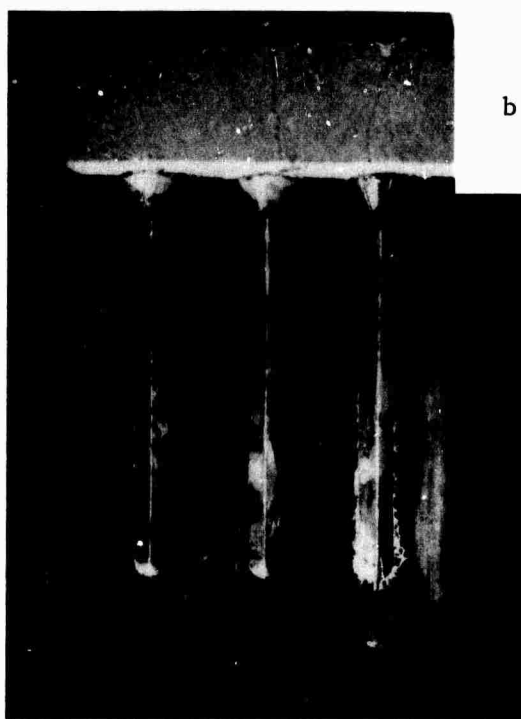
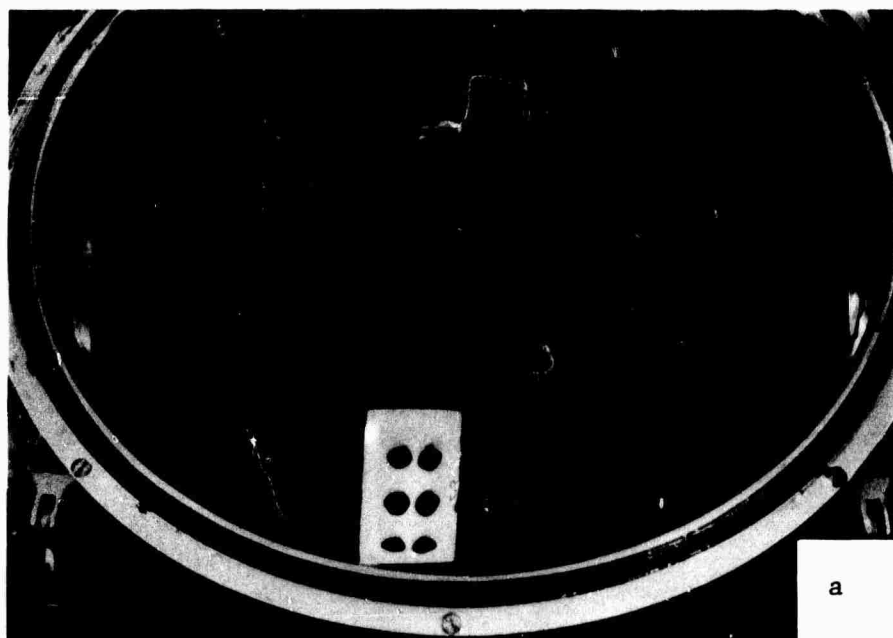


Figure 12. Photographs of (a) melting furnace and casting arrangement and (b) middle section of copper chill mold and cast rods of maraging 300 alloy; top section is part of the rowing basin made from CO₂ sand.

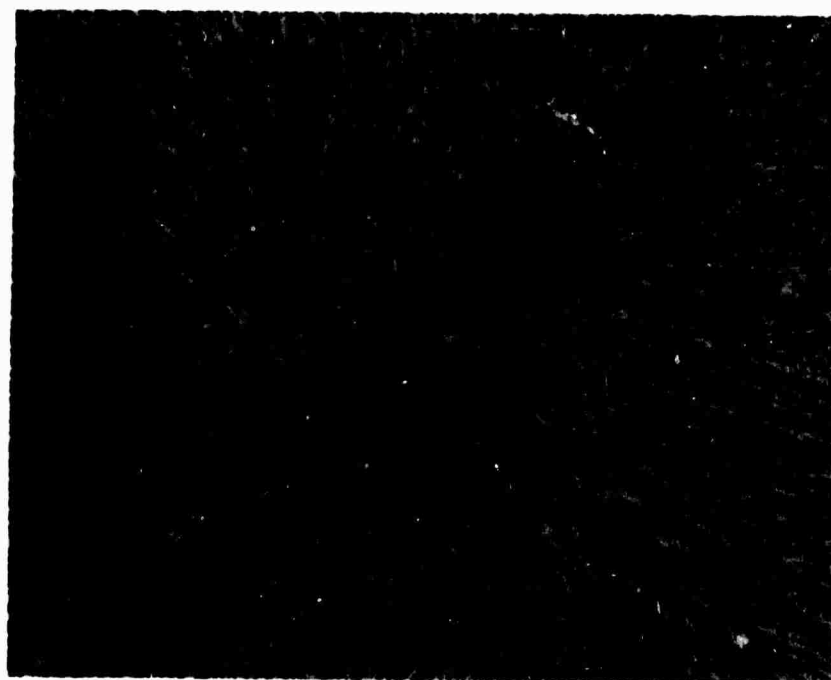


Figure 13. Photomicrograph showing the cross-sectional dendritic structure of rapidly solidified maraging 300 alloy rod. Magnification 50X.

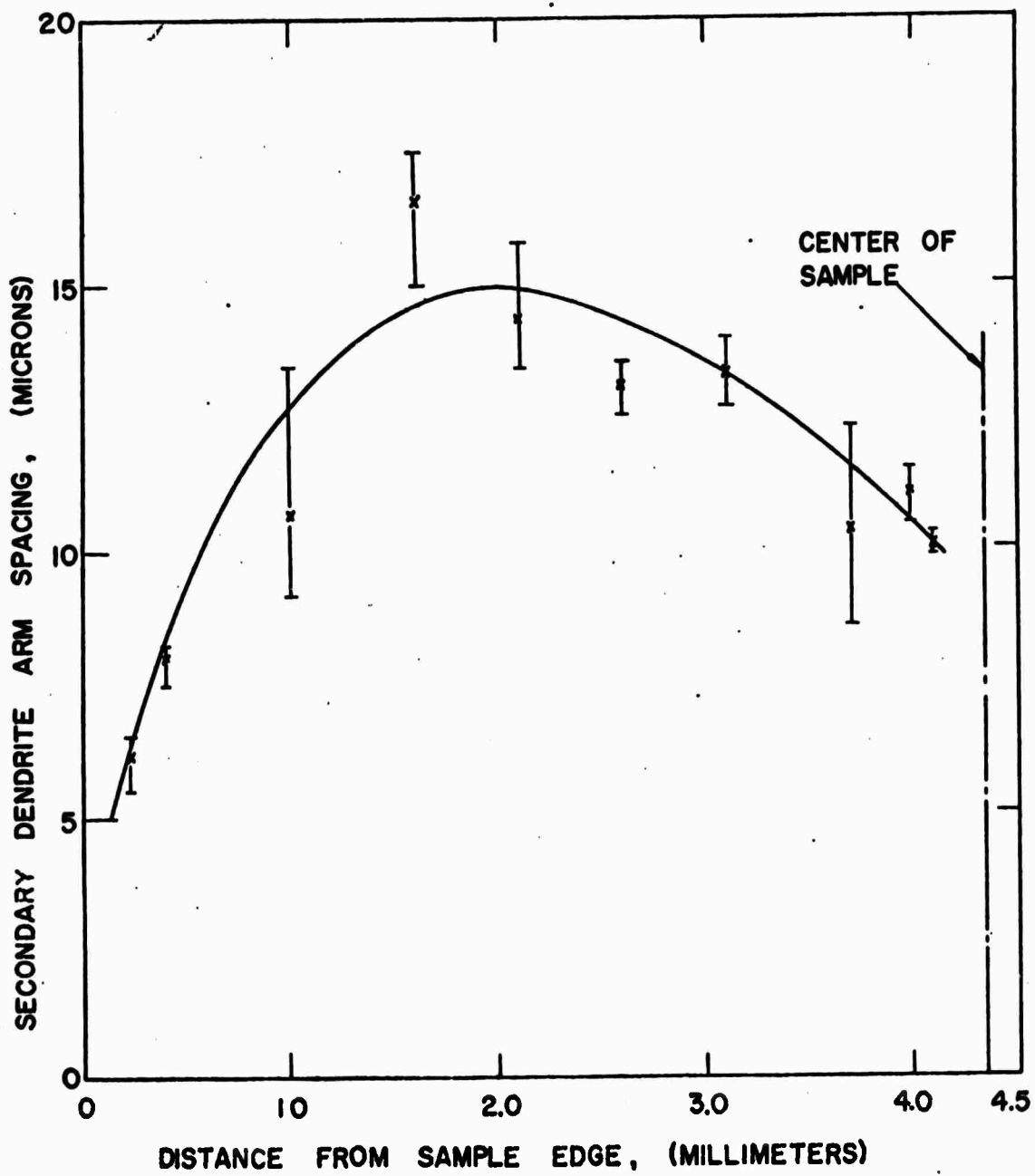


Figure 14. Secondary dendrite arm spacing versus distance from edge of 5/16" x 5/16" square rod of rapidly solidified maraging 300 alloy.

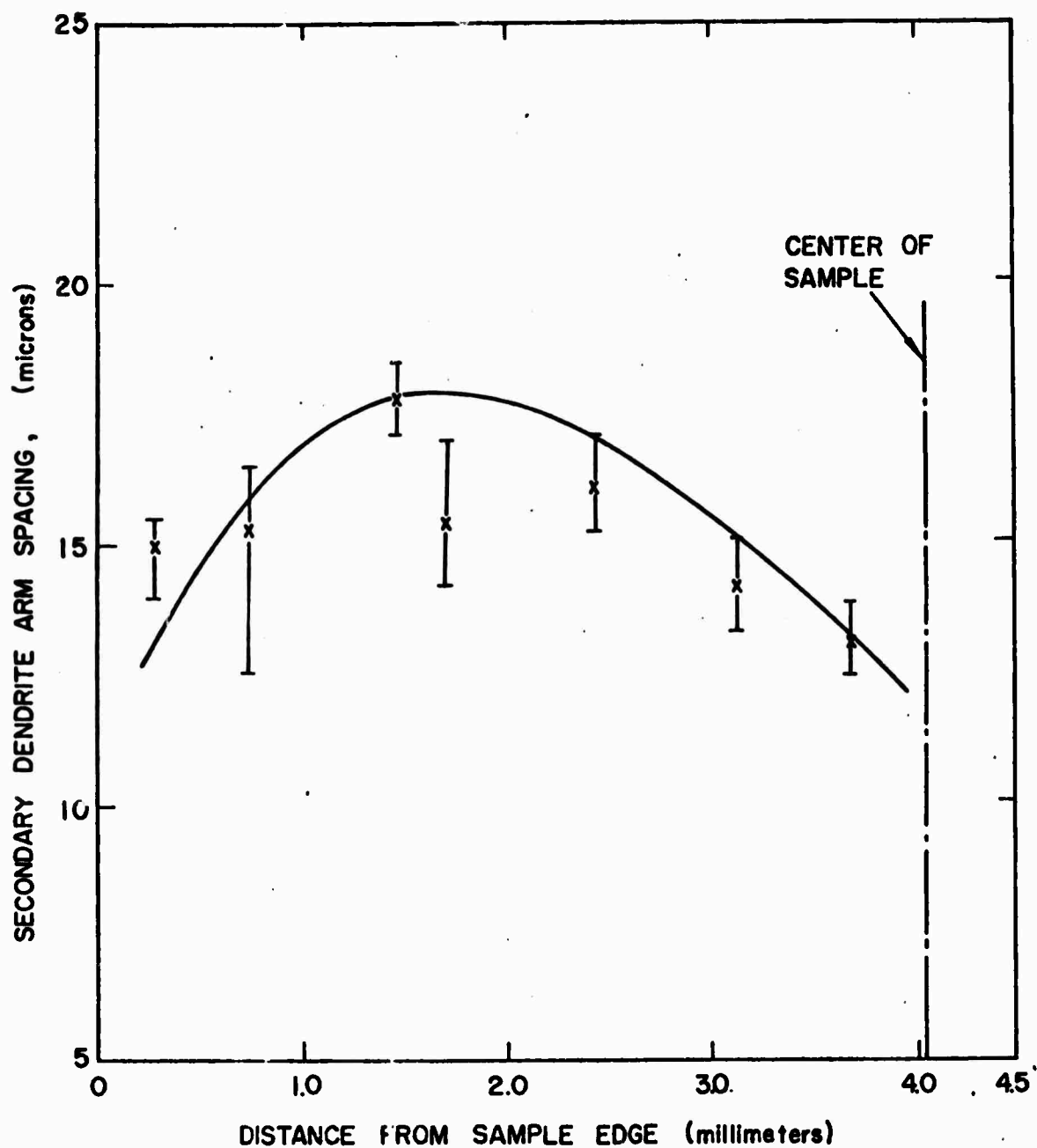
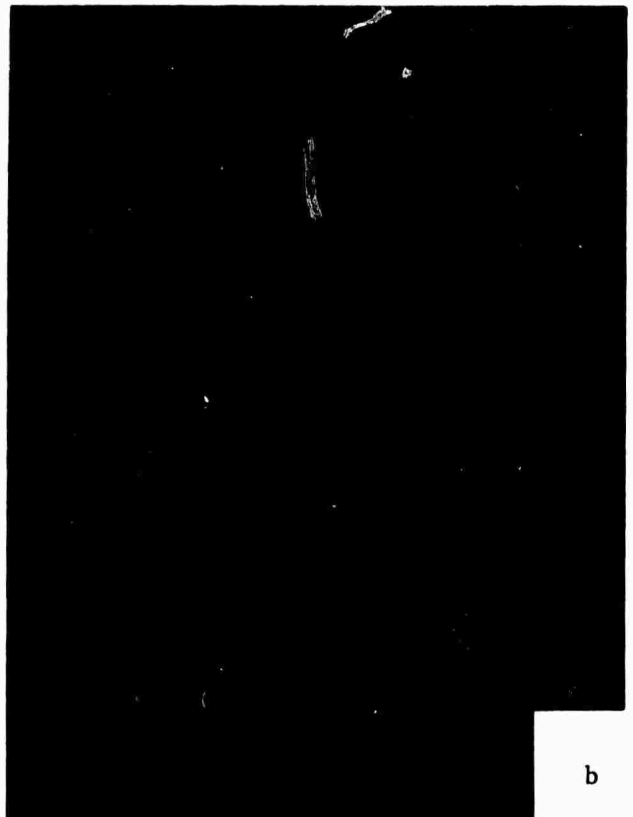


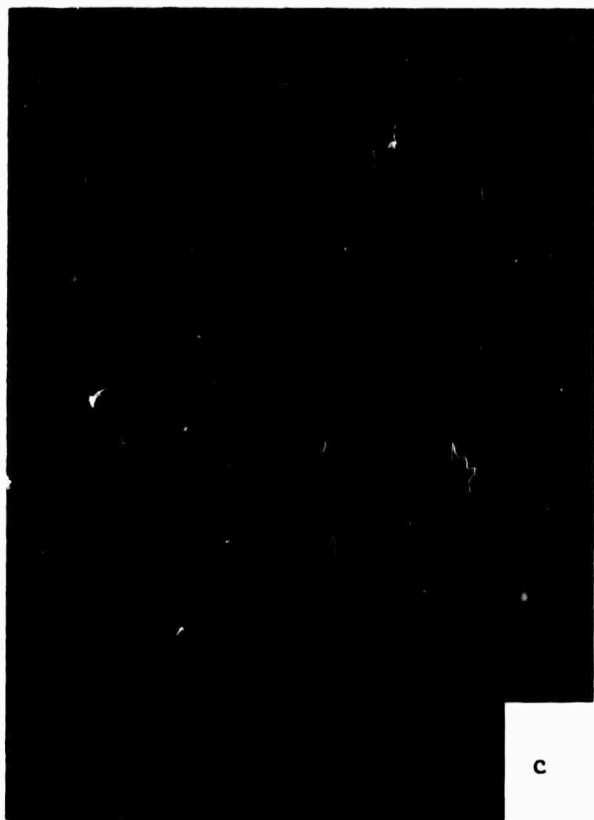
Figure 15. Secondary dendrite arm spacing versus distance from edge of 5/16" x 5/16" square rod of rapidly solidified IN-100 alloy.



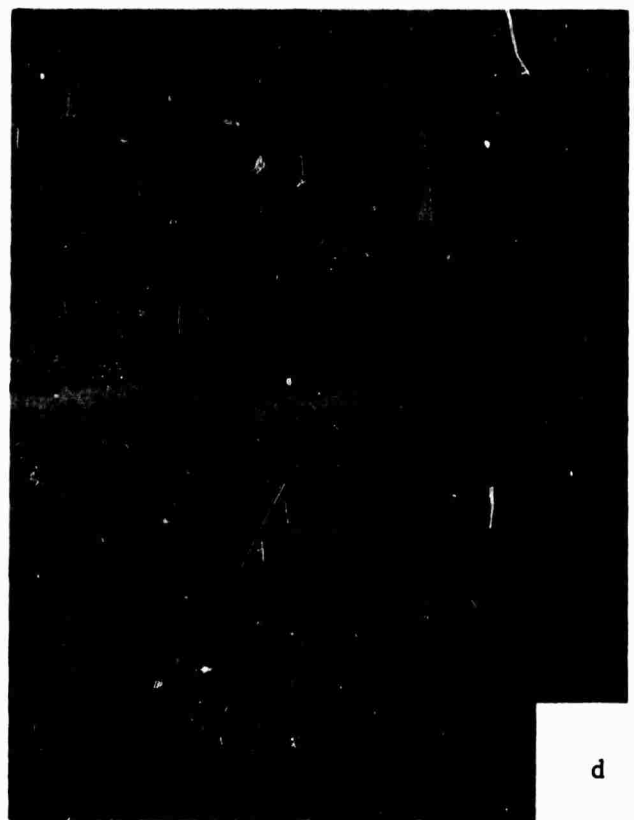
a



b



c



d

Figure 16. Photomicrographs showing the cross-section of consolidated rods of maraging 300 alloy. (a) non-plated rods, hot isostatically pressed, mag. 50X, (b) plated rods, hot isostatically pressed, mag. 100X, (c) plated rods, hot extruded, mag. 100X, (d) plated rods, hot isostatically pressed and hot extruded, mag. 100X.

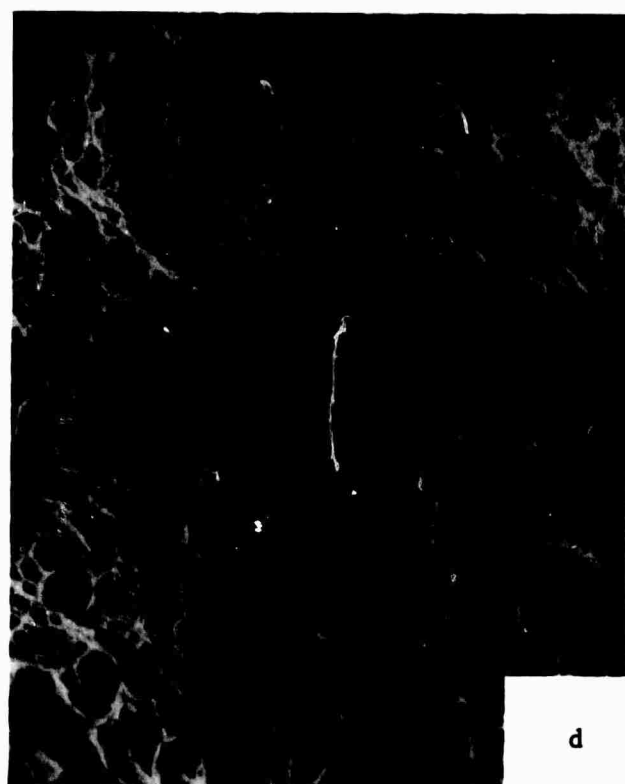
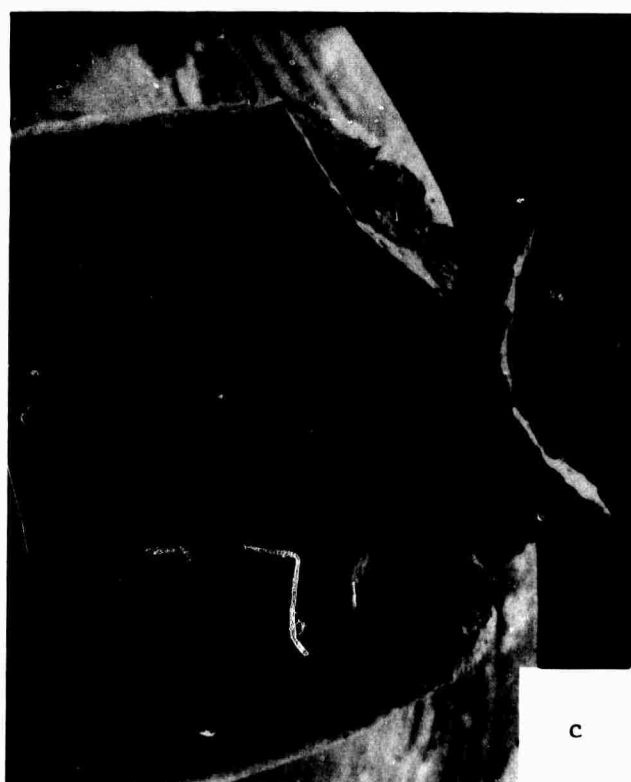
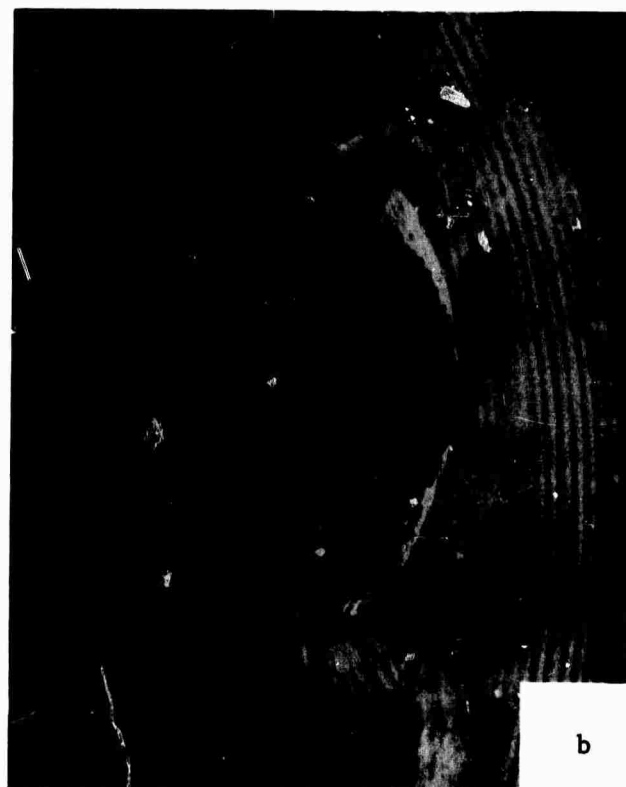


Figure 17. Scanning electron micrographs showing the fracture surfaces of consolidated rods of maraging 300 alloy. (a) non-plated rods, hot isostatically pressed, mag. 51X, (b) plated rods, hot extruded, mag. 26X, (c) plated rods, hot isostatically pressed and hot extruded, mag. 20X, (d) same as (c) mag. 1300X.

- TASK III -

Thermomechanical Treatments

**N.J. Grant
R.M.N. Pelloux
L.F.P. van Swam
L. Moskowitz
R.K. Robinson**

METALLOGRAPHY AND MECHANICAL PROPERTIES
OF
300 GRADE MARAGING STEELS

INTRODUCTION

To provide a baseline for the research in the mechanical properties of 300 grade maraging steel, extensive testing of commercial material took place. Stock in the form of 4" wide by 1 1/4" thick bar was obtained from Vasco. The composition of this material which was received in the annealed condition (one hour at 1500°F followed by cooling in air to room temperature) is given in Table I.

Most maraging steels produced by the classical ingot-hot work route show some degree of banding. Micrographs showing a moderate degree of banding in a commercial product were shown in our first half-yearly progress report.* Since segregation of alloy constituents in the ingot causes banding, it can be expected that materials produced by powder metallurgical methods are free of this kind of defect. Several products using atomized powders or small chill cast bars as a starting material have now been made and tested. A summary is given below:

- a. - Materials produced by Task I (I.M.T.). These include steam (I.M.T.) vacuum plus hydrogen atomized (H.M.) and argon spinning electrode (N.M.) powders. Final products utilized were:
 - 1. Steam atomized MAR 300. Extruded bar.
 - 2. Homogeneous Metals powder (H.M.). Hot isostatic pressed billet and extruded bar.
 - 3. Nuclear Metals powder (N.M.). Three final products: hot isostatic pressed billet, hot isostatic pressed and extruded bar, and loose powder extruded bar.
- b. - Materials produced by Task II. The starting material is 5/16"

* Semi-Annual Technical Report No. 1 - Task III

square chill cast bar and testing was done on:

- 1. As-cast material.
- 2. As-cast plus 30% cold swaged material.
- 3. Hot isostatic pressed bars.
- 4. Extruded bars.

Metallography and tensile testing was performed on all materials. Other testing included heat treatment response, Charpy testing, and fatigue testing. A start was made on plain strain tensile and fracture toughness testing of commercial stock.

HEAT TREATMENT

All commercial material is received in the solutionized condition. The usual solutionizing treatment consists of 1 hour at 1500° F followed by air-cooling. The material is then fully martensitic. In cases of very severe banding, stringers of retained austenite may be found; however, this was not the case in any of our materials.

The effect of aging temperature and time upon the hardness of maraging steel 300 was given in our first half yearly report.

The following heat treatments have been adopted for all materials tested:

- a. - Solutionizing treatment: 1 hour at 1500° F in either air or vacuum.
- b. - Aging treatment: 3 hours at 900° F in air.

Both heat treatments are followed by cooling in still air.

TENSILE PROPERTIES

The specimen size used in all tensile tests is 1" gauge length and 0.160" gauge diameter. These dimensions were chosen to preserve on material (small diameter) and to facilitate the use of a 1" long extensometer which was used in all tensile testing. It should be noted that the ratio of gauge length over diameter is greater than the ASTM standard 4:1. Total elongation values, if reported, will thus be low compared to values reported elsewhere.

Reduction in area, U.T.S., 0.2% offset, Youngs modulus E and the work-hardening exponent are determined on solutionized and aged specimens where possible. The availability of material limited the testing to aged specimens only in some cases. All the data obtained so far are given in Table II, which will facilitate comparison between the different materials.

The following specific comments can be made:

- a. - Commercial material-

- The obtained values compare well with values found in the literature. The very low workhardening exponent is especially noticeable. The fracture surface of the specimens was studied in the SEM. Typical ductile fracture and large voids around broken up inclusions are found. See Fig. 1.

b. - Materials produced by Task I.

- The steam atomized and extruded MAR 300 steel shows a large number of inclusions. Analysis of these inclusions with the ARL microprobe shows high levels of Al and Ti and smaller amounts of Ni, Co, Fe and Cr. It was concluded that the inclusions are oxide particles formed during atomization. All specimens show reasonable strength, considering the low level of Ti available for precipitation. (See Task I report for chemical analysis.) The reduction in area is, however, sharply reduced.

- With the Homogeneous Metals powder, the first batch of powder was contaminated with superalloy particles, as shown on the SEM with the microanalyser. Although both a hot isostatic pressed billet and an extrusion were produced by I.M.T., no tensile tests were performed on these contaminated products.

- Three final products were obtained from atomized powder made by Nuclear Metals. Nuclear Metals uses the spinning electrode method to atomize metals and the operation is carried out in an argon atmosphere. The process produces a clean and uniform product.

The hot isostatic pressed material obtained was not fully dense, as can be seen in Fig. 2. It showed, accordingly, low strength and little ductility.

The differences in tensile properties between hot isostatic pressed plus extruded and direct powder extruded material are minimal. The strength and the ductility of these two materials compares favorably with commercial maraging steel. This might be due to the absence of inclusion stringers as found in commercial products. It is also possible that more Ti is available for strengthening since the number of Ti_2S inclusions is lower in the atomized material. The particle boundaries in both materials can be made visible by etching in 10% HNO_3 propanol mixture. See Fig. 3 for a longitudinal section of the powder extrusion. The powder extrusion showed splitting of the tensile bar in the direction of pulling. This indicates a somewhat poor bonding between the particles. The bonding between particles in the hot isostatic pressed

and extruded material is most probably better because the material is at a high temperature (2150°F) for a longer time (3 hours) and diffusion can take place readily.

c. - Material produced by chill casting (Task II)

- A number of specimens were made from as-chillcast maraging steel. The as-cast material shows little strength and no ductility. This is undoubtedly due to the fact that the castings are full of shrinkage cavities. 30% Cold swaging helped very little in this regard. The fracture appearance of one of the bars is shown in Fig. 4.

Hot isostatic pressing of the bars produces a material with a large grain size (Fig. 5). The material shows little ductility and the original bar surfaces delaminate in tensile testing. Apparently, very little bonding between the bars took place during pressing. Separation of grain boundaries was observed on the SEM (see Fig. 6), but the surface is typical of ductile fracture (see Fig. 7). The center of the bar showed inclusions high in Al and containing some Ti; these inclusions might be aluminum-oxide, but it is difficult to determine this with the X-ray analyser on the SEM.

FATIGUE TESTING

Fatigue testing was done on a Baldwin SF-1 machine. All testing is in tension-compression with a mean load of zero. A constant load is maintained throughout the test and the specimens fail in general shortly after a crack is initiated.

The specimens used in our investigation have a 0.3" gauge length and are 0.15" in diameter.

The results of 14 tests of commercial material in the aged condition and of 16 tests of Nuclear Metals H.I.P. plus extruded material are given in Table III and plotted on a S-N curve in Fig. 8. The commercial material seems to perform slightly better than the powder product.

CHARPY IMPACT TESTING

Three standard Charpy V-notch specimens taken in 4 directions of the commercial barstock were tested in the aged condition. Eight of the specimens were tested at room temperature and four at liquid nitrogen temperature. The testing results are given in Table IV. The impact energy at room temperature is from 14 to 19 ft. lbs., depending on the direction of sample and notch, and from 3 to 6 ft. lbs. at liquid nitrogen temperature.

The fracture surface of these specimens as seen under the SEM is fully ductile at both temperatures. Fig. 9 shows a photograph of the notch root and part of the fracture surface of one of the specimens tested at liquid nitrogen temperature.

PLANE STRAIN TENSILE TESTING

Plane strain tensile testing of aged Vascomax 300 was undertaken to evaluate the plane strain tensile ductility of this material. The specimens used in our preliminary tests were 6" long, 1" wide and 0.25" thick and have a reduced section in the center parallel to the specimen width. This section is 0.25" wide and 0.05" thick. It is assumed that this area is in a state of plane strain and plane stress when the specimen is loaded in tension. Strains parallel to the tension axis and parallel to the specimen width have to be measured. In a first attempt to do this, a square grid with 100 lines per inch was photographically brought onto the reduced section. Measuring the distance between lines after fracture makes it possible to evaluate the plastic strain in both directions. The plastic deformation before fracture in maraging steel is too small, however, to be recorded in this way, and in our second attempt, metal foil gauges were mounted on the reduced section. One gauge was mounted parallel and the other transverse to the direction of pulling. The gauges, however, have a tendency to pop off just before fracture occurs. It was found that some plastic strain occurs in the direction of the specimen width and it is therefore necessary to redesign the specimen somewhat. It seems, furthermore, necessary to employ extensometers to measure the strains up to the point of fracture.

FRACTURE TOUGHNESS TESTING

The recommendations put down in ASTM E 399-70 were followed as closely as possible in the fracture toughness testing of aged Vascomax 300. Three point bending of 0.25" thick and 1" wide specimens was carried out on an MTS machine after starting of a fatigue crack. The crack propagation was measured with a clip-on extensometer as described in the ASTM standard. The recordings of load versus crack propagation in our tests failed to meet the criteria put down in the recommendations, and it was noted that all the specimens had a very extensive shearlip. Compact tensile specimens, 0.5" thick rather than 0.25" are now being made and will be tested soon.

- TABLE I -

Analysis of Commercial Maraging Steel 300
(Vascomax 300) used in this investigation

	<u>Weight percent</u>
Nickel	18.26
Cobalt	8.82
Molybdenum	4.81
Titanium	.66
Aluminium	.09
Carbon	.014
Silicon	.02
Manganese	.05
Sulfur	.004
Phosphorus	.005
Calcium	.05
Zirconium	.01
Boron	.004

- TABLE II -

Summary of Tensile Properties

Solutionized					Aged 3 hrs 900°F									
	Commercial Material	I.M.T. Steam at. heat # 3148	Nuclear Metals H.I.P. + extrus.	Nuclear Metals Extrus. only	Nuclear Metals H.I.P. only		Commercial Material	I.M.T. Steam at. heat #3148	Nuclear Metals H.I.P. + extrus.	Nuclear Metals Extrus. only	Chill Cast 95 cast	Chill Cast 30% cold swag.	Chill Cast H.I.P. center	Chill Cast H.I.P. intersection
U.T.S. k.s.i.	145.8 145.0	163.0	151.0	153.0	147.0		274.0 280.0	247.0	291.0	290.0	175.0 92.5	247.5 170.0	267.5	275.0
0.2% Offset k.s.i.	138.8 120.0	100.0	125.0	125.0	123.0		269.0 272.5	235.0	285.0	285.0	-	-	260.0	262.0
Reduction in area percent	76.0 72.1	46.2	65.6	68.6	22.3		48.6 53.6	12.5	47.3	48.4	Ni1 Ni1	3 Ni1	Ni1	Ni1
Workhardening exponent n	0.02 0.02	0.03					0.02 0.02	0.01			-	-	-	-

- TABLE III -

Results of Tension-Compression Fatigue Testing
of Cylindrical Specimens of Maraging Steel 300
in the Aged Condition

<u>Load ksi</u>	<u>Life cycles x 10³</u>	
	<u>Commercial</u>	<u>N.M. Powder</u>
200	15	
150	20	8
120	41	21
100	80	89;885
90	72;274;218;2273	87;1907;109;343
80	498;116;423;937	416;334;5060;98
70	1053;5330*	267;662;5860*;514

* specimen did not break.

- TABLE IV -

Results of Charpy Impact Testing
in Ft. Lbs. of Vascomax 300
in the Aged Condition

<u>Specimen</u>	<u>Room temperature</u>		<u>Liquid Nitrogen</u>
W T	17	15	3
W R	14	15	4
R T	19	19	6
R W	19	18	4

Key to specimen designation:

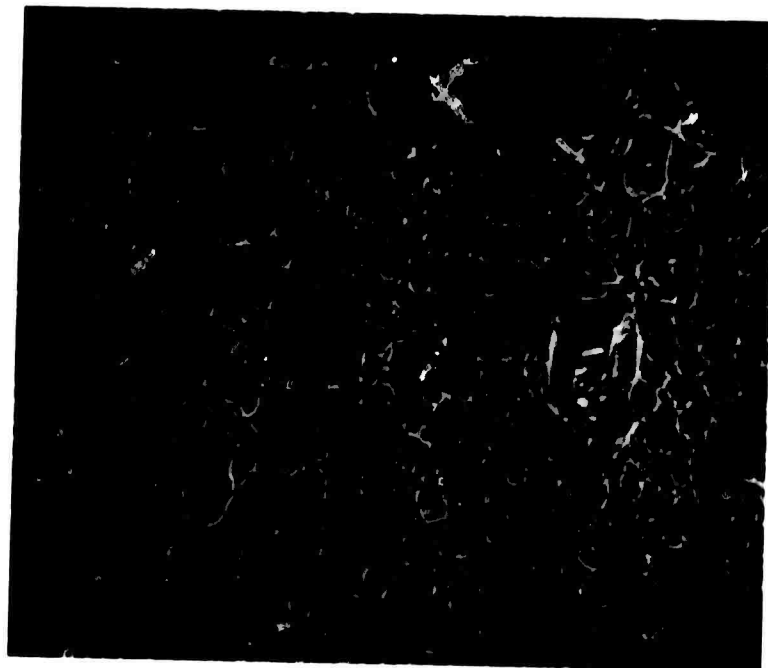
R = rolling direction

W = width direction

T = thickness direction

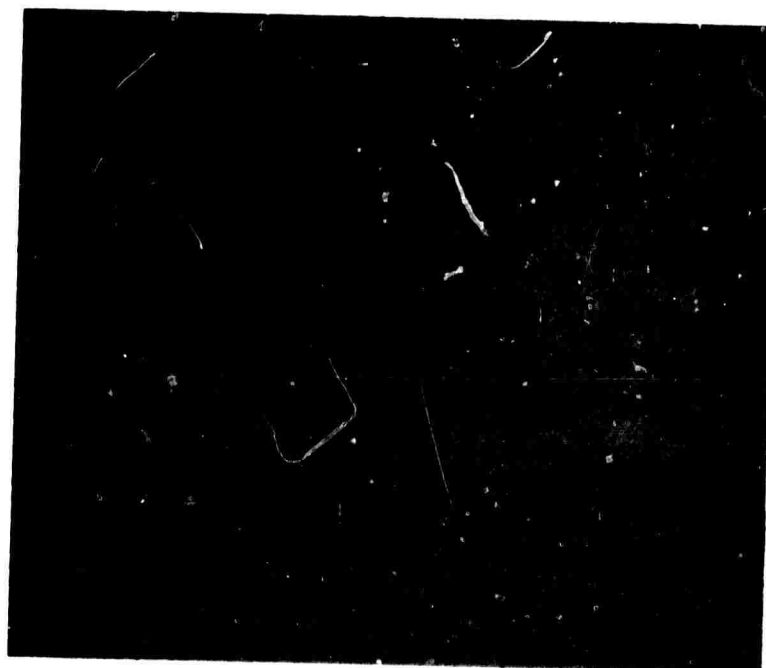
The first letter gives the direction of the Charpy bar.

The second letter gives the direction in which the crack will propagate.



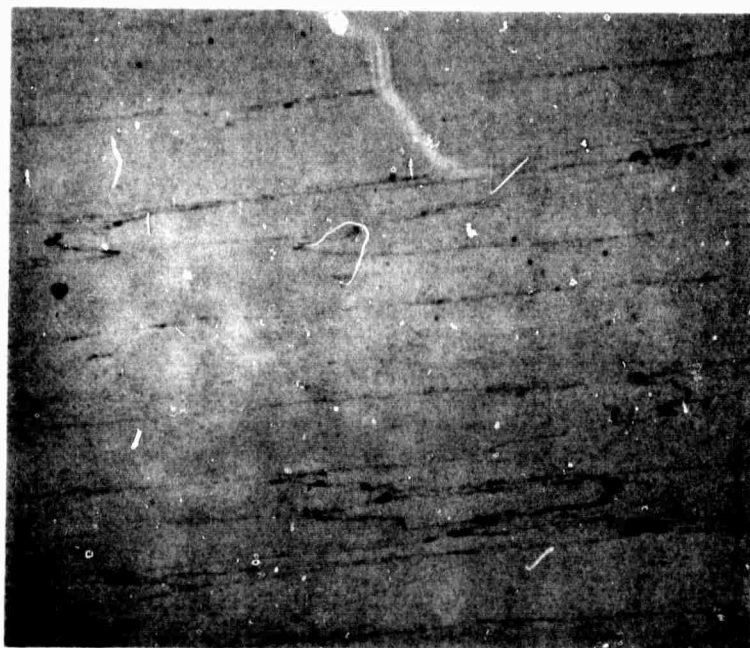
550X

Figure 1. Fracture surface of aged 300 grade Maraging steel. Note the inclusions in the large voids.



300X

Figure 2. Polished section of hot isostatic pressed Maraging steel powder produced by Nuclear Metals. Note the voids at the particle intersections.



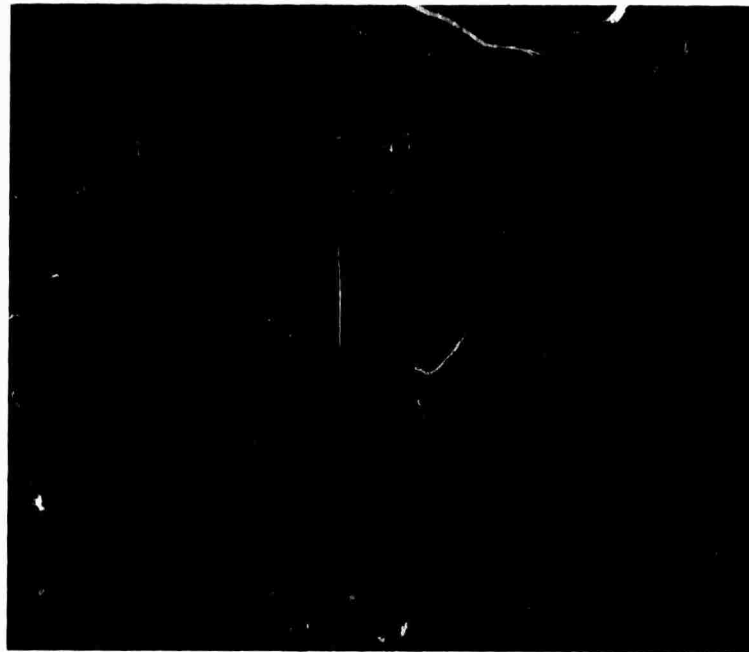
150X

Figure 3. Longitudinal section of extruded Maraging steel powder produced by Nuclear Metals. Etched with 10% HNO_3 propanol mixture.



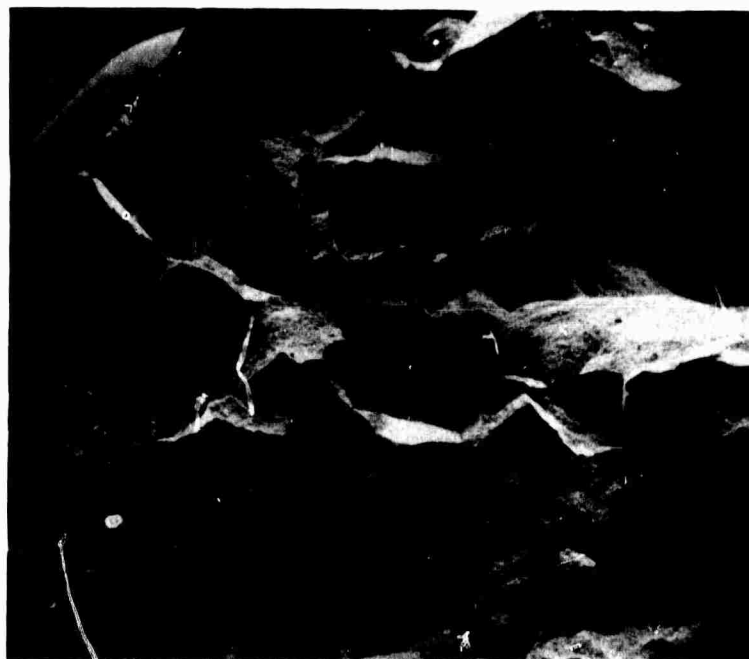
26X

Figure 4. Fracture surface of a tensile bar made from chill cast Maraging steel. The large shrinkage cavity in the center of the bar and the dendrite structure can be clearly seen.



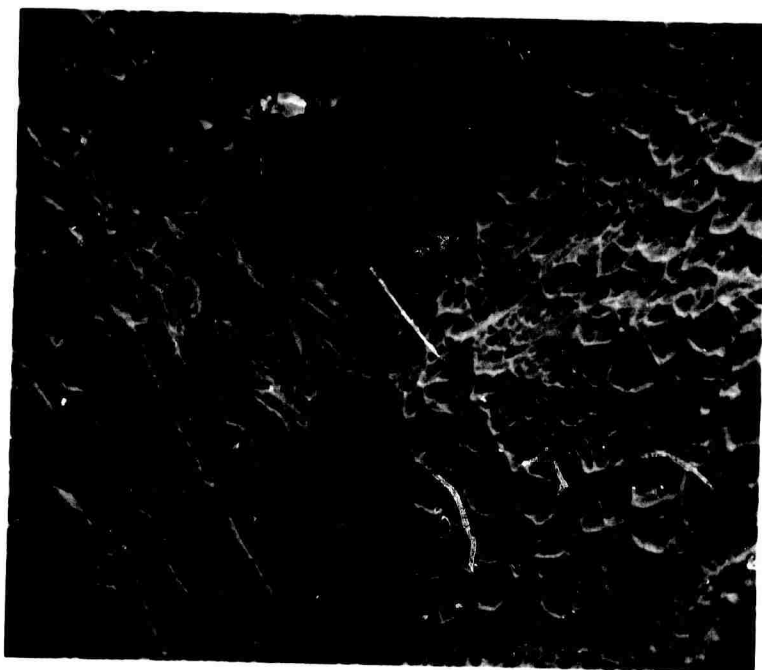
150X

Figure 5. Micrograph of hot isostatic pressed Maraging steel produced by chill casting. The straight line through the center of the picture is the interface of 2 bars.



50X

Figure 6. Fracture surface of chill cast and hot isostatic pressed Maraging steel showing grain boundary separation.



1900X

Figure 7 . A higher magnification of the fracture surface of Figure 6 showing grain boundary separation. The dimpled surface is typical of ductile fracture.

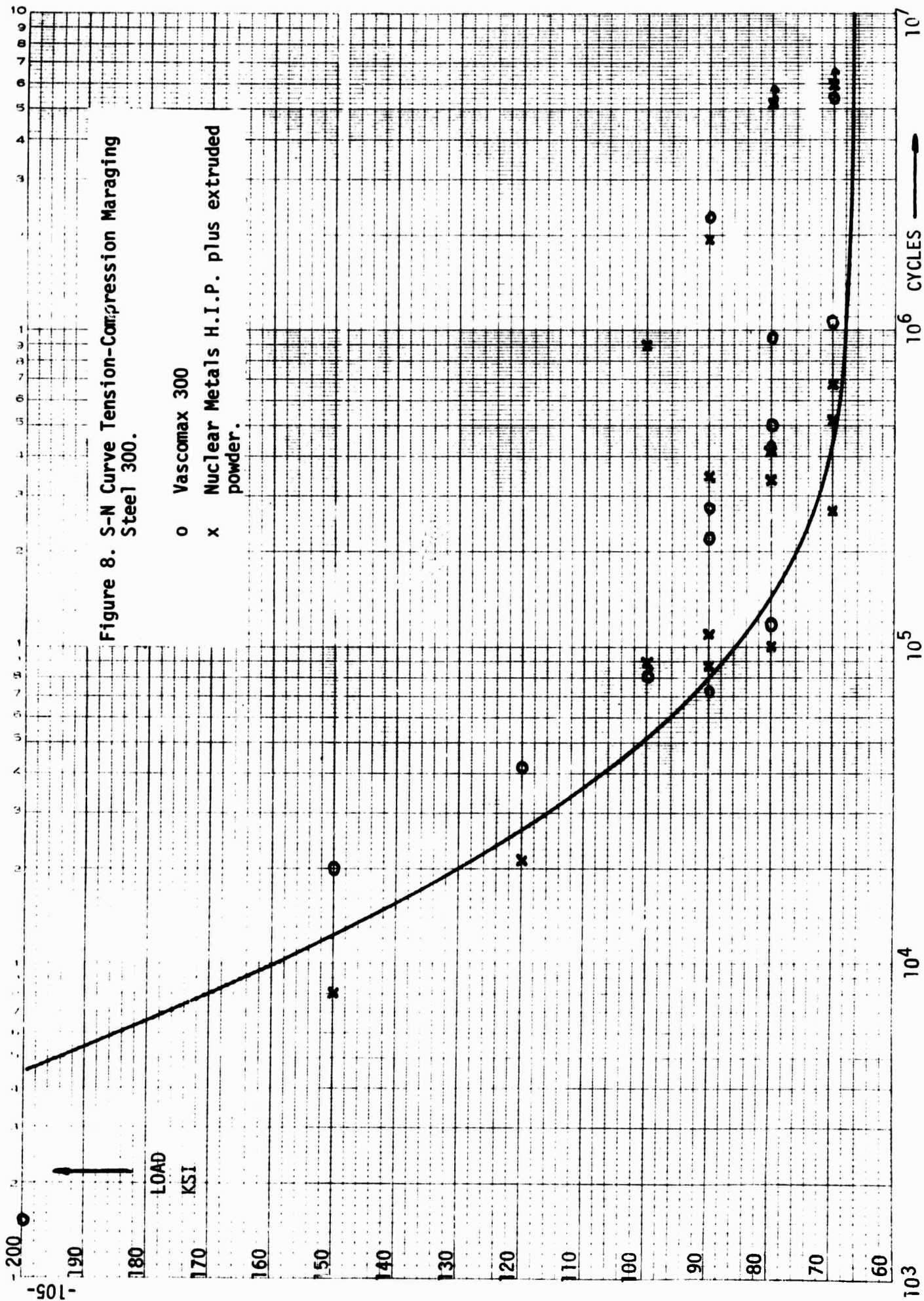


245X

Figure 9. Fracture surface of Charpy V-notch bar tested at liquid nitrogen temperature. The notch is shown on the right.

Figure 8. S-N Curve Tension-Compression Maraging Steel 300.

- o Vascomax 300
- x Nuclear Metals H.I.P. plus extruded powder.



HOT PLASTICITY OF IN-100

PROCESSED BY POWDER METALLURGY

INTRODUCTION

Hot plasticity stress-rupture tests were carried out on fine, hot isostatically pressed powders of IN-100. The -60 mesh powders were produced by Federal Mogul, using a vacuum remelted pre-alloyed ingot which was atomized with commercial high-purity argon gas. The composition in weight percent is given in Table 1. The average dendrite arm spacing was approximately 10^{-4} inches. (See Figures 1 and 2.) The hot isostatic pressing was performed at 2320°F and 25,000 psi for one hour. The resulting material had an average hardness of 49 R_c , and its microstructure is shown in Figures 3 through 7. It can be seen that little deformation of individual particles had taken place, and that the particle boundaries are surrounded by a network of a phase, tentatively identified as a carbide.

STRESS-RUPTURE TESTING

Twelve tensile bars were machined from the original bar with a gauge length of one inch and a diameter of .25 inch. Stress-rupture tests were performed on the Nemlab High Strain Rate Testing Machine at 1900°, 2000°, 2100° and 2200°F, the temperature range of conventional superalloy forging. Pre-heat time was less than ten minutes in all tests so as to avoid any grain growth that might have occurred. The results are presented in Table 2 and on a stress-rupture time plot, and the cross-sections of typical fractures are shown in Figures 8 and 9.

Poor ductility was exhibited at all temperatures and the strength level was relatively low. Fracture occurred at the particle boundaries and the influence of the surrounding phase was obviously great. The use of the scanning electron microscope and X-ray spectrometer showed the phase to be rich in titanium relative to nickel and aluminum, thus suggesting it was TiC. The examination of as-received powders (Fig. 10) gave no indication of the presence of this phase at the powder surface, and its formation

was probably a result of the H.I.P. processing. Further investigation into the effects of variables in H.I.P. processing will be made.

Samples of -20 mesh IN-100 powder produced by Homogeneous Metals were examined. The first had been hot isostatically pressed at 2300°F and 15,000 psi for one hour, and had an average hardness of 70 R_C . The second had been extruded after the same hot isostatic pressing. The extrusion temperature was 2000°F and the reduction ratio was 12:1. The average hardness of the cross-section was 40 R_C , and the microstructure is shown in Figs. 11 and 12. The entire length of extruded bar contained holes and cavities. This porosity is attributed to the presence in the powders of hydrogen, which was used in Homogeneous Metal's process to pressurize the melt and subsequently explode the rising stream of liquid metal.

At present, hot plasticity tests are about to be conducted on a 20:1 extrusion of Federal Mogul powders at 2150°F, without prior hot pressing or sintering. Positive identification of the phases at the particle boundaries is being made by extraction and X-ray analysis, and its effect on grain growth is being examined.

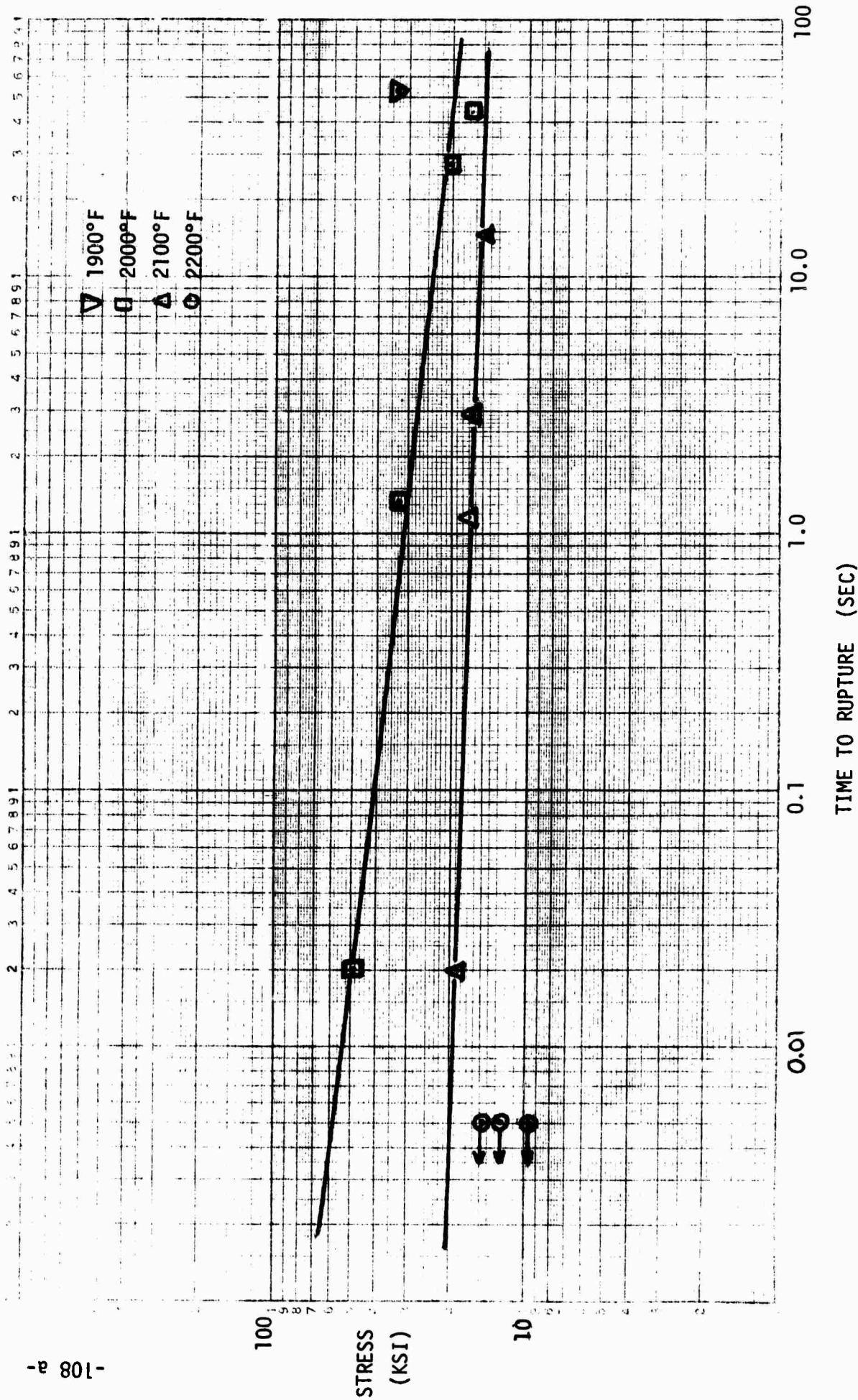
TABLE 1

Carbon	0.15 - 0.20
Manganese	max 0.20
Sulfur	max 0.015
Silicon	max 0.20
Chromium	8.00 - 11.00
Cobalt	13.00 - 17.00
Molybdenum	2.00 - 4.00
Titanium	4.50 - 5.00
Aluminum	5.00 - 6.00
Vanadium	0.70 - 1.20
Boron	0.01 - 0.02
Zirconium	0.03 - 0.09
Iron	max 1.00
Nickel	remainder

TABLE 2

	<u>stress (ksi)</u>	<u>time (sec)</u>	<u>elong. (%)</u>	<u>R.A. (%)</u>
1	<u>2000F</u> 16.9	43.83	2.9	2.4
2	20.2	27.58	1.3	1.0
3	32.1	1.33	1.5	2.4
4	48.1	0.02	1.1	4.0
5	<u>2100F</u> 14.4	14.79	1.4	3.8
6	16.3	2.91	1.2	3.9
7	16.9	1.16	1.2	6.3
8	18.2	0.02	1.6	7.3
9	<u>2200F</u> 14.4	< 0.005	1.5	6.4
10	12.2	< 0.005	2.4	1.0
11	9.6	< 0.005	1.0	1.0
12	<u>1900F</u> 32.1	53.55	2.3	3.5

-108a-



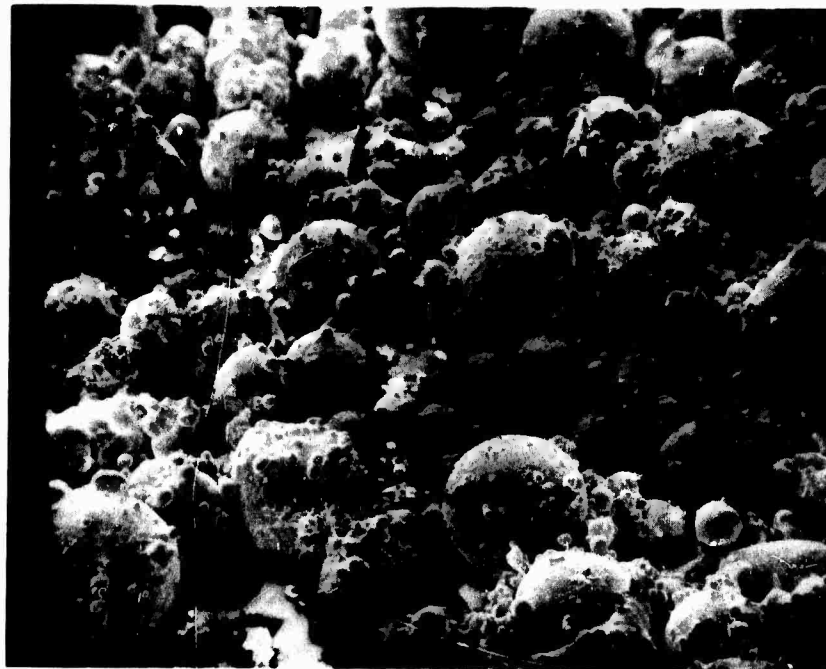


Figure 1. As-received Federal Mogul IN-100^{140X}
powders. Scanning Electron Microscope.

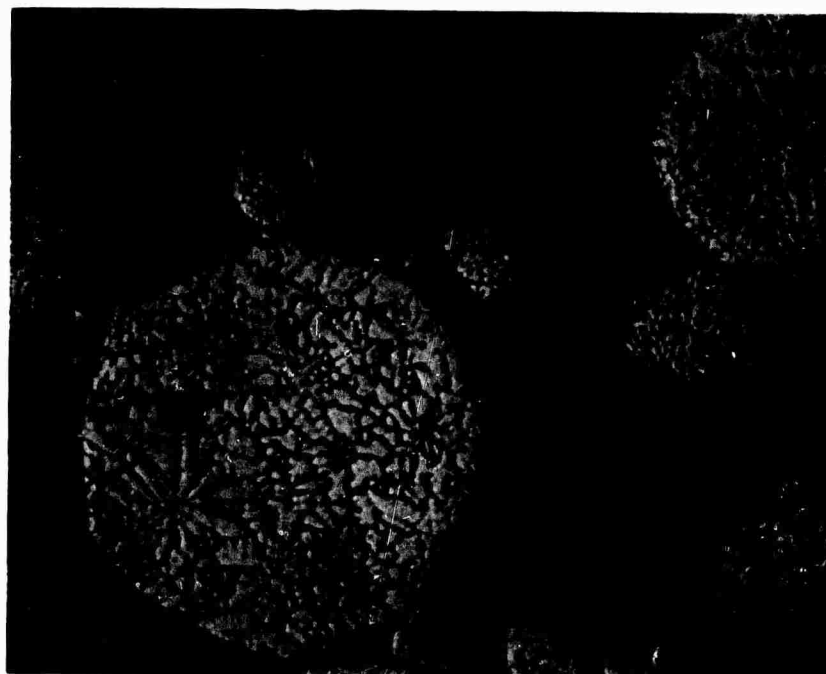


Figure 2. Polished and etched sections of^{500X}
above powders.

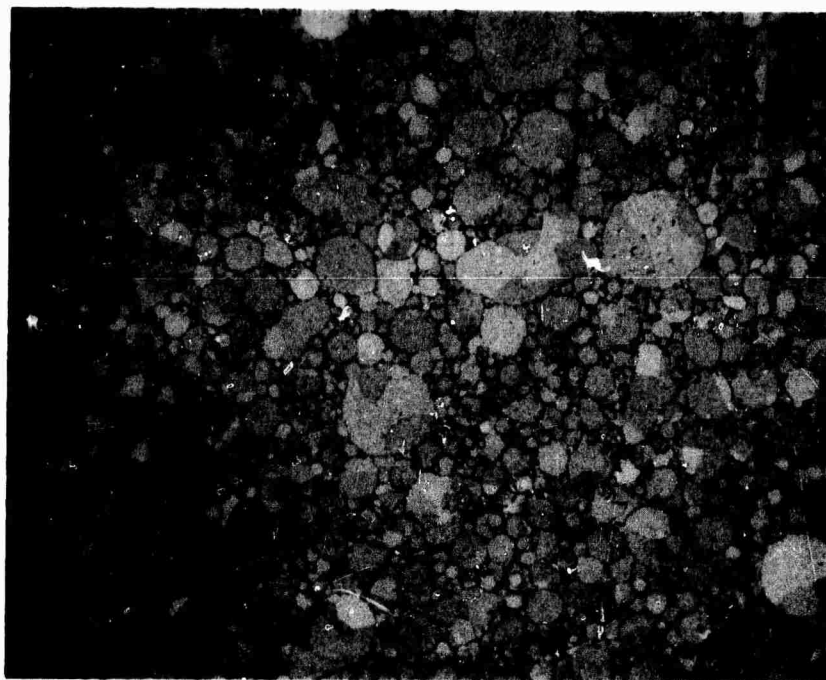


Figure 3. Hot isostatically pressed Federal Mogul IN-100 powders. 100X



Figure 4. Hot isostatically pressed Federal Mogul IN-100 powders. 500X

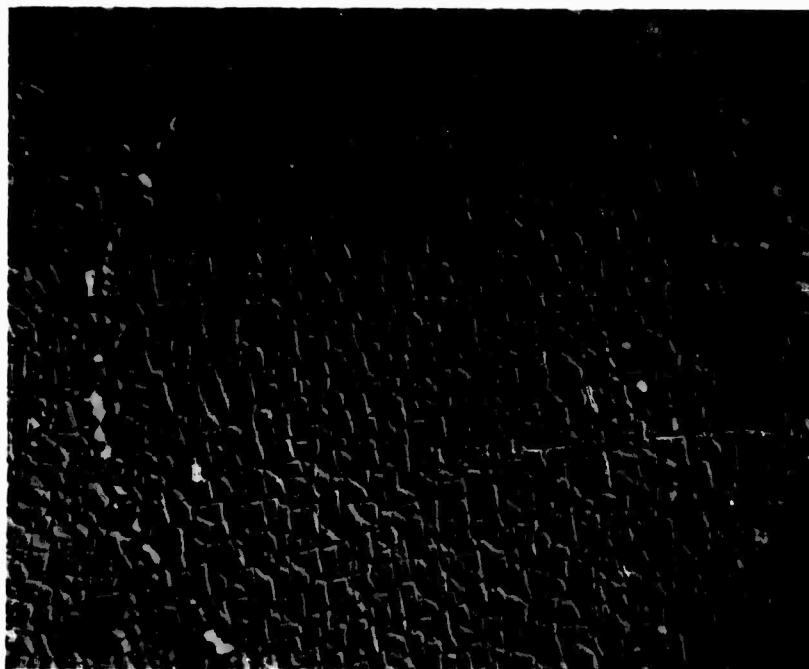


Figure 5. Hot isostatically pressed Federal Mogul IN-100 powders. Transmission Electron Microscope. 3200X

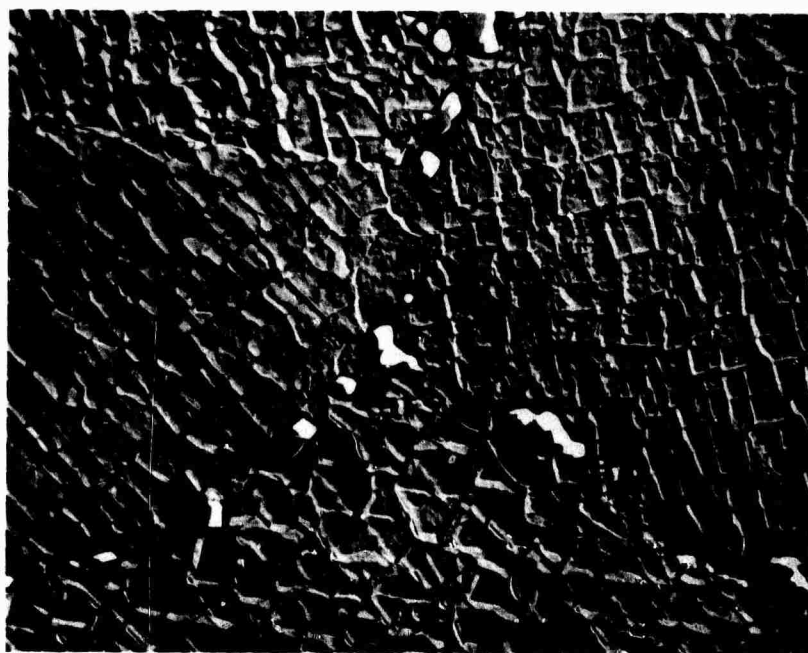
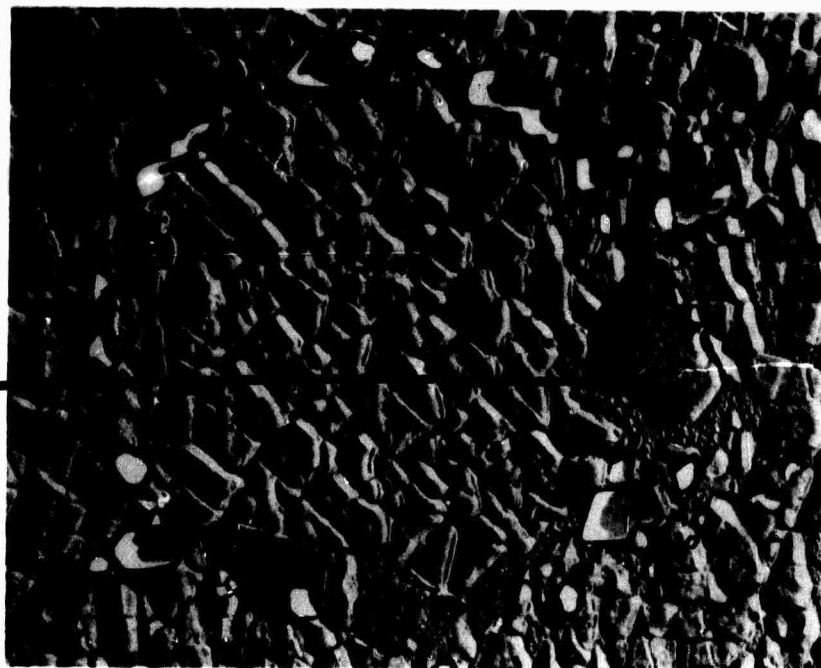
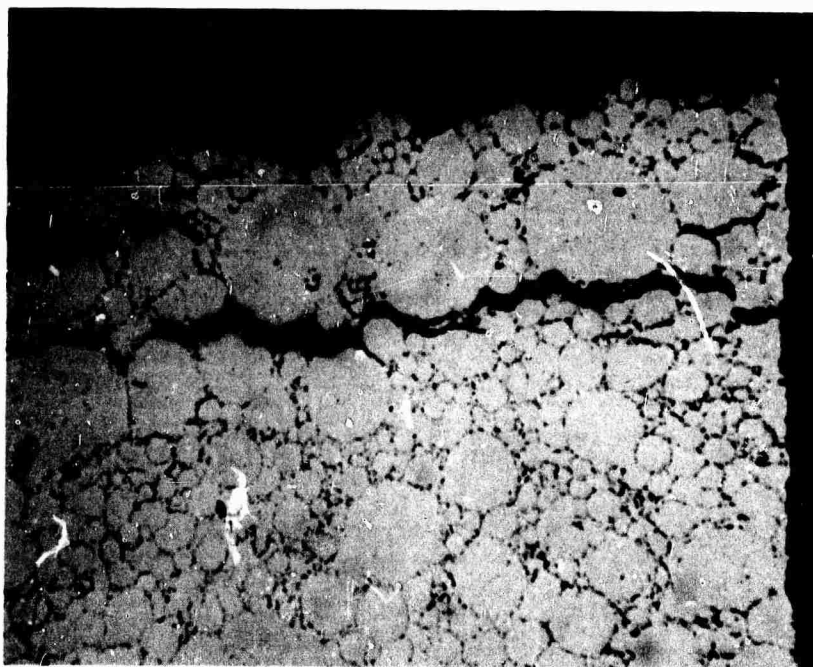


Figure 6. Hot isostatically pressed Federal Mogul IN-100 powders. T.E.M. 5400X



8000X
Figure 7. Hot isostatically pressed Federal Mogul IN-100 powders. T.E.M.



200X
Figure 8. Fracture cross-section of stress-rupture specimen. Unetched.

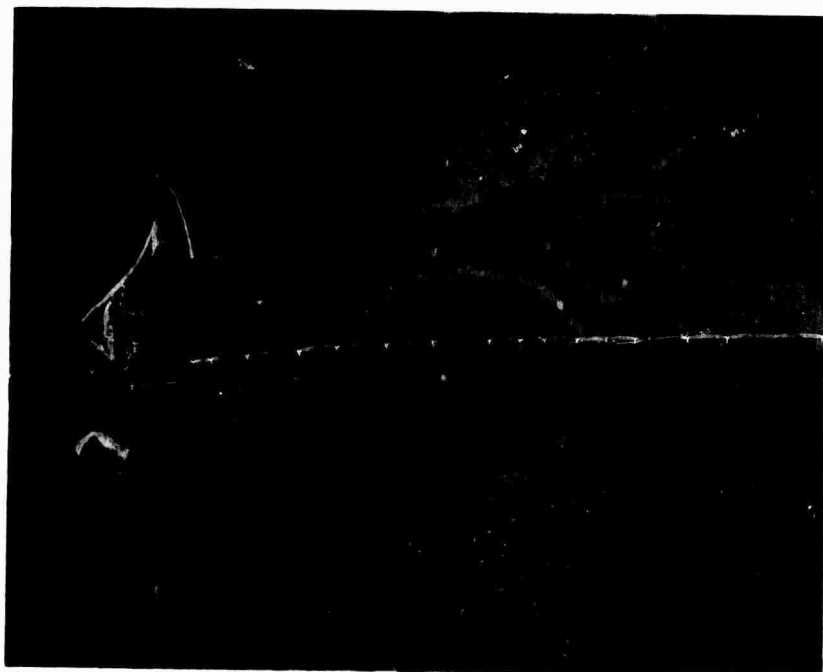


Figure 9. Fracture cross-section of stress-rupture specimen. Etched. 500X

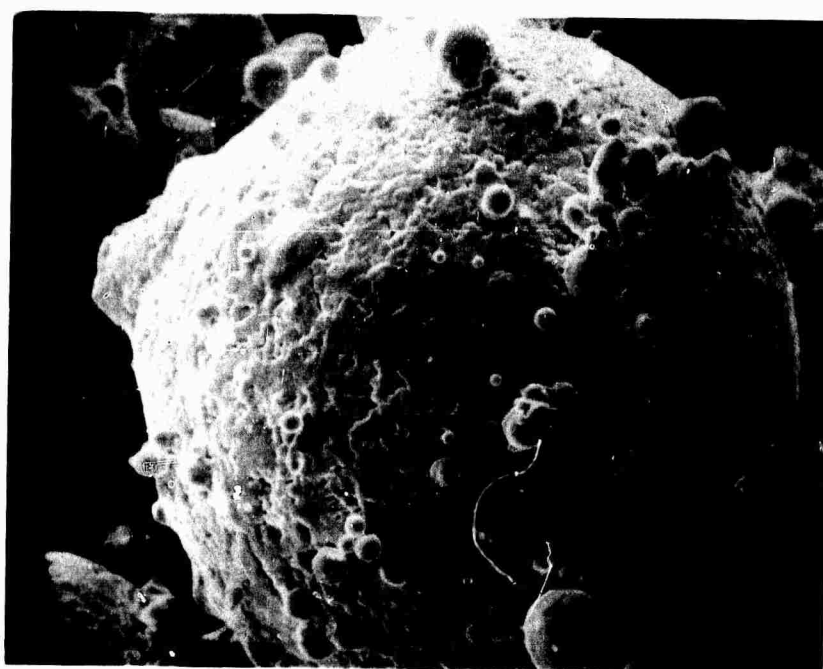


Figure 10. As-received Federal Mogul IN-100 powder surface. S.E.M. 700X

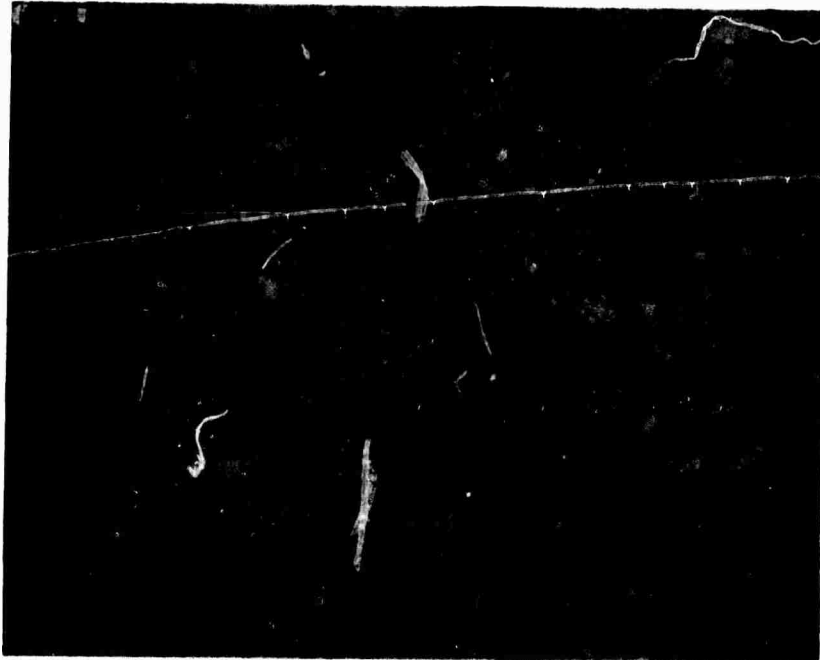


Figure 11. H.I.P. and extruded Homogeneous
Metals IN-100 powders. Transverse.

100X

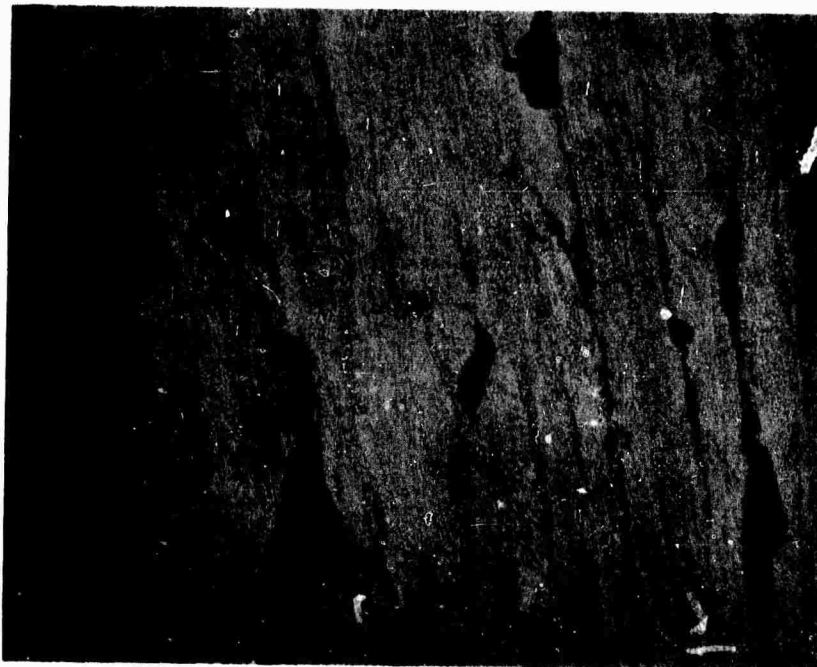


Figure 12. H.I.P. and extruded Homogeneous
Metals IN-100 powders. Longitudinal.

100X

THERMOMECHANICAL TREATMENTS,
MICROSTRUCTURE AND MECHANICAL PROPERTIES
OF COBALT ALLOYS

INTRODUCTION

Cobalt alloys are of significant interest in this program since most commercial cobalt alloys depend primarily upon carbide precipitation hardening for their high temperature strength. Control of the shape, size and distribution of the carbide phases in cobalt plus the potential for increasing the amount of carbide via the powder metallurgy structure-refinement route are indeed promising. Cobalt alloys in general have an intrinsic melting point advantage over nickel base alloys and have good hot sulfidation and stress rupture properties at the very high temperatures relative to nickel base alloys.¹

One of the best commercially available cobalt base superalloys is Martin-Marietta's MAR-M-509 casting alloy. Its 0.6% carbon content places it in the medium carbon casting alloys (Table I) and its 0.7%Ti + Zr and 3.5% Ta contents similarly are in the medium range for Group IV and V carbide formers (Table II). Tungsten or molybdenum is added for solid solution strengthening and chromium for corrosion resistance. Nickel is frequently employed in cobalt base alloys to austenitize the low temperature hexagonal close packed allotrope^{1,2}

Since the high temperature strength of cobalt is derived primarily from its carbide phases, the likely choice of a carbide-former would be one which had the greatest thermodynamic stability and highest melting point consistent with phase stability and precipitation hardening theory. An examination of the properties of the carbides (Table III)^{3,5} indicates that hafnium carbide is the most stable. Hafnium additions have recently been made of nickel alloys⁴ and molybdenum and tungsten alloys⁵ with beneficial results in ductility and/or strength. For comparative purposes, a Co-Hf alloy being developed in another MIT program was also selected for evaluation via the steam atomization, powder metallurgy approach. A 250-pound vacuum melted ingot with low oxygen (~ 24ppm) was selected as a master alloy. The composition of the Co-Hf alloy after various processing steps is listed in Table IV.

115

In order to have comparable data for evaluating the effects of powder metallurgy processing versus the cast alloy, a precision casting of tensile and stress rupture specimens of the Co-Hf alloy was made (Figure 1). Literature values for MAR-M-509 are adequate for comparisons of cast versus powder metallurgy in that alloy system.⁶

HEAT TREATMENT & AGEING OF COBALT ALLOYS

Four lots of material are currently being evaluated:

<u>Lot #</u>	<u>Alloy</u>	<u>Identity</u>	<u>Product</u>
1.	MAR-M-509-1	IMT #30-111	nominal 1/2" extruded rod
2.	MAR-M-509-2	IMT #30-112	" " "
3.	Co-Hf-1c	Precision Casting	1/4" dia. gauge
4.	Co-Hf-1e	IMT #30-217	nominal 1/2" extruded rod

The bulk of the evaluation to date has been on #1 and # 3.

Thermal treatments are being utilized in three major areas: solutioning prior to mechanical working or ageing, ageing treatments to develop optimum hardness, and grain coarsening treatments to enhance high temperature properties. Solutioning and ageing treatments are described below. Coarsening studies of Lots #1, 2 and 4 are being initiated utilizing a 2³ factorial design, three response test.⁷

The solutioning and ageing studies on MAR-M-509-1 are summarized in Table V and Figure 2. The as-extruded hardness of R_C 42.5 can be reduced to a low of R_C 27 with a 2265°F, 1 hour, water quench solution treatment. Maximum hardness on ageing with no intermediate cold work was R_C 44 using solution 4 treatment followed by ageing at 1450°F for approximately twenty hours.

THERMO-MECHANICAL TREATMENT

A 3.78" long x 0.470" diameter section of MAR-M-509-1 was subjected to solution 5 treatment and followed by room temperature swaging in five passes to a final diameter of 0.361" before the first end cracking was observed. This corresponds to a 41% reduction of area. Upon ageing, the peak hardness of R_C 58 is rapidly attained with a 1 hour treatment at 1000°F. Further ageing or higher temperatures lead to overageing as shown in Figure 2.

MECHANICAL PROPERTIES

Room temperature tensile tests were performed on MAR-M-509-1 in the as-extruded condition and upon Co-Hf-1c in the as-cast condition. Extruded specimens had 0.0160" diameter x 1.0-inch gauge lengths and the as-cast specimens had a nominal 0.25" diameter x 1.0-inch gauge length. An Instron tensile testing machine was utilized with an extensometer for determining elongation. Reduction of area measurements were made during testing using dial calipers. Cross head speeds of .01-.02 inches per minute were employed in all tests.

Tensile properties are summarized in Table VI. Note that the elongation, YS, and UTS of the powder metallurgy MAR-M-509-1 is significantly greater than the commercial material. There is excellent agreement in the measured vs. literature modulus for MAR-M-509-1.

The 509 alloy work hardens rapidly with a uniform reduction in area throughout the gauge length, i.e., there is little or only slight necking at fracture. The scanning electron microscope was employed to observe the fracture surface as shown in Figure 3. The top photograph shows where the fracture initiated and the lower photograph indicates the extremely fine dimpled structure of this material.

Elevated temperature (1800°F) stress rupture tests were performed on 509-1 and Co-Hf-1c using top loaded, cantilever beam stress rupture frames. Swivel ball top and bottom connecting joints minimize non-axial loading. A hydraulic jack is used to gradually add the predetermined load on the specimen. Furnaces are calibrated and preheated prior to loading with all tests performed with the controlling thermocouple attached at the gauge length position. Timers and dial gauges are used for accurate rupture time and strain elongation data.


The stress rupture data is summarized in Table VII and depicted on a log stress-log rupture time plot in Figure 4. The 509-1 high temperature strength in the as-extruded condition is significantly below that of commercial 509 (cast) while the elongations of the powder metallurgy 509-1 material is 10-12 times that of the commercial material. This superplasticity effect and simultaneous decrease in strength of the extruded powder material can be attributed primarily to the extremely fine grain size (approx. 2-5 microns). As noted in Figure 2, a 2285°F solution treatment for 1 hour plus ageing 20 hours at 1450°F did improve the as-extruded properties. Conversely, similar heat treatment of the Co-Hf-1c shows a tendency to decrease stress rupture properties, probably due to the already extremely coarse cast structure. Further work is in progress to determine the optimum thermal treatment(s)

to coarsen the grain size without degradation of the fine dispersion.

MICROSTRUCTURE

The beneficial refinements in microstructure due to the steam atomization, hot isostatically pressed and extrusion processes can be readily appreciated in Figure 5, comparing the Co-Hf alloy in the cast condition and the final as-extruded condition.

The peak hardness for 509-1 in the aged condition both with and without intermediate cold work came from specimens with the microstructures depicted in Figure 6.



REFERENCES

1. Sims, Chester T. " A Contemporary View of Cobalt-Base Alloys",
Journal of Metals (Dec 1969), pp 27-42
2. Morral, F.R. "The Metallurgy of Cobalt Alloys - A 1968 Review",
Journal of Metals (July 1968)
3. Lemkey, F.D. & Thompson, E.R., "Nickel & Cobalt Eutectic Alloys
Reinforced by Refractory Metal Carbides", Metallurgical
Trans, 2, 6 (June 1971) p. 1538
4. "Ductility Improvement Discovery", Martin-Marietta News Release on
MM 004, 1970
5. Klopp, W.D., et. al. "Strengthening of Mo & W Alloys with HfC",
Journal of Metals (June 1971) pp. 27-38
6. "MAR-M-509 DATA Sheets", Martin Marietta News Release
7. Hunter, W.G. and Hoff, M.E., "Planning Experiments to Increase
Research Efficiency", Ind. & Engr. Chem., 59, 3 (Mar 67)
pp. 43-49

- TABLE I -

Characterization of cobalt-base alloys according to

nickel carbon composition

(weight percent)

Nickel

LOW
<.25%

LOW
<5%

ML-1700 (c)
Illium D
UMCO 50 (cast)

MEDIUM
5-15%

AF-94
WF-11, L-605, HS-25
WF-31
Elgiloy
XSH

HIGH
>15%

J-1570
J-1650
M-203
M-204
M-205
MAR-M-918
HAYNES 188
NIVCO-10
I-336
25-Ni
MP-20N

Carbon

MEDIUM
.25-.75 %

UMCO-51 (c)
AIRESIST 13 (c)
NASA-Co, W, Re
WI-52 (c)
HAYNES 151 (c)
HS-21 (c)
HS-23, 61 (c)
UMCO-51

X-40, HS-31 (c)
X-45 (c)
X-63 (c)
MAR-M-509 (c)
HS-30, 422-19 (c)
HS-36, L-251 (c)
HE-1049
CF-43 (c)
G-32
"J" alloy

X-50 (c)

S-816
V-36
HS-27, 6059 (c)
ONERAL S-90 (c)
ATS-113

HIGH
>.75%

MAR-M-302 (c)
MAR-M-322 (c)
Illium X

G-34 (c)
ONERAL M-47 (c)

(c) = castings typically

- TABLE II -

Characterization of cobalt-base alloys according to
Group IV + V vs VI composition (weight percent)

<u>Mo+W</u>	<u>NONE</u>	<u>MEDIUM 10-7%</u>	<u>Nb+Ta+Ti+Zr</u>
<u>LOW < 7%</u>	X-63 (c) HS-30,422-19 (c)	G.32	<u>HIGH > 7%</u>
<u>MEDIUM 7-11%</u>	X-40, HS-31 (c) X-45, (c) CF-43 (c)	MAR-M-509 (c) 3.5 Ta, .7 Ti+Zr AR-213 (c) 6.5 Ta	SM-302 (c) 9 Ta, .2 Zr MM-322 (c) 4.5 Ta, .75 Ti, 2.3 Zr
<u>HIGH > 11</u>	HS-36, L-251 (c) HE-1049 (c)		

(c) = castings typically.

12-1

- TABLE III -

Properties of Carbides

Carbide	Melting Point °C (°F)	Density, g/cc	Lattice Parameter, Å	Heat of Fusion, kcal/gfw	Elastic Modulus, 10 ⁶ psi	Microhardness kg/mm ²	Oxidation Rate mg/cm ² /hr	Free Energy of Formation kcal/g at., 1500°C
VC	2650, peritectic (4800)	5.8	4.16	--	37	2950 to 2250	900°C, 73.5	---
TiC	3067, max at TiC _{0.8} (5570)	4.9	4.33	20	45-64	3200 to 2850	1000°C, 3.57	-38
ZrC	3420, max at ZrC _{0.81} (6200)	6.4	4.70	20	--	2830 to 2560	900°C, 46	-39
NbC	3600, max at NbC _{0.82} (6500)	7.8	4.47	22	49	2400 to 2020	900°C, 20.5	-36
HfC	3928, max at HfC _{0.94} (7100)	12.7	4.64	--	62	2700	----	-43
TaC	4000, max at TaC _{0.82} (7200)	14.5	4.6	25	57	1800 to 1500	900°C, 20.5	-38

122

- TABLE IV -

Co-Hf Compositions (Wt%)

		(wet chemical analysis)		
	<u>Vacuum Melt Charge</u>	<u>Primary Ingot (A-L)</u>	<u>Precision Cast (Bldg 8)</u>	<u>Steam Atom (IMT)</u>
Hf	5.25	4.0	2.5	2.6
Cr	21.0	18.2 (21.6)*	16.3 (20.8)*	20.1 (20.9)*
Mo	6.75	5.6	6.8	5.5
Ni	10.0	9.9 (8.4)*	(8.5)*	10.0 (8.35)*
C	0.25	0.24	0.28	.205
Hf/C (atom %)	1.4	1.11	0.6	0.85
		<u>37.94</u>	<u>34.98</u>	<u>39.255</u>
<u>Co</u>	<u>(Bal)</u>	<u>62</u>	<u>65</u>	<u>61</u>

* Atomic absorption

123

- TABLE V -

Heat treatment of cobalt alloys

TREATMENT #	SOLUTION CONDITION			HARDNESS			AGEING		
	temp.	atmos- phere	time	quench	sample	condition	R _C [*]	conditions	R _C
1	2275°F	air	90 min	wq	509-1	as ext.	30.5(5)	None	
2	2192°F	air	60 min	wq	509-1	as ext.	37.5(8)	None	
3	2500°F	air	60 min	Ac	509-1	as ext.	19.5(3)	None	
4	2350°F	air	60 min	wq	509-1 509-1	as ext. sol.#2	32 (8) 31 (4)	20, 45, 90 mins 1450°F	R _C 44
5	2255°F	vac	60 min	wq	509-1	as ext.	27	CW, then aged (see Fig 2)	
6	2260°F	vac	60 min	Ac	509-1 509-1	sol.#2 sol.#5 plus 30% CW	33.5(3) 37.0(2)	20 min., 1500°F 20 min., 1800°F None	32(3) 38(2)
7	2275°F	vac	60 min	Ac wq wq wq	509-1 509-1 509-1 509-111	as ext. as ext. sol.#5 plus 41% CW as HIP	40.0(3) 41.5(3) 32.5(1) 37.5(4)		
8	2285°F	vac	60 min	wq	509-1	machined specimen	29 (3)	20 min, 1450°F	R _C 41.5(3)
					509-1	sol.#7	33 (2)		41.0(3)
					509-111	as HIP	32 (4)		45 (3)
					Co-Hf 1	cast specimen	23 (3)		29.5(3)

* All hardness values are Rockwell C; (No.)-bar over number indicates average number of measurements.

124

- TABLE VI -

Tensile properties of cobalt-base alloys

ALLOY	TEST	ENGINEERING DATA				TRUE STRESS-STRAIN DATA			
		$\frac{A_0-A_f}{A_0}$ (%)	$\frac{l_f-l_0}{l_0}$ (%)	Yield Strength (0.2%) (KSI)	UTS (KSI)	$E_f = \ln \frac{A_0}{A_f}$ or $E_f = \ln \frac{l_f}{l_0}$	$\frac{UTS}{(KSI)}$	Young's Modulus $(KSI \times 10^3)$	Work* Hardening Exponent "n"
MAR-M-509-1 As extruded	1	-	8.67	135	189	.0906	207	—	0.20
	2		13.8	123	195	.165	226	33	0.20
MAR-M-509 Commercial	1		1.5	70	110		91.5	32.7	
	2		3.5	90	120				
Co-Hf-1 As cast	② 1		11	55	68.5				
	2			66	82	.0965		30	0.17

* Where $\sigma = K \cdot \epsilon^n$

① From Martin-Marietta data sheets

② contained shrinkage porosity

125

-119- A

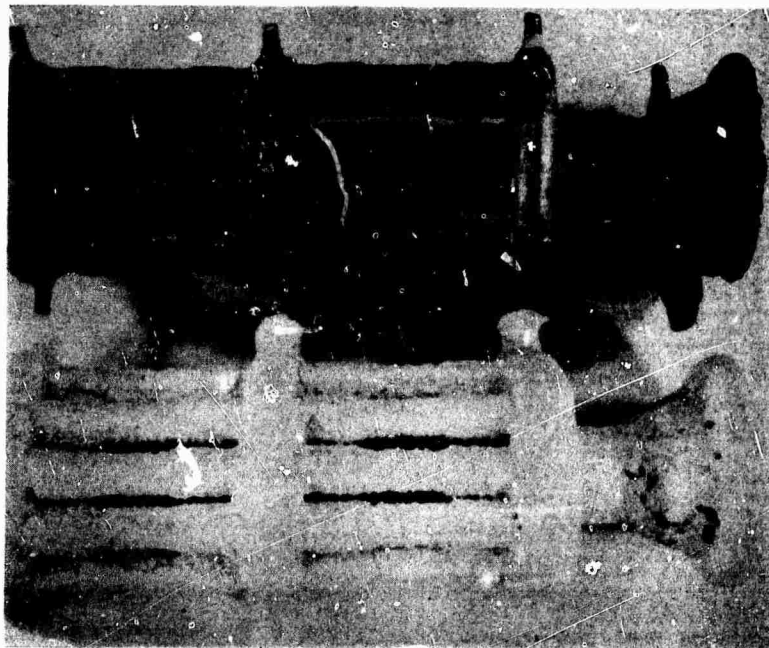


Figure 1 : Precision cast Co-Hf tensile & stress rupture specimens . $\frac{1}{3} \times$.

126

- TABLE VII -

Stress rupture data - Cobalt alloys

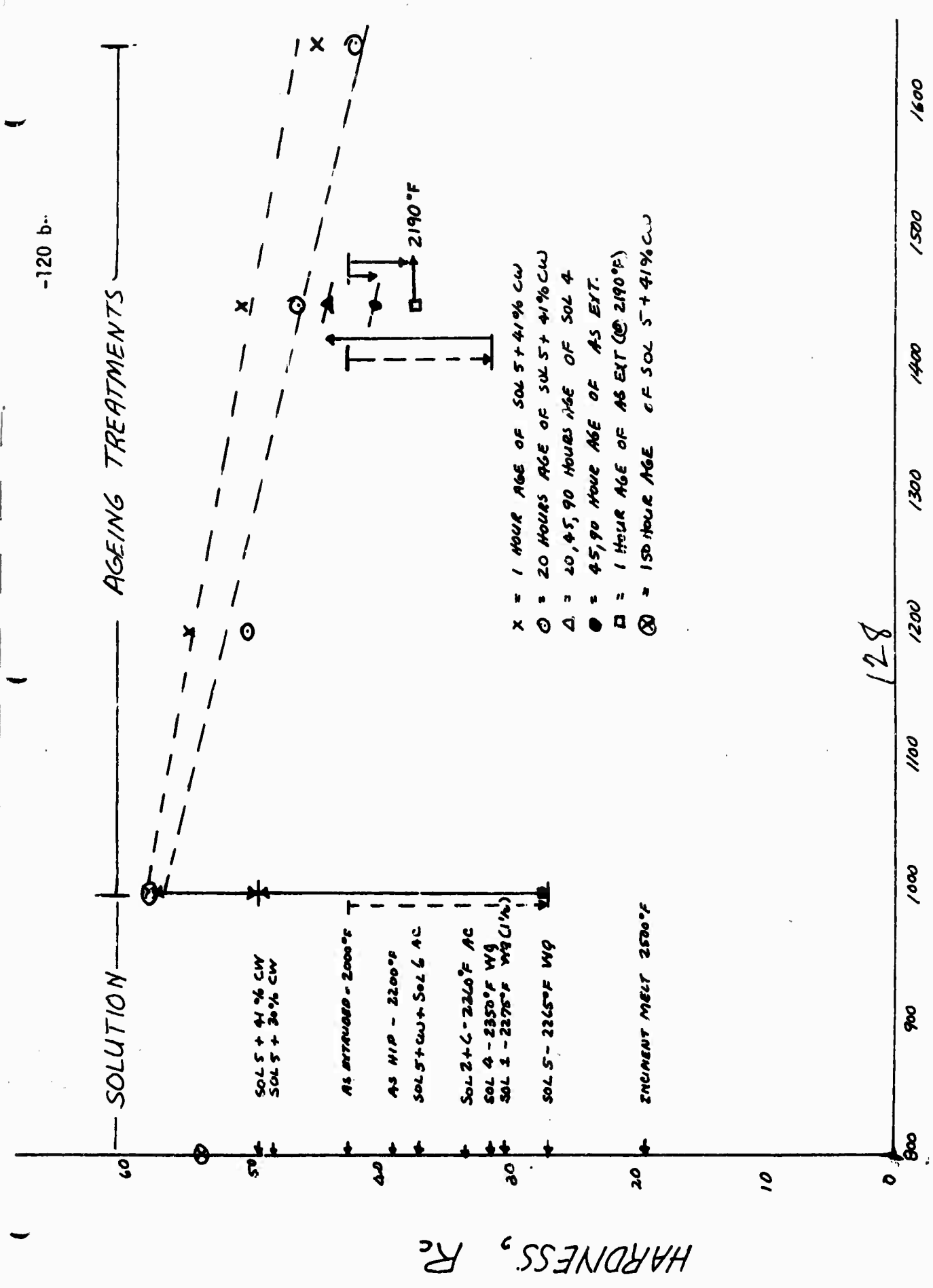
<u>ALLOY</u>	<u>CONDITION</u>		<u>LIFE</u>	<u>EL</u>	<u>RA</u>	<u>COMMENTS</u>
	<u>(°F)</u>	<u>(KSI)</u>	<u>(HRS)</u>	<u>(%)</u>	<u>(%)</u>	
MAR-M-509-T ↑ (as Ext.) ↓	1800	2.75	72.5	98	56.6	#32
	1800	4.0	15.3	95.5	57.7	
	1800	10.0	0.85	120	57.0	# 1
	1800	17.0	0.095	56	51.0	
	1800	10.0	17.0	10	6.1	#21 - av.
(SOL + Age*)	1800	17	0.762	~10	6.1	- approx. elong.

Co-Hf	1800	10.0	27.2+	18.8		- test continue
(cast)	1800	12.0	2.4	13.0		- shoulder failure
↓	1800	14.0	1.1+	10.9		- test continue
↑	1800	6.0	281 +	1.0		- test continue
(SOL + Age)	1800	8.0	2.0	8.9		- shoulder fail
↓	1800	10.0	10.8	19.9		

Typical(Lit)						
Commercial						
MAR-M-509	1800	10.0	3,218	8.0	10.2	
↑	1800	13.0	1,000			
(cast)	1800	17.0	100			
↓	1800	17.5	27	10.0	9.6	

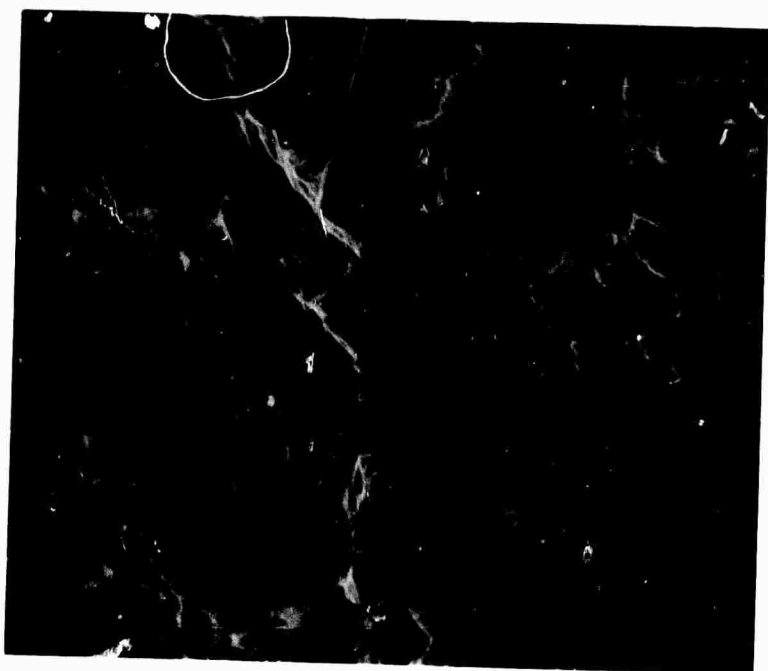
127

* Solution 2285°F, 1 hour, w.q.; age 20 hours - 1450°F



128

FIG 2: MAR-M-509 HEAT TREAT & THERMAL-MECH. TREAT.



7000 X.



56 X.

129

Figure 3 : Room temperature tensile fracture of MAR-M-509-1

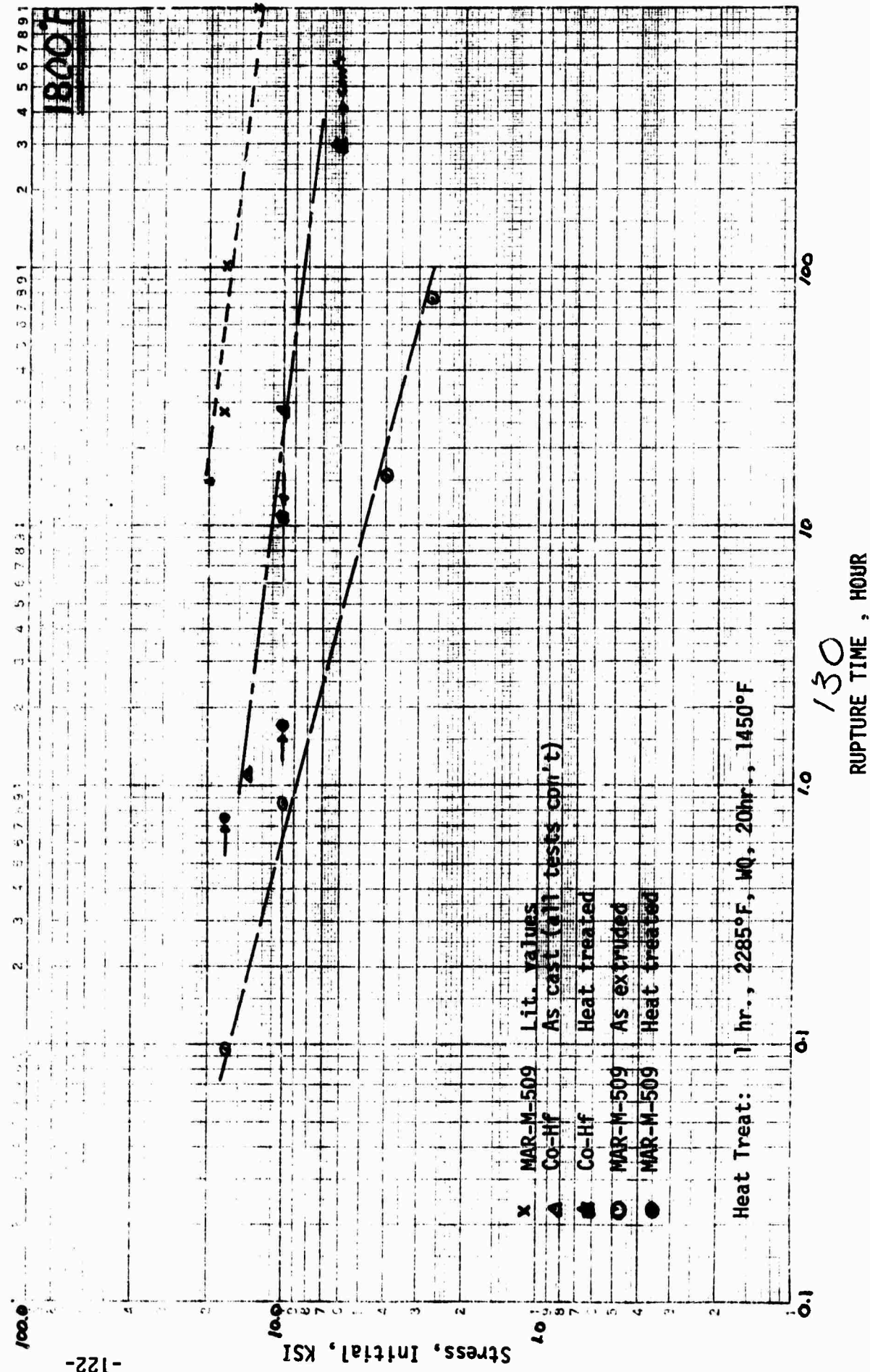
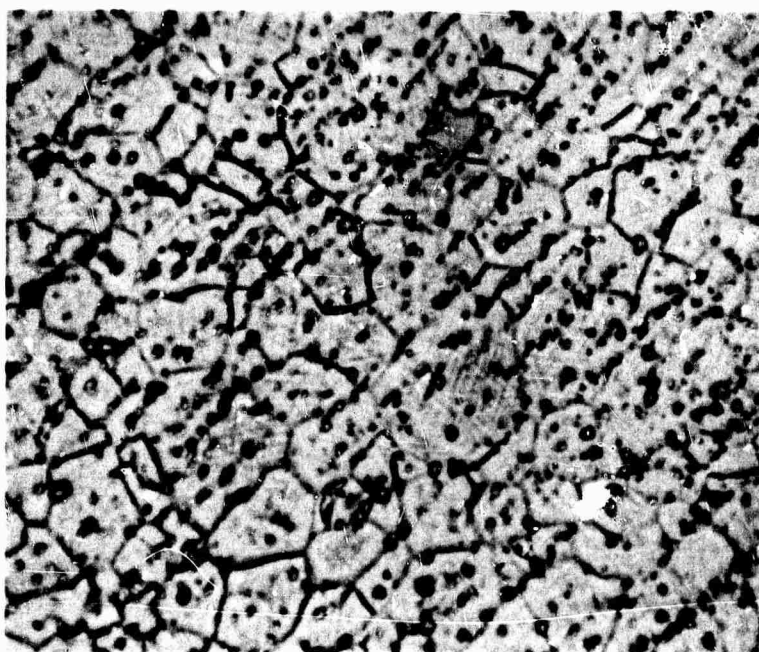


Figure 4. : Stress Rupture Properties for Cobalt Base Alloys at 1800°F

-122-A

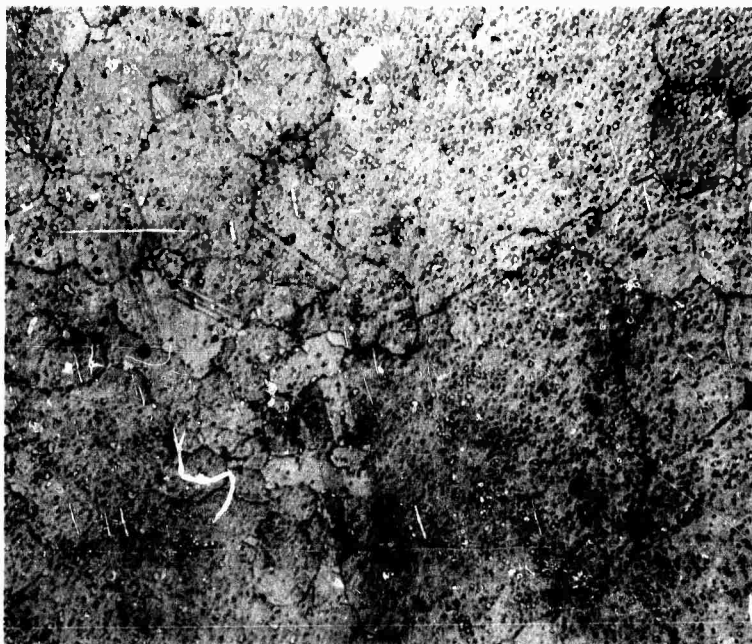


131

Figures 5 : Structure refinement due to powder process. 1500x.

Top: As cast Co-Hf master ingot with massive carbides

Bottom: As extruded powder met. Co-Hf-1



132

Figures 6 : Peak hardness structures for MAR-M-509-1

Top: Sol. + age. 300x.

Lower Sol. + 41% cold work + age . 750x.

Microstructure and Mechanical Behavior
of Commercial and HIP Maraging Steels

by A. S. Argon

Personnel: A. S. Argon, Professor of Mechanical Engineering
K. Ghosh, Visiting Engineer
R. Lee, Research Assistant
N. Surg, Part-time Assistant

Introduction

The areas of tensile ductility and stress-corrosion cracking were singled out for study during the first year of the program. The work progressed in close association with another program on the study of the role of inclusions in ductile fracture^(*). Some of the theoretical work developed in the latter research will be summarized below together with the developments in this research to give a coherent picture of the total program as it applies to the study of various commercial and hot isostatically pressed (HIP) maraging steels.

It has been well recognized that the tensile ductility and fracture toughness of an engineering, structural material can be enhanced by controlling nucleation of holes from inclusions. Once such holes have been nucleated they grow by a plastic expansion process under a triaxial tensile stress. Since the portion of the tensile ductility based on growth and linking of existing holes is strictly a deformation problem, it is less variable than the

^{*)} Work supported by the National Science Foundation under Grant # GK1875X1.

portion based on the development of holes by inhomogeneous plastic deformation around inclusions. The latter includes physical and metallurgical aspects which govern the interfacial strength of the inclusions.

In the first part of the report the processes of inclusion separation and hole growth will be discussed in addition to the more conventional descriptions of mechanical behavior of the maraging steels tested.

In the second part of the report the progress on the study of the stress corrosion cracking will be described.

Part I. Tensile Ductility

1.1 Hole Formation from Inclusions

Holes are formed from inclusions by either separation of the inclusions from the matrix at the interface or by fracture of the inclusion. Equiaxed inclusions almost always separate from the matrix by decohesion at the interface. Elongated inclusions on the other hand, frequently form holes, by fracture in the inclusion. In either case, if the inclusion has smooth surfaces the local stress across the interface or in the interior of the inclusion has to reach the cohesive strength of the interface or that of the inclusion, respectively. This process is envisioned to come about from the inhomogeneous plastic flow around the inclusion in the ductile matrix. Cavitation in the ductile matrix material, away from the interface is unlikely since stresses can always be relaxed to some extent by plastic flow.

Below, the process of hole nucleation by decohesion at the interface will be discussed theoretically both on the basis of continuum plasticity for large inclusions, and dislocation mechanics for small inclusions.

1.2 Hole Formation from Widely Separated Large Inclusions

The problem of the stress and strain distribution around a rigid inclusion in an inhomogeneous plastic flow field of a strain hardening plastic material is not yet soluble even with numerical, finite element approaches, especially when the plastic strains are large. It is, however, possible to obtain reasonably narrow bounds for the distribution of stresses and plastic strains around the inclusion by idealizing the behavior of the plastic matrix material into a non-hardening, and linearly hardening one as shown in Fig. 1.

The solution to the problem of plastic flow of a non-hardening material in pure shear around a rigid circular particle in plane strain is best obtained by a finite element method. The result of such a study shows that after the entire matrix material has become fully plastic, the maximum interfacial stress becomes very nearly

$$\sigma_{rr} = \frac{\sqrt{3}}{2} \gamma \quad (1)$$

where γ is the tensile flow stress, and the term in the denominator arises from the use of the Mises flow rule.

The corresponding problem of plastic flow of a linearly hardening material in pure shear around a rigid circular particle in plane strain can be obtained directly from the theory of plane strain elasticity by substitution of 0.5 for Poisson's ratio in the equations. In this case the maximum interfacial radial stress is somewhat higher,

$$\sigma_{rr} = \frac{2\gamma}{\sqrt{3}} \quad (2)$$

Naturally in both cases if a long range triaxial tensile stress is present in the vicinity of the inclusion, it must be added to interfacial stresses calculated for the case of pure shear. Based on these rather different idealized limiting behaviors of the plastic matrix, the interfacial stress can

be bounded as

$$\frac{\sqrt{3}Y}{2} < \sigma_{rr} - \sigma_T < \frac{2Y}{\sqrt{3}}, \quad (3)$$

where σ_T is the triaxial tensile stress. As has been discussed by McClintock and Rhee⁽²⁾, the behavior of the real material must indeed lie within these two limits.

Evidently, the interfacial tensile stress is only slightly higher than the flow stress of the matrix, and can rise to high values only to the extent the matrix can strain harden.

The above analysis is appropriate for large inclusions where the inclusion size is very much larger than the mean inclusion spacing, and a continuum approach is the correct one. For very small inclusions, however, the inclusion size may be much smaller than the mean dislocation spacing so that continuum deformation around the inclusion is not possible. In the latter case the problem must be solved by dislocation mechanics.

The exact form of dislocation accumulation around inclusions depends on the specific crystallography of the deforming matrix. A good estimate of the interfacial stress can be obtained for a general case by adopting a prismatic dislocation punching model introduced first by Ashby⁽³⁾. The model, illustrated in Fig. 2, is based on producing only the necessary prismatic dislocations to spread out the displacement incompatibilities between matrix and particle into prismatic punching zones shown in Fig. 2. The interfacial stresses can be calculated from an approximate model of punching an elastic cylinder into a cylindrical rigid cavity with either constant or displacement dependent surface shear tractions as shown in Fig. 3. These two models represent a non-hardening material and a linearly hardening material respectively. The two solutions for the interfacial surface stresses are⁽⁴⁾

$$\sigma_{rr} = \sqrt{2\sqrt{2} E k_0 \gamma} \quad (4)$$

for non-hardening matrix with yield strength in shear k_0 , and

$$\sigma_{rr} = \sqrt{E k_0 \left(\frac{\theta}{k_0} \gamma^2 + 2\sqrt{2} \gamma \right)}, \quad (5)$$

for linearly hardening material with yield strength in shear k_0 and strain hardening rate θ .

Taking the second of the above expression as more appropriate, and evaluating it for

$$E = 2.5G; k_0/G = 1/600; \theta/G = 1/600,$$

one finds that $\sigma_{rr} = 0.1 E$ for $\gamma = 2.7$.

This indicates, for strains of the order of $\epsilon = 2.7/\sqrt{3}$ (150%) interface decohesion is possible if the stresses around the particle can not be relaxed earlier.

The conditions for plastic relaxation when the local dislocation density becomes too large, have been investigated by Im ⁽⁴⁾ who finds that transition from discrete dislocation behavior to continuum behavior will occur at a shear strain

$$\gamma_t = \frac{b}{r_0 f} \quad (6)$$

where b is the magnitude of the Burgers vector, r_0 the particle radius and f is the volume fraction of the second phase.

Equations (3), (4) and (5) for continuum behavior and discrete dislocation behavior are independent of particle size, indicating that when the particles are non-interacting, separation can occur for small or larger particles alike for the same strain. In practice, however, it is found that large inclusions

separate before small ones do. The explanation of this can be found only in particle interactions which is discussed below.

1.3 Hole Formation between Interacting Particles of Uniform Size

With increasing plastic strain the zones of inhomogeneous plastic strain around particles will interact as shown in Fig. 4. In this case the zones of inhomogeneous plastic zone will remain of fixed size instead of growing with the shear strain. The interfacial stress can again be readily calculated and is found to be

$$\sigma_{rr} = \frac{E\gamma}{2} \frac{1}{\left[\left(\frac{\pi}{6f}\right)^{1/3} - 1\right]} \left\{ 1 + \frac{4\sqrt{2}}{E\gamma} \left[\left(\frac{\pi}{6f}\right)^{1/3} - 1\right]^2 \right\}, \quad (7)$$

where the symbols have the same meaning as before. The interfacial stress is now dependent on the volume fraction f of second phase but ^{is} still independent of particle size.

1.4 Hole Formation Between Interacting Particles of Different Size

In real materials there is always a distribution of particle sizes. In this case the interparticle spacing must depend on the average particle radius \bar{r}_0 , and particle size dependent interfacial stresses should now appear since larger incompatibility displacements have to be accommodated in smaller interparticle spaces. The solution of this problem gives for the interfacial stress between particles of radius r_0 for a population of particles of average radius \bar{r}_0 ,

$$\sigma_{rr} = \frac{E\gamma}{2} \left(\frac{r_0}{\bar{r}_0}\right) \frac{1}{\left[\left(\frac{\pi}{6f}\right)^{1/3} - 1\right]} \quad (8)$$

This indicates that for a family of particles of different sizes but constant interparticle distance, the interfacial stress increases directly with particle

size. A somewhat similar argument has been advanced by Ashby⁽³⁾.

2. Experimental Procedure

2.1 Material used

Experiments were conducted on three different materials.

- a) Commercial Vascomax 300 purchased from Teledyne Vasco.
- b) Hot isostatically pressed Maraging 300 Alloy with some large hollow inclusions, manufactured by IMT and received as a 0.75" dia rod.
- c) Hot isostatically pressed Maraging 300 Alloy of higher grade, manufactured by IMT and received as a 0.75" dia rod.

All the maraging material was tested either in the unaged condition or in the age hardened condition produced by heating to 1400°F for one hour, air cooling to room temperature, heating to 900°F for 3 hours, and furnace cooling.

2.2 Specimen Shape

Experiments were performed in tension on round bars of both uniform cross section and pre-machined natural neck profiles to give a range of ratios of neck radius to neck profile radius of curvature. A wider range of triaxial tensile stress was produced by the latter specimens. Specimens with natural profiles were preferred over plane strain specimens because for natural neck specimens Bridgman's⁽⁵⁾ approximate solution provides stress and strain distributions in the specimen valid for relatively large strains in non hardening materials. For linearly hardening material the solution of Neuber⁽⁶⁾ could be used.

Of particular interest are the distributions of triaxial tensile stress along the radial direction in the smallest cross section as well as along the axis of the specimen away from the plane of the smallest cross section. Of

further interest is the distribution of equivalent plastic strain along the axis to determine the local plastic drag and the interfacial tensile stress which it produces.

The solution for the triaxial stress along the radial direction in the smallest cross section and along the axial direction away from the narrowest cross section for a non-hardening material is

$$\frac{\sigma_T}{Y} = \frac{1}{3} + \ln\left(\frac{a^2 + 2aR - r^2}{2aR}\right) \quad \text{along } z = 0 \quad (9)$$

$$\frac{\sigma_T}{Y} = \frac{1}{3} + \ln\left(\frac{a^2 + 2aR}{2aR}\right) - \frac{2 + \ln\left(\frac{a^2 + 2aR}{2aR}\right)}{(a^2 + 2aR + z^2)/z^2} \quad \text{along } r = 0 \quad (10)$$

where the latter has a range of validity only for distances z for which the triaxial stress is larger than $Y/3$, and where a is the radius of the narrowest section, and R the profile radius of curvature at the narrowest section.

The distributions of triaxial stress along the narrowest section and along the z axis away from the narrowest section ^{for a linearly hardening material} are given by

$$\frac{\sigma_T}{p} = \frac{C}{\sqrt{1 - \left(\frac{r}{\bar{a}}\right)^2}} \quad \text{along } z = 0 \quad (11)$$

$$\frac{\sigma_T}{p} = \frac{C}{\sqrt{1 + \left(\frac{z}{\bar{a}}\right)^2}} \quad \text{along } r = 0 \quad (12)$$

where

$$\bar{a} = \frac{a\sqrt{1 + \frac{a}{R}}}{\sqrt{\frac{a}{R}}}$$

$$C = \frac{1 + \frac{a}{R} + \sqrt{1 + \frac{a}{R}}}{2\left(2 + \frac{a}{R} + \sqrt{1 + \frac{a}{R}}\right)} \quad 140 \quad p = \frac{\text{Applied Load}}{\pi a^2}$$

Inspection of equations (9) and (11) shows that for the non-hardening material the triaxial stress is maximized along the axis while for the linearly hardening material it is maximum at the surface of the narrowest cross-section.

Finally the distribution of plastic strain along the z axis in the neck region is obtained from geometry as

$$\epsilon^p = \ln \frac{R_0'^2 (1 - \cos \alpha_0)}{R_1'^2 (1 - \cos \alpha_1)} \quad (13)$$

where the quantities R_0' , R_1' , and α_1 , defined in Fig. 5 are directly measurable and the angle α_0 is calculable by equating the volume enclosed by the spherical cap going through Z_0 in the initial shape to the corresponding volume in the distorted shape containing the point Z. The latter procedure is tedious and requires machine calculation.

The specimens of the commercial Vasco 300 material were provided with pre-machined neck profiles resembling a notch as shown in Fig. 6. These profiles in which the shape differs significantly from that of a natural neck are known to have non-uniform plastic strain increment distributions at the narrowest cross section (7,8) introducing errors into the Bridgman analysis. Although, as Norris (8) has shown, the plastic strain increments in across the section become uniform upon straining, going asymptotically to the Bridgman strain distribution, the results deduced from these tests should not be taken as completely reliable.

The specimens of the Maraging 300 HIP alloys, produced by IMT, were machined to natural neck geometries based on empirical profile curves based on the measurements of $\text{Im}^{(4)}$ on copper. The results obtained from these experiments can be considered as more reliable.

3 Experimental Results

3.1 Tensile Behavior

The stress strain curves for all material at room temperature are shown in Fig. 7 for specimens with initially uniform cross sectional demensions, and for a test strain rate of 10^{-3} sec^{-1} . The pertinent parameters of yield stress, tensile strength, strain hardening rate, uniform extension are summarized in Table I.

In the experiments where it was necessary to stop the machine several times in the post necking region, to make area measurements, large deformation transients and unloading yield phenomena were observed such as those shown in Fig. 8. In the past such deformation transients have been attributed to transients in the mobile dislocation density and to changes in the deformation structures between states. These deformation transients will be investigated further.

3.2 Microstructure

The microstructure of the three materials was investigated both before the tensile test and after the tensile test. In the interest of economy only on axial cuts going through the specimen axis will be discussed. For such observation those microstructures which were made on fractured specimens *one side of the fractured specimens were given a heavy nickel* coating. The specimens were then milled down to the axial plane mounted in lucite, and metallographically polished. Some specimens were given a light Pickral etch to delineate better the microstructure and inclusions. In the unaged commercial Vascomax 300, large inclusions of 15μ average size were encountered at a volume density of $1.5 \cdot 10^6 \text{ cm}^{-3}$. These large inclusions shown in Fig. 9 were most likely titanium carbide. As will be discussed below they play a role in ductile fracture. In addition to the large inclusions mentioned above, many small etch pits were seen especially near the fracture surface.

Judging from the size of the etch pits these inclusions were of the order of 0.1μ and at a volume density of $5 \cdot 10^{10} \text{ cm}^{-3}$. They are shown in Fig. 9 and are thought to be Ni_3Mo . These too play a prominent role in ductile fracture of this material.

In the aged Vascomax 300 far fewer inclusions were found. There were still occasional large inclusions of about $1\text{-}2\mu$ size. No small inclusions could be detected from etch pits. The general appearance of the etched axial cross section was cleaner. Yet the roughness of the profile of the ductile fracture surface was largely unaltered. A characteristic cross section is shown in Fig. 10. In all of the aged alloy specimens axial cracks were observed. One such small crack is shown in Fig. 10. The propensity for axial cracking increased with increasing (a/R) ratios, i.e. with increasing levels of triaxial stress.

The grain size in the unaged Vascomax 300 can be measured from Fig. 9 as being approximately $40\text{-}50\mu$. The grain size in the aged alloy could not readily be determined.

In the first hot isostatically pressed Maraging 300 Alloy bar received from IMT a number of large, round, hollow inclusions ^{of iron oxide} of $\sim 50\mu$ size were found. Several such inclusions are shown in the axial section of Fig. 11 in an unaged specimen. In addition to the hollow inclusions a second family of equiaxed but irregular polygonal shaped inclusions, were also found. These inclusions too can be seen in Fig. 11. Their density shown in Fig. 11 is unrepresentatively large. The wave length of the fracture surface dimples seen in Fig. 11 suggests yet a smaller size inclusion of much larger density. The identity of none of these inclusions has yet been determined. All these inclusions were also found in the aged specimens as Fig. 12 shows. In one of the aged specimens of the first bar received from IMT large inhomogeneities were found. These

are shown in Fig. 13. These regions had distinctly different plastic behavior and tensile ductility. Figures 14 and 15 show large internal cracking by ductile fracture in one of the streaks of high inclusion concentration. The inhomogeneous microstructure of this specimen is, however, non-representative and has come most likely from one of the ends.

3.3 Tensile Ductility

3.3.1 Commercial Vascomax 300 Alloy

The tensile ductility of all specimens with special initially manufactured notched profiles of different a/R ratios, of both the unaged and aged commercial Vascomax 300 Alloy are given in Tables II and III respectively together with the pertinent data on initial and final a/R ratios and the calculated maximum triaxial tensile stress. As expected, inspection of Tables II and III shows a decreasing strain to fracture with increasing triaxial tensile stress.

The conditions for hole nucleation were investigated in the Vascomax 300 alloy by determining the cumulative number of separated inclusions along a narrow strip on the axial microsections. These cumulative counts are shown in Figs. 16 and 17 for unaged and aged material respectively for the four different specimen profiles. The separated inclusions represented only the population of the large titanium carbide inclusions. No small separated inclusions could be seen in the light micrographs. From the position of the last separated inclusion along the z axis the local equivalent plastic strain was determined either by means of Eq. (13) or by a graphical construction. The results are given in Tables IV and V for the unaged and aged material. The interfacial strength of the titanium carbide inclusions was then determined by means of the stress strain curves and Eqs. (3) and (9). The calculated interfacial strengths for both the unaged and the aged material are given in Tables IV and V.

144

The conditions for separation of the small inclusions could not be determined in a similar way since these inclusions were not observable in either the light microscope or the scanning electron microscope.

3.3.2 Maraging 300 HIP Alloy with Large Hollow Inclusions

The tensile ductility of all specimens with specially machined natural neck profiles of different a/R ratios in both the unaged and aged conditions are given in Tables VI and VII respectively together with the pertinent data on the initial and final a/R ratios and the calculated maximum triaxial tensile stress at the center of the specimens. Since the final a/R ratios at fracture were always above the initial a/R ratios not much variation in triaxial tensile stress was achieved in these experiments, hence no trend in strain to fracture with changing triaxial stress can be distinguished.

Since the large hollow inclusions were well adhered to the matrix and the coarse titanium carbide inclusions were absent, and since no unique association could be made between the fracture surface dimples and a much finer set of inclusions, no determinations could be made of the conditions of inclusion separation comparable with those discussed in the last section.

4. Discussion of Results

The calculated values of the interfacial strength given in Tables IV and V for the commercial Vascomax 300 Alloy corresponds to an elastic strain of 0.012 in the matrix at separation. This compares favorably with the ideal elastic fracture strain of 0.035 - 0.045 measured in iron whiskers by Brenner⁽⁹⁾. It is not unnatural to expect that the ideal elastic strain at fracture across

the interface be somewhat less than that of the matrix. McClintock and O'Day⁽¹⁰⁾ measured in soap bubble rafts a 50% reduction of ideal fracture strain of high angle grain boundaries below that of the perfect raft. In view of this we consider our results representing near-ideal behavior of the interfaces.

In the commercial Vascomax 300 Alloy fracture was governed by two distinctly different sizes of inclusions. The large titanium carbide inclusions and the much smaller inclusions which were most likely Ni_3Mo . The stereo-scanning electron micrograph shown in Fig. 18 for Specimen #7 in the aged condition was typical of the appearance of all of these alloys whether unaged or aged. The large dimples surrounding the titanium carbide inclusions are separated by a second dimple size which is more than a factor of ten smaller. Figure 19 shows these smaller dimples at somewhat larger magnification. No inclusions could be found at the bottom of these dimples, suggesting that they had been lost either during the fracture or during the subsequent ultrasonic cleaning operation. Table VIII shows the difference between the total fracture strain and the strain for hole nucleation in the Vascomax 300 alloy. This difference is associated with the strain for inclusion growth and linking which occurs as a process of plastic expansion of these holes primarily in response to the triaxial tensile stress. A clear trend of decrease of this growth strain with increasing triaxial tensile stress is shown in Table VIII. In the last column of the table the growth strain is compared with the theoretical calculation of McClintock, as formally generalized for a three dimensional case

$$\epsilon_g = \frac{(1-n) \ln(a/2r_0)}{\sinh((1-n) \sigma_T/\gamma)} \quad (14)$$

In Eq. (14) n is the strain hardening exponent, a the effective inclusion spacing, r_0 the inclusion radius, and $\sigma_{T/Y}$ is the ratio of the triaxial tensile stress to the tensile flow stress given in Tables II and III. The figures given in the last column of Table VIII should be equal to the natural logarithm of the ratio of the inclusion spacing to the inclusion diameter. Evidently this value is unacceptably small and does not remain constant. The reason for this discrepancy could be either in the fact that the smaller inclusions might separate at smaller strains than the larger ones but remain undetected by scanning microscopy leading to larger growth strains than measured, or that the formal generalization of McClintock's plane-strain formula into three dimensions as is given above is invalid. Comparison of the total strains to fracture for the commercial Maraging steel and the atomized and hotisostatically pressed material shows that the HIP material has about 12% more ductility in the unaged and 28% more ductility in the aged state, confirming the advantage of the hotisostatic pressing process. Since there are compositional changes in the HIP material resulting from the atomization process, the apparent advantage is not well documented.

147

Part II. Stress-Corrosion Cracking Experiments

The objective of these experiments is to generate information on stress-corrosion behavior of 18 Ni, Maraging-300 steel in 3% aqueous sodium chloride solution. Specifically, it is intended to produce data on the value of K_{Isc} and crack growth rate as a function of K_I . Both commercially available material and the material produced by the experimental method of steam atomization followed by hot isostatic pressing (HIP) is being tested. The sodium chloride solution is maintained at room temperature and the surface is exposed to air.

1. Design of the Specimen

The resistance of materials to stress corrosion is usually assessed by measuring the time to fracture of a smooth or notched specimen in a corrosive environment. The life of the specimen in such tests is governed primarily by the time taken for a critical corrosion pit to form and grow to a sufficient size to initiate a stress-corrosion crack. From the standpoint of usefulness for design, data on growth rate of cracks is more important. Specimens suitable for studying stress-corrosion cracking making use of fracture mechanics are similar to those used in conventional fracture-toughness testing. A number of standard specimen shapes (11-15) and K-calibrations for such specimens (14,16-20) are available in the literature. A crackline-loaded specimen is most suitable for crack-growth measurements. By suitably contouring a ^{double cantilever beam (DCB)} DGB specimen, it is possible to have a constant value of K with change in crack length for a constant load. Such a specimen can be used for crack growth measurements at a constant load (and constant K) or the crack can be arrested at any desired point by reducing the load.

In designing a specimen for this series of experiments, the treatment of Ripling et al (20) was followed. The minimum specimen thickness b_n , the minimum crack length a_o were determined using the relationship

$$\left. \begin{matrix} b_n \\ a_o \end{matrix} \right\} \geq 2.5 \left(\frac{K_{Ii}}{\sigma_{ys}} \right) \quad (15)$$

where K_{Ii} = maximum expected value of K_I during test

σ_{ys} = yield strength of the material.

Using $K_{Ii} = 50 \text{ Ksi } \sqrt{In}$

and $\sigma_{ys} = 280 \text{ Ksi}$

we get $\left. \begin{matrix} b_n \\ a_o \end{matrix} \right\} \geq 0.0796"$

The specimen thickness at the crack plane will be assumed to be 0.1" and this will ensure plane strain conditions. For a DCB specimen, the so-called crack extension force G_I , is

$$G_I = \frac{P^2}{2b_n} \frac{\partial C}{\partial a} \quad (16)$$

where P = applied load

b_n = specimen thickness at crack plane

C = specimen compliance, when the crack length is "a",

$$G_I = \frac{(1 - \nu^2)}{E} K_I^2$$

with E = modulus of elasticity

ν = Poisson's Ratio

149

If the specimen is designed such that $\frac{\partial c}{\partial a}$ is a constant, then the relation between P and G (and hence K) is independent of a. As the crack extends, G_{Ic} and K_{Ic} varies only with the critical load P_c .

Using beam theory, it is easy to show that (Ripling, et al (20)):

$$\frac{dc}{da} = \frac{8}{Eb} \left[\frac{3a^2}{h^3} + \frac{1}{h} \right] \quad (17)$$

where h is the beam height at distance a from the point of loading.

For $\frac{dc}{da}$ to be constant,

$$m = \frac{3a^2}{h^3} + \frac{1}{h} \text{ has to be constant.}$$

The taper of the specimen is steeper, the smaller the value of m. The choice of a proper value of m is one of compromise. Large taper angles are useful for producing straight cracks. On the other hand, experience with different specimens have indicated that by decreasing the taper angle, the crack arrest capability is enhanced.

In this case, a value of 4 was chosen for m.

The relationship

$$m = \frac{3a^2}{h^3} + \frac{1}{h}$$

then yields the possible combinations of values for a and h, which define the specimen shape.

The shape of the specimen which was finally picked is shown in Fig. 19b.

150

2. The Experimental Apparatus photograph

Figure 20 shows a photograph of the testing machine. It consists of two arms, hinged together at a fulcrum. The specimen is supported at the bottom end. At the top end, the arms are pulled together by a low stiffness spring to minimize load drop during crack growth. The arms, the specimen support links, and the fulcrum links are made of Hastelloy C alloy which has superior corrosion resistance in sodium chloride solution.

The spring force is amplified 5 times by the levers, and the spring constant of 200 lb/in was chosen in such a way that the variation of the load at the specimen due to the extension of the crack will be limited to 5%. The crack opening displacement is monitored by using a differential transformer mounted on the arm above the spring as shown in Fig. 20. The spring load is measured by strain gauges attached to the tensioning bolt. Both the load and displacement are continuously recorded on a chart recorder.

3. Experimental Results

Experiments are now in progress to measure the crack growth rates in 3% sodium chloride solution as a function of K_I in the unaged and aged condition in both the commercial Vascomax 300 as well as in the Maraging 300 HIP alloy produced at IMT, and rolled into flat strips at the Army Materials and Mechanics Research Agency.

As a preliminary step to the experiments on stress corrosion cracking, the compliance of the crack-line loaded wedge specimen was measured for several crack lengths. The resulting curve relating the crack length to extensometer output is shown in Fig. 21.

151

References Part I

- (1) Muskhelishvili, N. I., Some Basic Problems of the Mathematical Theory of Elasticity, P. Noordhoff. Ltd., Groningen, The Netherlands, p. 355, (1963).
- (2) Rhee, S. S., and F. A. McClintock, "On the Effects of Strain Hardening on Strain Concentrations" Proc. 4th U. S. National Congress of Applied Mechanics. A.S.M.E. New York, p. 1007, (1962).
- (3) Im, J., "Inclusion Separation in Plastic Deformation," S. M. Thesis, Mechanical Engineering Department, M.I.T., (1967).
- (4) Ashby, M. F., Phil. Mag., 14, 1157, (1966).
- (5) Bridgman, P. W., Studies in Large Plastic Flow and Fracture, McGraw-Hill, New York, Chapter 1, (1952).
- (6) Neuber, H., Theory of Notch Stresses, T. W. Edwards Ann Arbor, Michigan, pp. 84-89, (1946).
- (7) Clausen, D. P., A.S.M. Trans, V60, N3 504, (1967).
- (8) Norris, K. C., "Strain in Neck of a Tensile Specimen," S. M. Thesis, Department of Mechanical Engineering, M.I.T., (1967).
- (9) Brenner, S. S., "Properties of Whiskers," Growth and Perfection of Crystals, T. Wiley, New York, p. 157, (1958).
- (10) McClintock, F. A., and W. O'Day, "Biaxial Tension, Distributed Cores, and Fracture in Bubble Rafts," Proc. 1st Intern. Conf. Fracture (Sendai) Yokobori, et. al. editors, Japan. Soc. Strength Fracture Materials, I., 75, (1966).

152

References Part II

11. "Fracture Toughness of High Strength Materials: Theory and Practice", ISI Publication 120, The Iron and Steel Institute, London, U.K., 1970.
12. "Fracture Toughness", ISI Publication 121, The Iron and Steel Institute, London, U.K.
13. "Fracture Toughness Testing and Its Applications", STP 381, ASTM, Philadelphia, Pa., 1965.
14. Brown, W. F. Jr., and J. E. Srawley: "Plane Strain Crack Toughness Testing of High Strength Metallic Materials", STP 410, ASTM, Philadelphia, Pa., 1966.
15. Brown, W. F. Jr., Ed.: "Review of Developments in Plane Strain Fracture Toughness Testing", STP 463, ASTM, Philadelphia, Pa., 1970.
16. Gross, B., J. E. Srawley and W. F. Brown, Jr.: "Stress-Intensity Factors for a Single-Edge-Notch Tension Specimen by Boundary Collocation of a Stress Function", NASA TN D-2395, 1964.
17. Gross, B., and J. E. Srawley: "Stress Intensity Factors by Boundary Collocation for Single-Edge-Notch Specimens Subject to Splitting Forces", NASA TN D-3295, 1966.
18. Srawley, J. E., and B. Gross: "Stress Intensity Factors for Crackline-Loaded Edge-Crack Specimens", NASA TN D-3820, 1967.
19. Wessel, E. T.: "State of the Art of the WOL Specimen for K_{IS} Fracture Toughness Testing", Eng. Frac. Mech., Vol. 1, pp. 77-103, 1968.
20. Ripling, E. J., S. Mostovoy and P. B. Crosley: "Use of Crackline-Loaded Specimens for Measuring Plane Strain Fracture Toughness", Materials Research Lab., Inc., Richton Park, Ill.

153

**Table I Tensile Behavior of Commercial
Maraging Vascomax 300 Alloy and Maraging
300-HIP Alloy Prepared by IMT**

Vascomax 300

	Y	TS	σ_0	n	$\frac{d\sigma}{d\epsilon}$	ϵ_0
	ksi	ksi	ksi		ksi	
Unaged	116	150	200	0.12	77	0.023
Aged	117	188	255	0.12	98	0.063

Maraging 300-HIP

Unaged	110	143	200	0.10	59	0.020
Aged	11	178	250	0.10	60	0.082

154

Table II Experimental Data on the
Unaged Vascomax 300 Material with Special
Neck Profiles

Spec. No	R_o	a_o	R	a	$(\frac{a}{R})$	Red. Area	$(\sigma_T/Y)_f$	ϵ_f
	in.	in.	in.	in.				
1	0.125	0.125	0.068	0.073	1.070	0.660	0.762	1.09
2	0.250	0.125	0.098	0.071	0.725	0.678	0.643	1.15
3	0.500	0.125	0.112	0.069	0.615	0.695	0.601	1.15
4	1.250	0.125	0.182	0.065	0.357	0.730	0.497	1.32
	∞	0.125	0.082	0.067	0.817	0.713	0.675	1.24

Table III Experimental Data on the
Aged Vascomax 300 Material with Special
Neck Profiles

Spec. No	R_o	a_o	R	a	$(\frac{a}{R})$	Red Area	$(\sigma_T/Y)_f$	ϵ_f
	in.	in.	in.	in.				
5	0.125	0.125	0.101	0.110	1.09	0.226	0.768	0.258
6	0.250	0.125	0.112	0.104	0.93	0.307	0.715	0.368
7	0.500	0.125	0.134	0.095	0.71	0.430	0.637	0.549
8	1.250	0.125	0.164	0.088	0.54	0.505	0.572	0.700
	∞	0.125	0.208	0.087	0.42	0.516	0.524	0.725

155

Table IV Data on Hole Nucleation in the
Unaged Vascomax 300 Material with Special
Neck Profiles

Spec. No	$(\frac{a}{R})_o$	$(\frac{a}{R})_f$	z_n in.	$(\sigma_T/Y)_n$	$\bar{\epsilon}_n$	$Y(\bar{\epsilon}_n)$ ksi	$\sigma_{rr}-\sigma_T$ ksi	σ_{rr} ksi
1	1.00	1.07	0.045	0.477	0.844	218	251	351
2	6.50	0.73	0.080	$\sim 1/3$	0.660	202	233	303
3	0.25	0.62	0.094	$\sim 1/3$	0.660	202	233	303
4	0.10	0.36	0.088	$\sim 1/3$	0.844	218	251	321

Table V Data on Hole Nucleation in the
Aged Vascomax 300 Material with Special
Neck Profiles

Spec. No	$(\frac{a}{R})_o$	$(\frac{a}{R})_f$	z_n in.	$(\sigma_T/Y)_n$	$\bar{\epsilon}_n$	$Y(\bar{\epsilon}_n)$ ksi	$\sigma_{rr}-\sigma_T$ ksi	σ_{rr} ksi
5	1.00	1.09	0.069	0.484	0.172	206	238	338
6	0.50	0.93	0.056	0.513	0.176	206	238	344
7	0.25	0.71	0.094	$\sim 1/3$	0.177	206	238	307
8	0.10	0.54	0.106	$\sim 1/3$	0.246	212	245	316

156

Table VI Experimental Data on the
Unaged Maraging 300-HIP Alloy with Large, Hollow
Inclusions and Natural Neck Profiles

Spec. No	R_o in.	a_o in.	R in.	a in.	$(\frac{a}{R})_f$	Red. Area	$(\frac{\sigma_T}{Y})_f$	ϵ_f
1	1.000	0.100	0.0343	0.048	1.400	0.770	0.863	1.464
2	0.400	0.100	0.0375	0.051	1.36	0.740	0.852	1.346
3	0.200	0.100	0.0450	0.057	1.268	0.686	0.817	1.159
4	0.100	0.100	0.0332	0.055	1.718	0.675	0.953	1.122
	∞	0.100	0.0435	0.049	1.128	0.760	0.780	1.408

Table VII Experimental Data on the
Aged Maraging 300-HIP Alloy with Large, Hollow
Inclusions and Natural Neck Profiles

Spec. No.	R_o in.	a_o in.	R in.	a in.	$(\frac{a}{R})_f$	Red. Area	$(\frac{\sigma_T}{Y})_f$	ϵ_f
1	1.000	0.100	0.058	0.061	1.05	0.628	0.755	0.989
2	0.400	0.100	0.064	0.067	1.05	0.550	0.755	0.799
3	0.200	0.100	0.069	0.073	1.06	0.369	0.759	0.629
4	0.100	0.100	0.056	0.075	1.34	0.339	0.846	0.575
	∞	0.100	0.072	0.066	0.92	0.565	0.711	0.831

157

Table VIII Nucleation and Growth
Strains of Holes Leading to Ductile Fracture in
Maraging Vascomax 300

Unaged (n=0.12)					
Spec. No.	ϵ_f	ϵ_n	ϵ_g	$\frac{\sigma_T}{Y}$	$\ln\left(\frac{a}{2r_0}\right) = \frac{\epsilon_g \sinh[(1-n)(\sigma_T/Y)]}{(1-n)}$
1	1.090	0.844	0.246	0.762	0.201
2	1.150	0.660	0.490	0.643	0.326
3	1.190	0.660	0.530	0.601	0.334
4	1.320	0.844	0.476	0.497	0.245
Aged (n=0.12)					
Spec. No.	ϵ_f	ϵ_n	ϵ_g	$\frac{\sigma_T}{Y}$	$\ln\left(\frac{a}{2r_0}\right) = \frac{\epsilon_g \sinh[(1-n)(\sigma_T/Y)]}{(1-n)}$
5	0.258	0.170	0.086	0.768	0.071
6	0.368	0.176	0.192	0.715	0.147
7	0.549	0.177	0.372	0.637	0.250
8	0.700	0.246	0.454	0.572	0.270

158

Figure Captions Part I

- Fig. 1 Idealization of plastic behavior by non-hardening and linearly hardening behavior.
- Fig. 2 Plastic accommodation around a rigid spherical particle.
- Fig. 3 Plastic accommodation of incompatibilities around a rigid inclusion embedded into: (a) a non-hardening matrix, (b) a linearly hardening matrix with finite yield strength.
- Fig. 4 Plastic accommodation between two interacting large particles.
- Fig. 5 Changes of neck profiles with deformation in a tension specimen.
- Fig. 6 Shape of pre-machined, notched Vascomax 300 specimens.
- Fig. 7 Stress strain curves of: (a) Vascomax 300; Maraging 300 HIP alloy (b) 1st bar with large hollow inclusions, (c) 2nd bar without large inclusions.
- Fig. 8 Deformation transients in an unaged Vascomax 300 specimen during interrupted loading.
- Fig. 9 Fracture surface profile of Specimen #1 of Vascomax 300 alloy showing both the large titanium-carbide inclusions, and much smaller inclusions.
- Fig. 10 Fracture surface profile of specimen #5 of Vascomax 300 alloy, showing only large titanium carbide inclusions, and an axial crack.
- Fig. 11 Fracture surface profile and two types of inclusions in unaged Maraging 300-HIP alloy from 1st bar. Note the three large hollow inclusions.
- Fig. 12 Fracture surface profile and two types of inclusions in aged Maraging 300-HIP alloy from 1st bar.

Fig. 13 Inhomogeneities in Maraging 300-HIP alloy from 1st bar.

Fig. 14 Premature ductile fracture in an inhomogeneity band in the aged Maraging 300-HIP alloy from the 1st bar.

Fig. 15 Another area from same specimen shown in Fig. 14.

Fig. 16 Cumulative number of separated inclusions along an axial scan in unaged Vascomax 300 specimens with different initial machined neck profiles.

Fig. 17 Cumulative number of separated inclusions along an axial scan in aged Vascomax 300 specimens with different initial machined neck profiles.

Fig. 18 Ductile fracture surface of Vascomax 300 aged Specimen #7. Showing two types of ductile fracture dimples.

Fig. 19 Larger magnification view of the smaller ductile fracture dimples shown in Fig. 18.

160

Figure Captions Part II

Fig. 19 Specimen chosen for the stress corrosion cracking measurements.

Fig. 20 Experimental apparatus showing (a) the specimen; (b) the LVDT extensometer; (c) the load cell; (d) two arms of the scissor shaped test frame.

Fig. 21 Compliance of the crack-line loaded specimen.

161

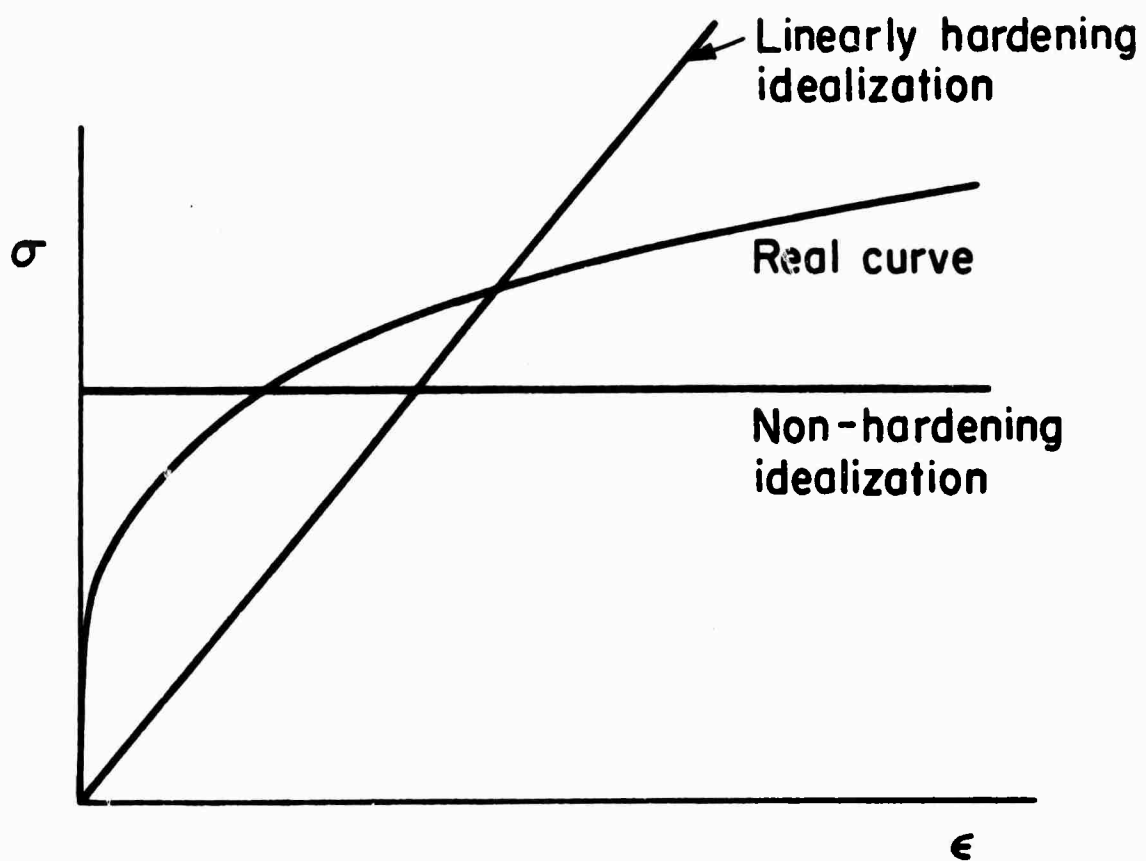
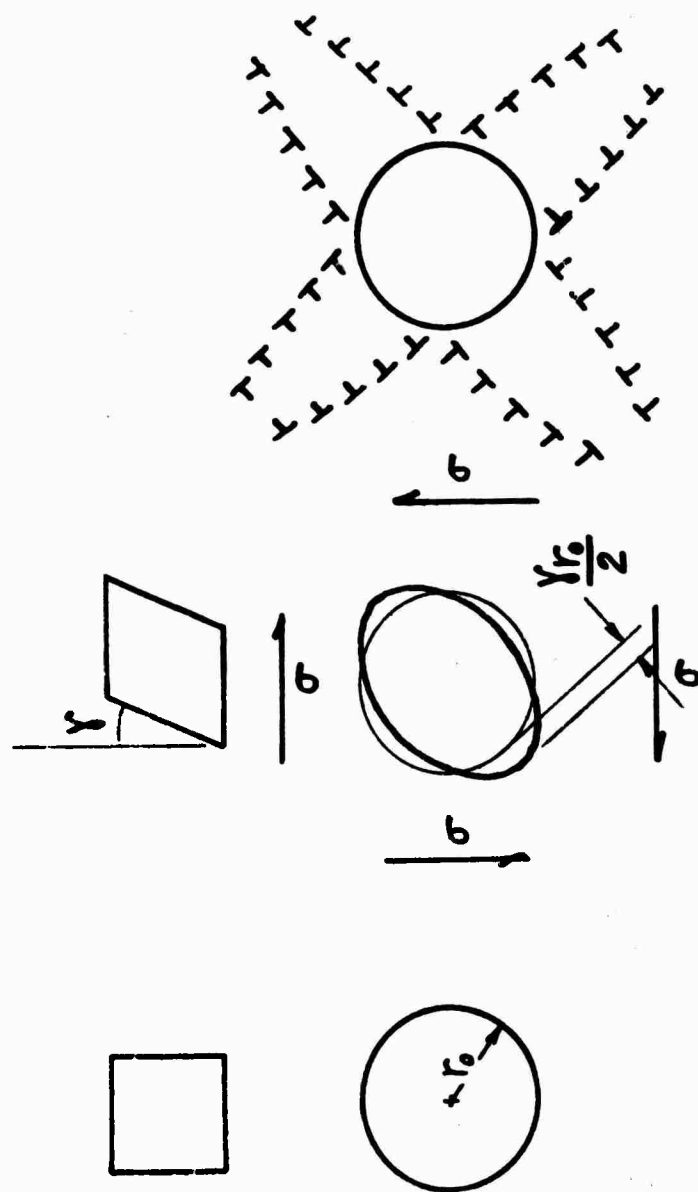


Fig. 1 Idealization of plastic behavior by non-hardening and linearly hardening behavior.

162



163

Fig. 2 Plastic accommodation around a rigid spherical particle.

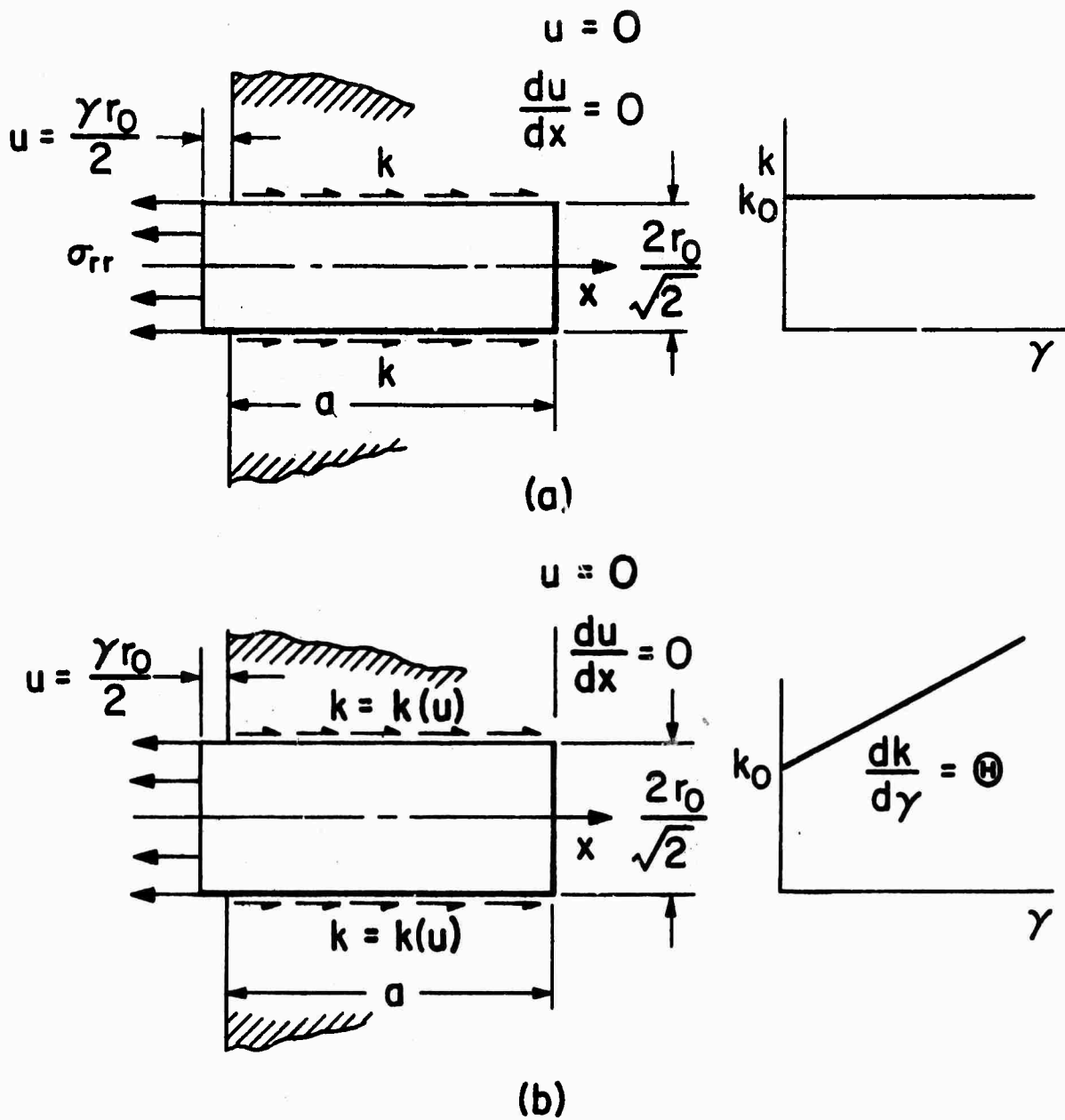
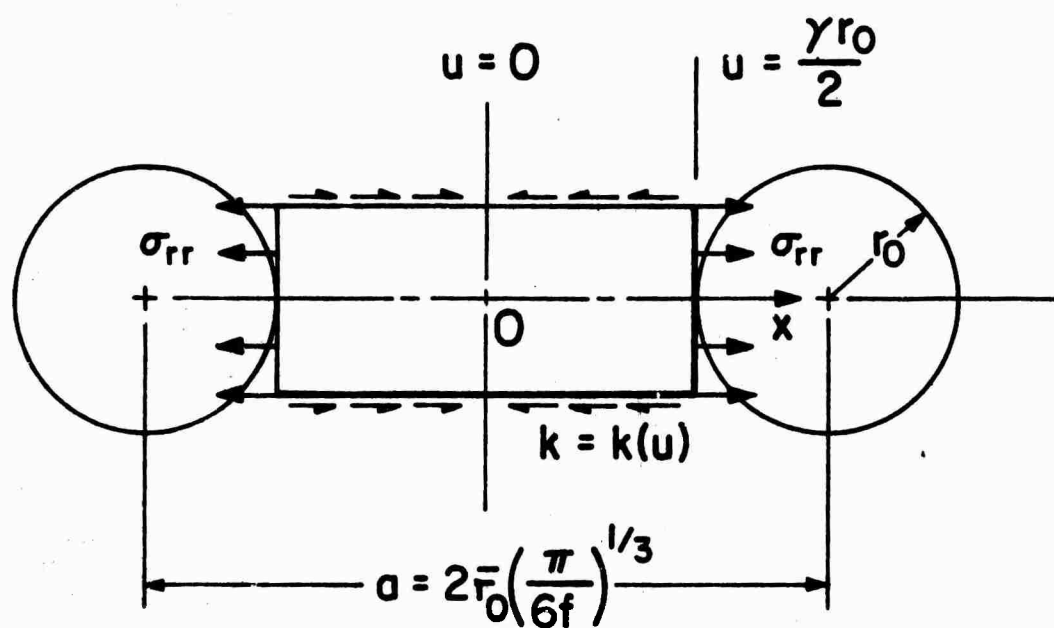
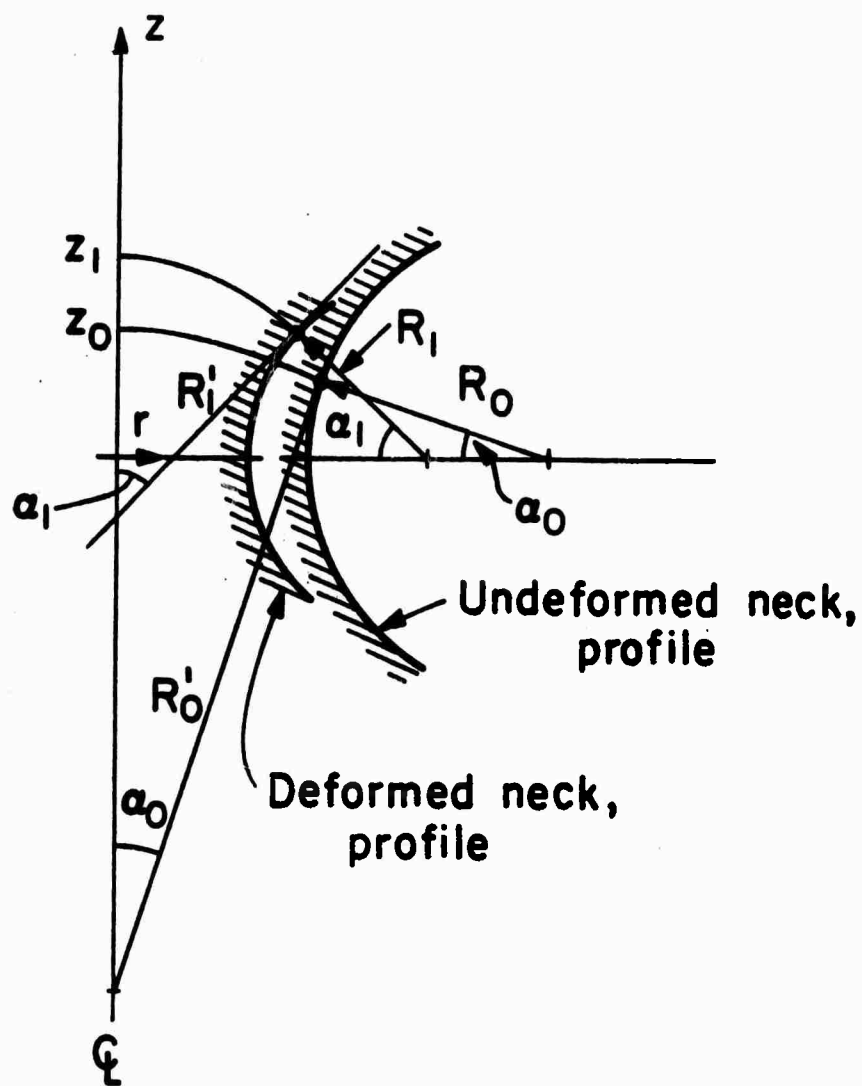


Fig. 3 Plastic accommodation of incompatibilities around a rigid inclusion embedded into: (a) a non-hardening matrix, (b) a linearly hardening matrix with finite yield strength.



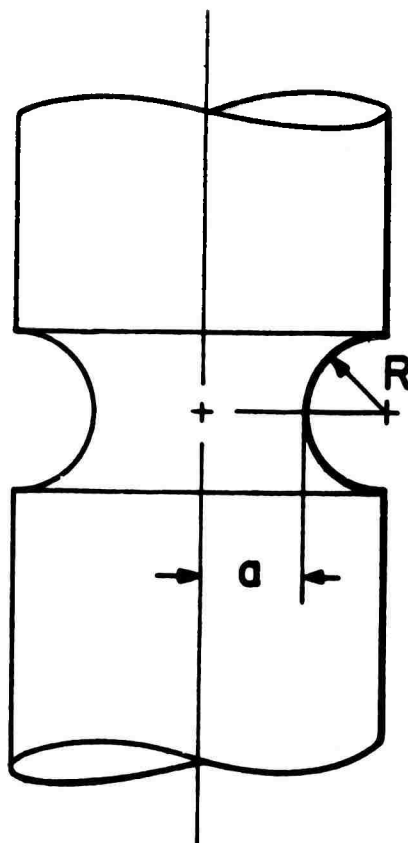
165

Fig. 4 Plastic accommodation between two interacting large particles.



166

Fig. 5 Changes of neck profiles with deformation in a tension specimen.



167

Fig. 6 Shape of pre-machined, notched Vascomax 300 specimens.

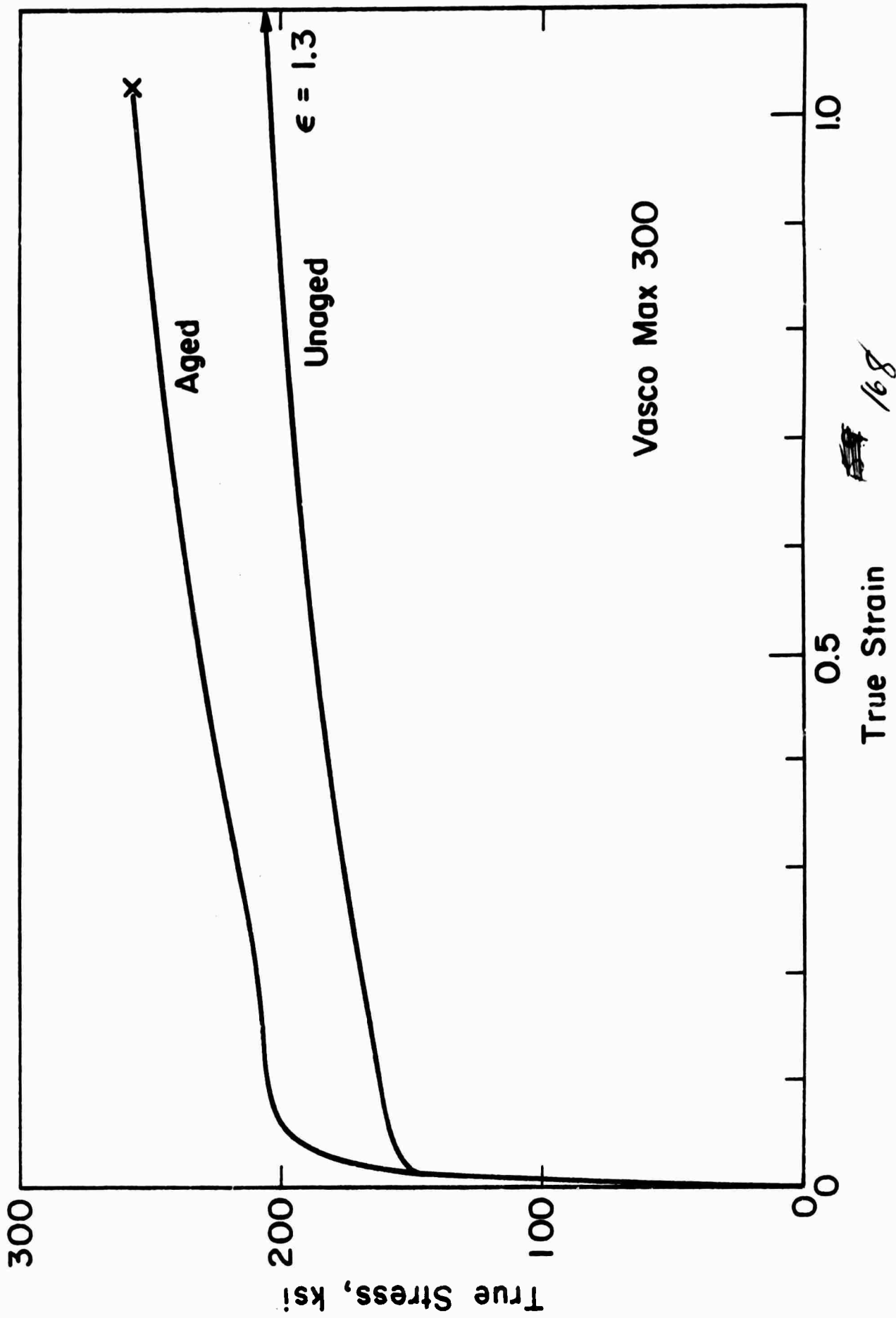
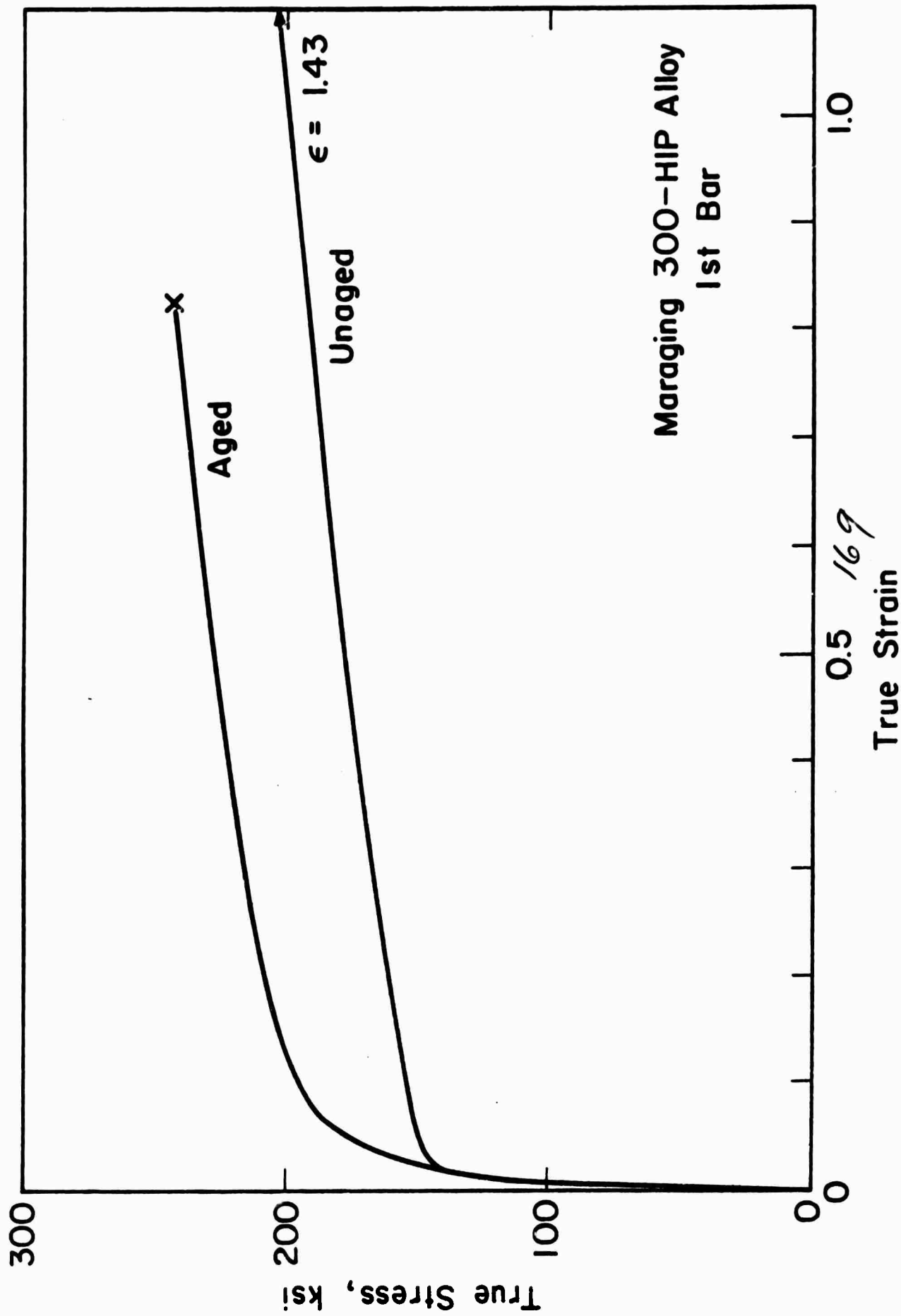
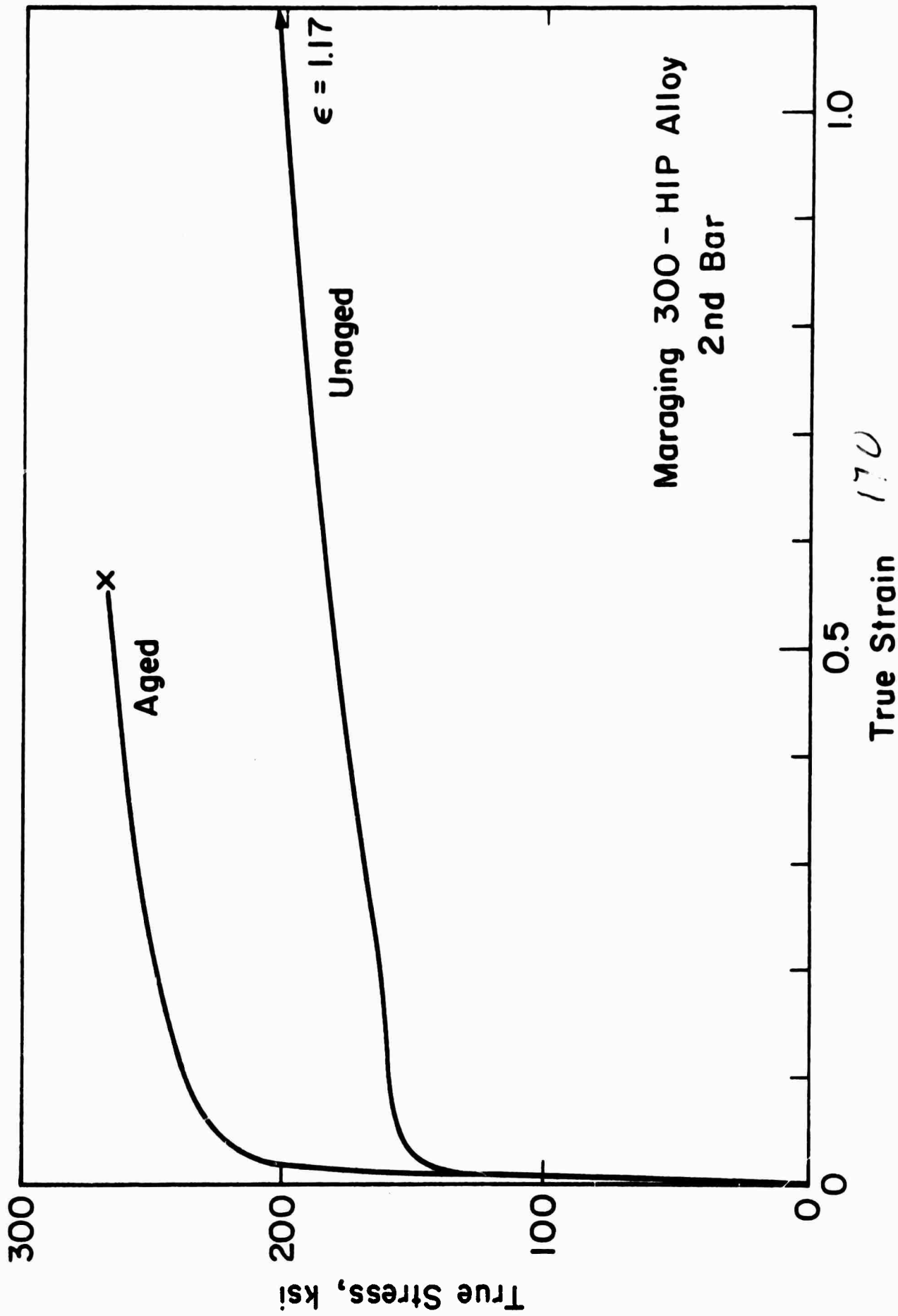


Fig. 7 Stress strain curves of: (a) Vascomax 300; (b) 1st bar with large hollow inclusions, (c) 2nd bar without large inclusions.





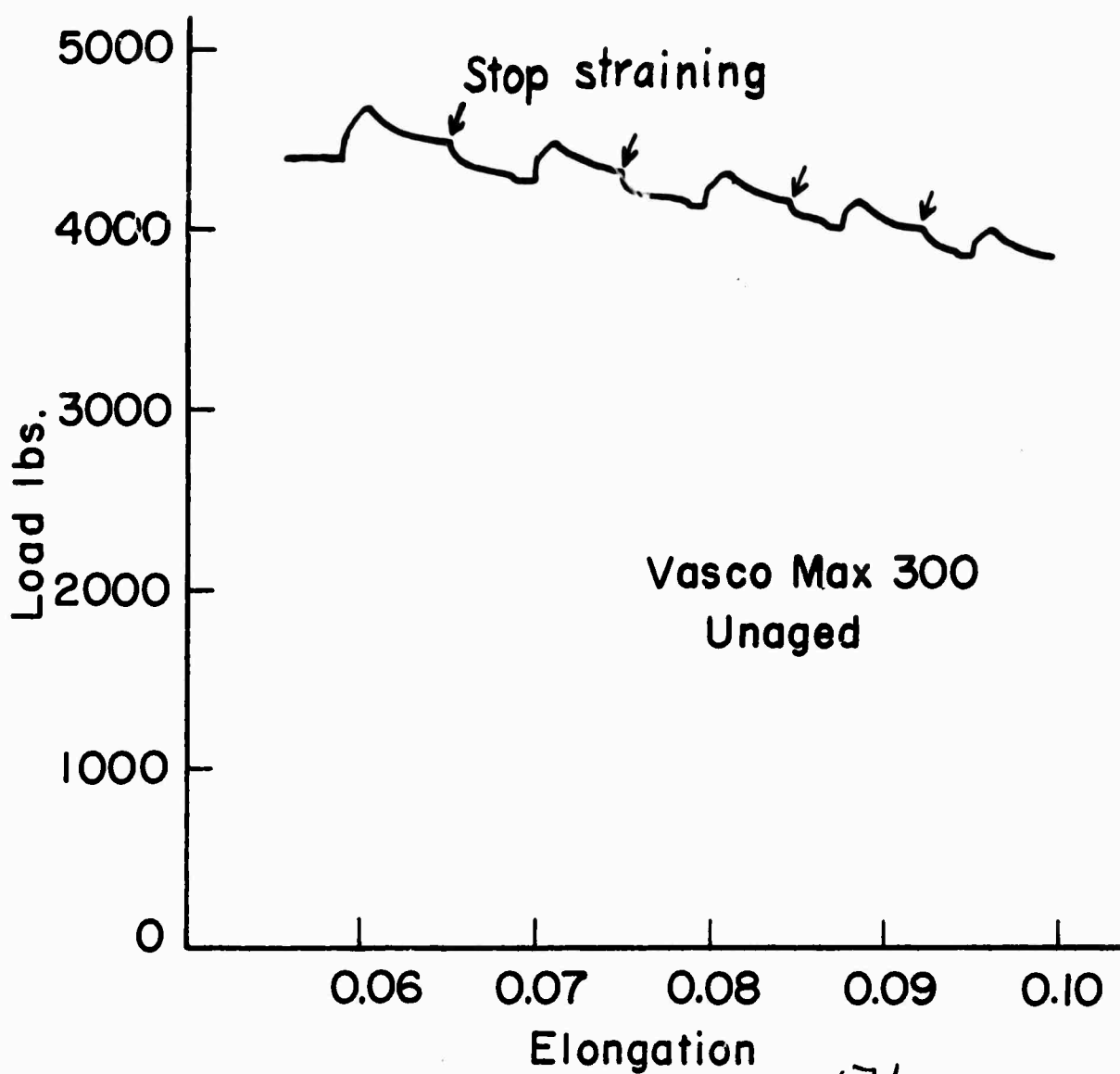


Fig. 8 Deformation transients in an unaged VascoMAX 300 specimen during interrupted loading.

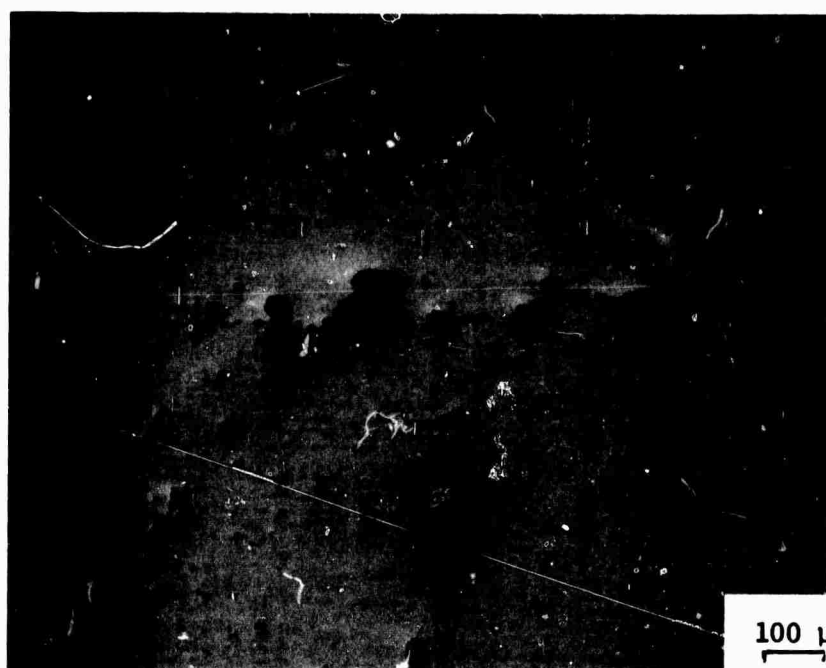


172

Fig. 9 Fracture surface profile of Specimen #1 of Vascom3x 300 alloy showing both the large titanium-carbide inclusions, and much smaller inclusions.



Fig. 10 Fracture surface profile of specimen #5 of Vascomax 300 alloy, showing only large titanium carbide inclusions, and an axial crack.



173

Fig. 11 Fracture surface profile and two types of inclusions in unaged Maraging 300-HIP alloy from 1st bar. Note the three large hollow inclusions.

-169-

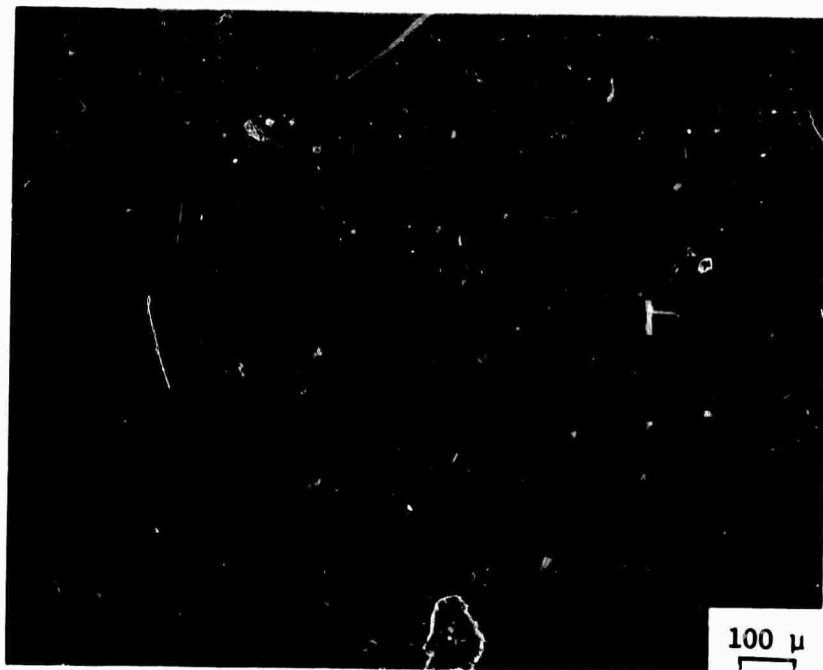
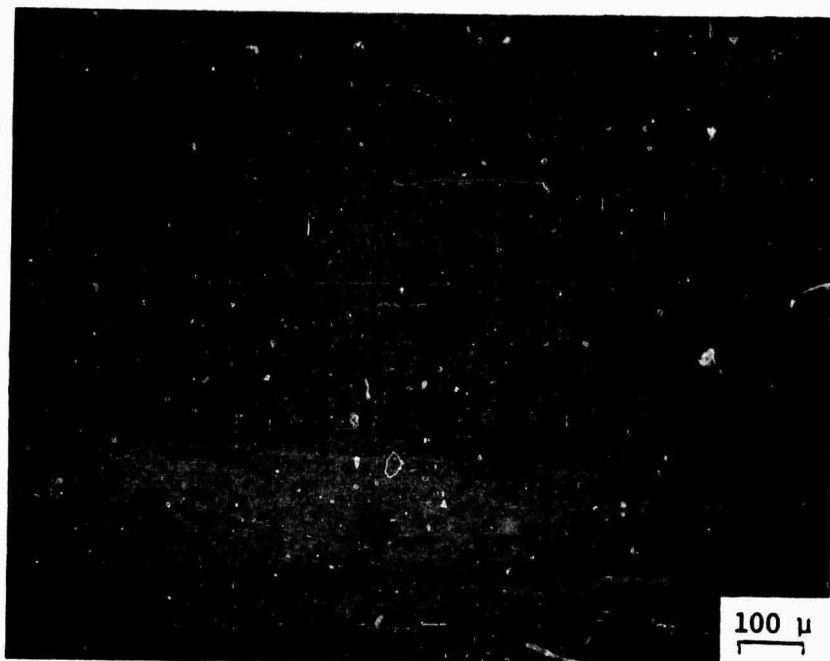


Fig. 12 Fracture surface profile and two types of inclusions in aged Maraging 300-HIP alloy from 1st bar.



174
Fig. 13 Inhomogeneities in Maraging 300-HIP alloy from 1st bar.

-165-

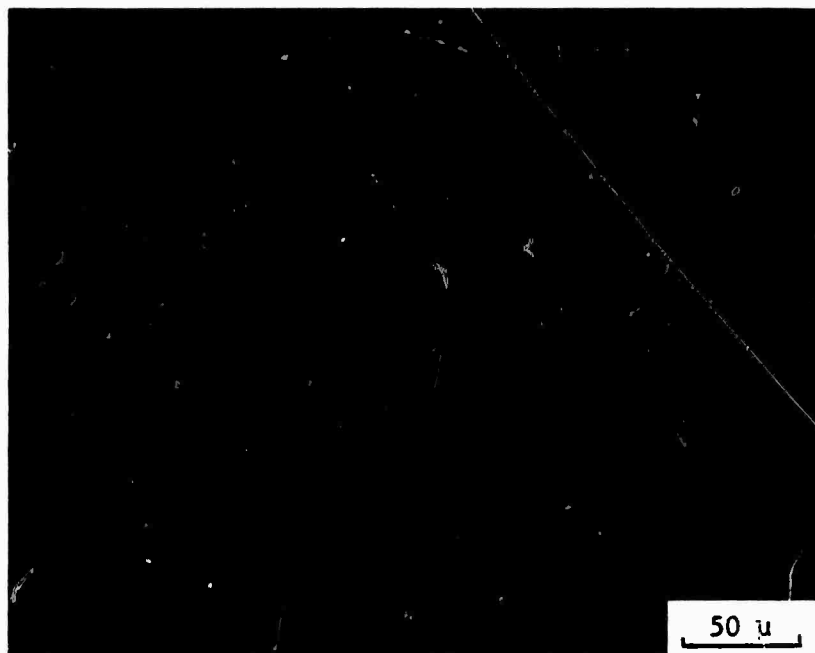
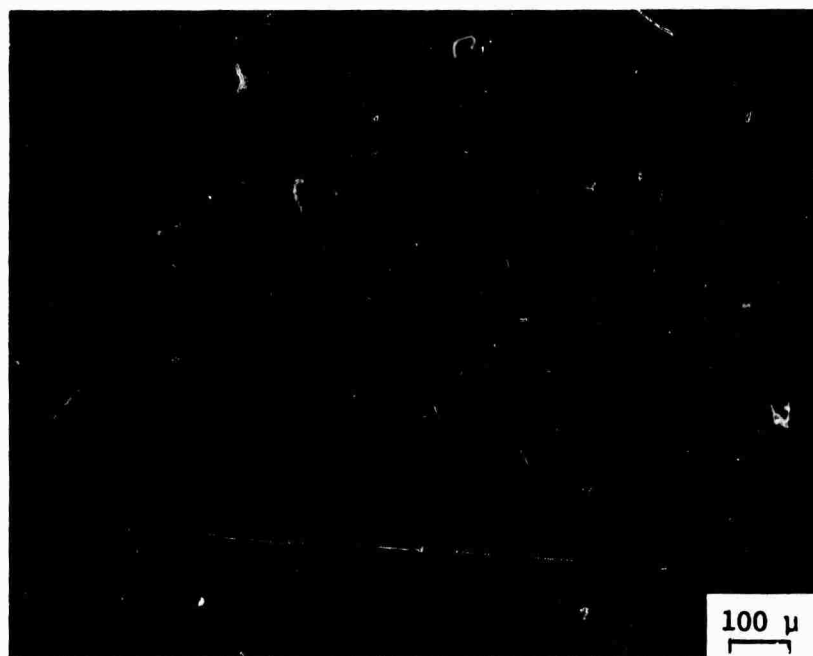


Fig. 14 Premature ductile fracture in an inhomogeneity band in the aged Maraging 300-HIP alloy from the 1st bar.



175

Fig. 15 Another area from same specimen shown in Fig. 14.

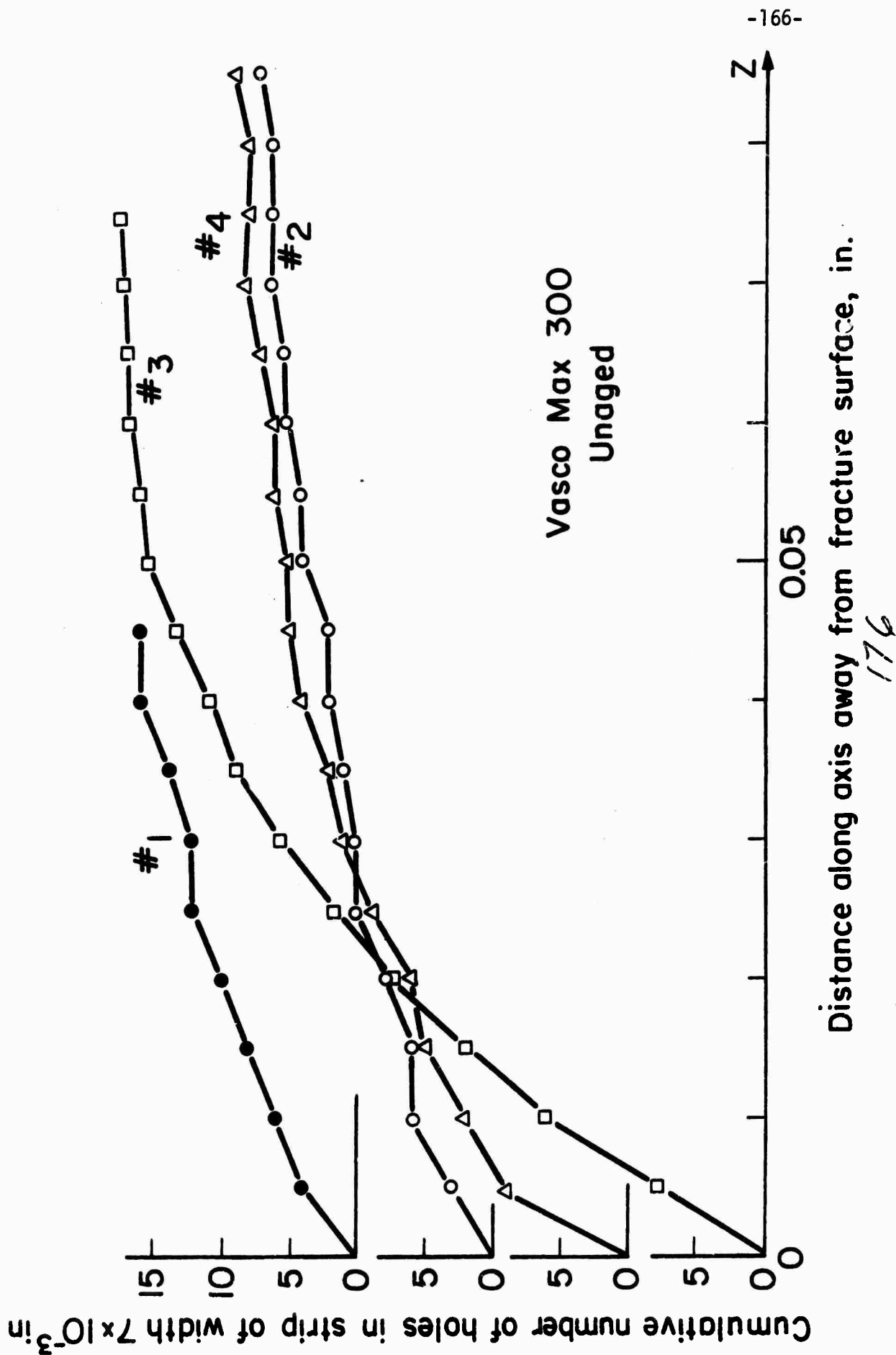


Fig. 16 Cumulative number of separated inclusions along an axial scan in unaged Vascomax 300 specimens with different initial machined neck profiles.

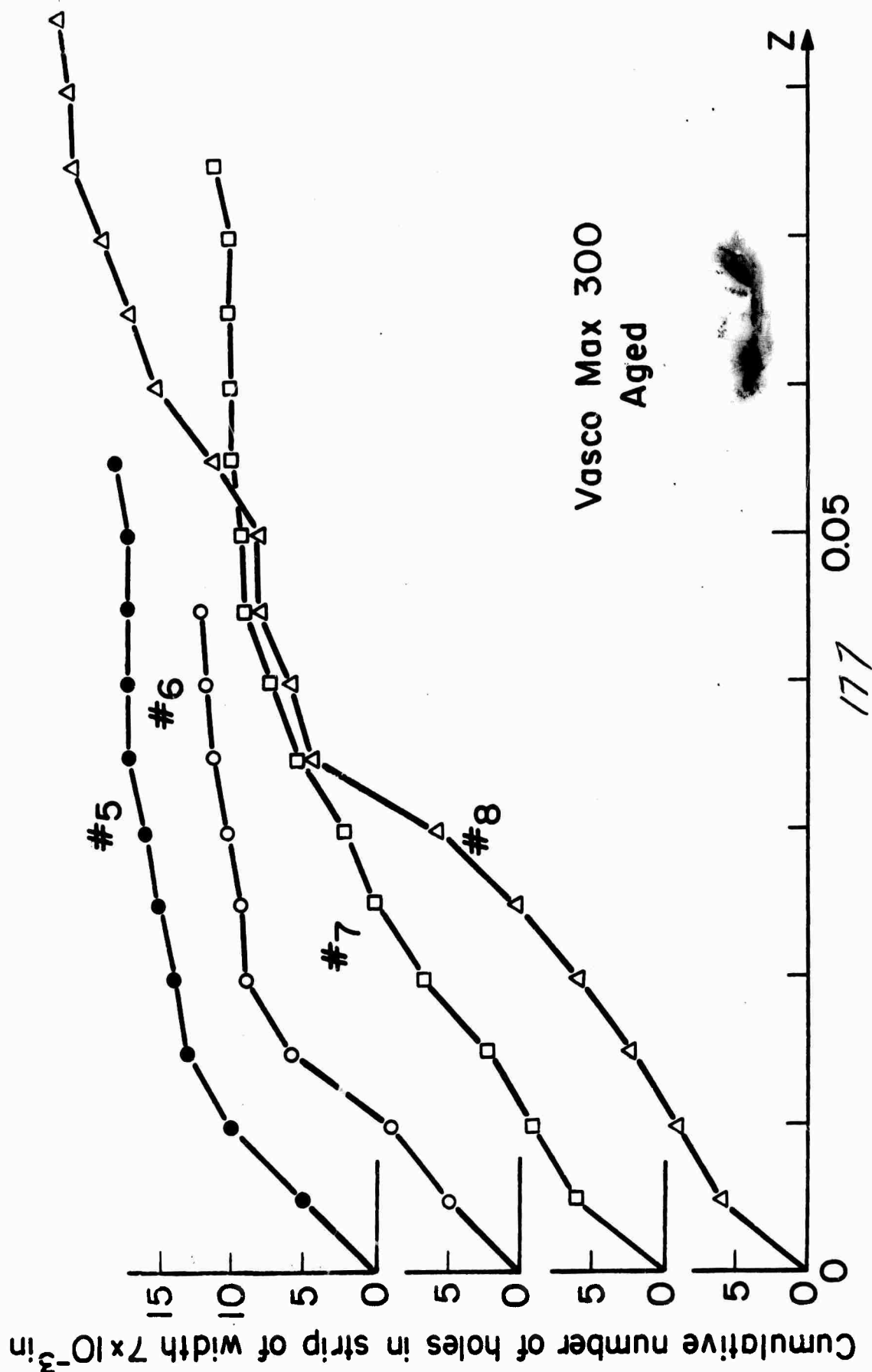
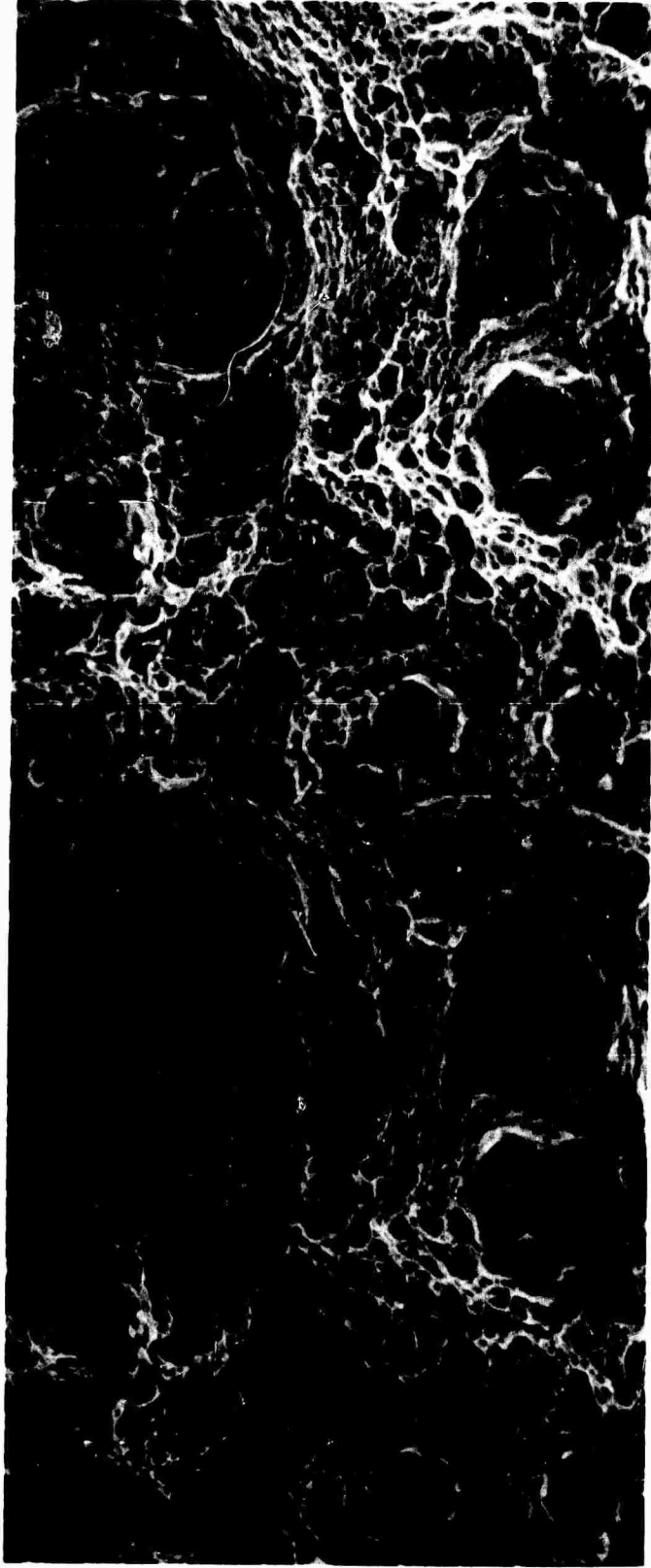


Fig. 17 Cumulative number of separated inclusions along an axial scan in aged Vascomax 300 specimens with different initial machined neck profiles.

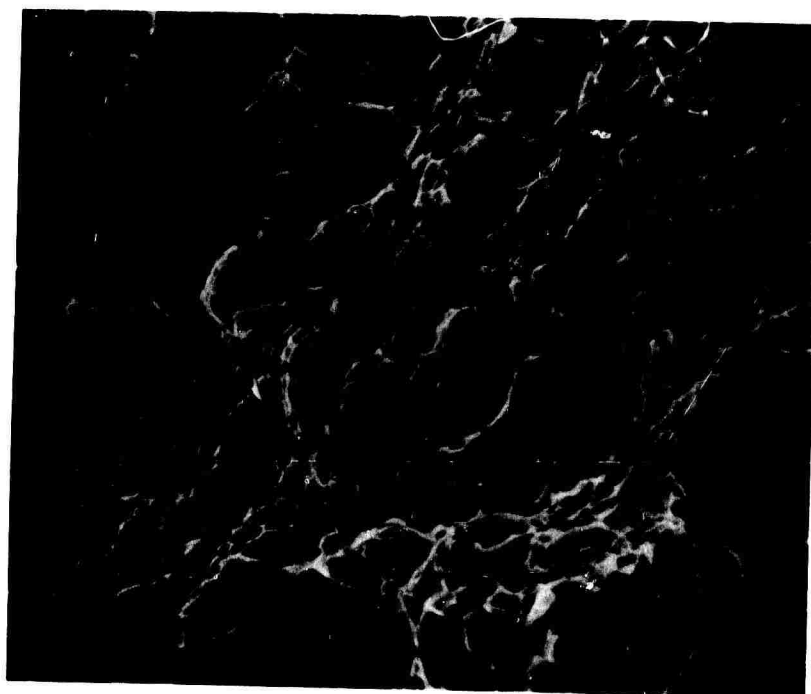


511

178

Fig. 18 Ductile fracture surface of Vascomax 300 aged Specimen #7. Showing two types of ductile fracture dimples.

-169-



5μ

179

Fig. 19 Larger magnification view of the smaller ductile fracture dimples shown in Fig. 18.

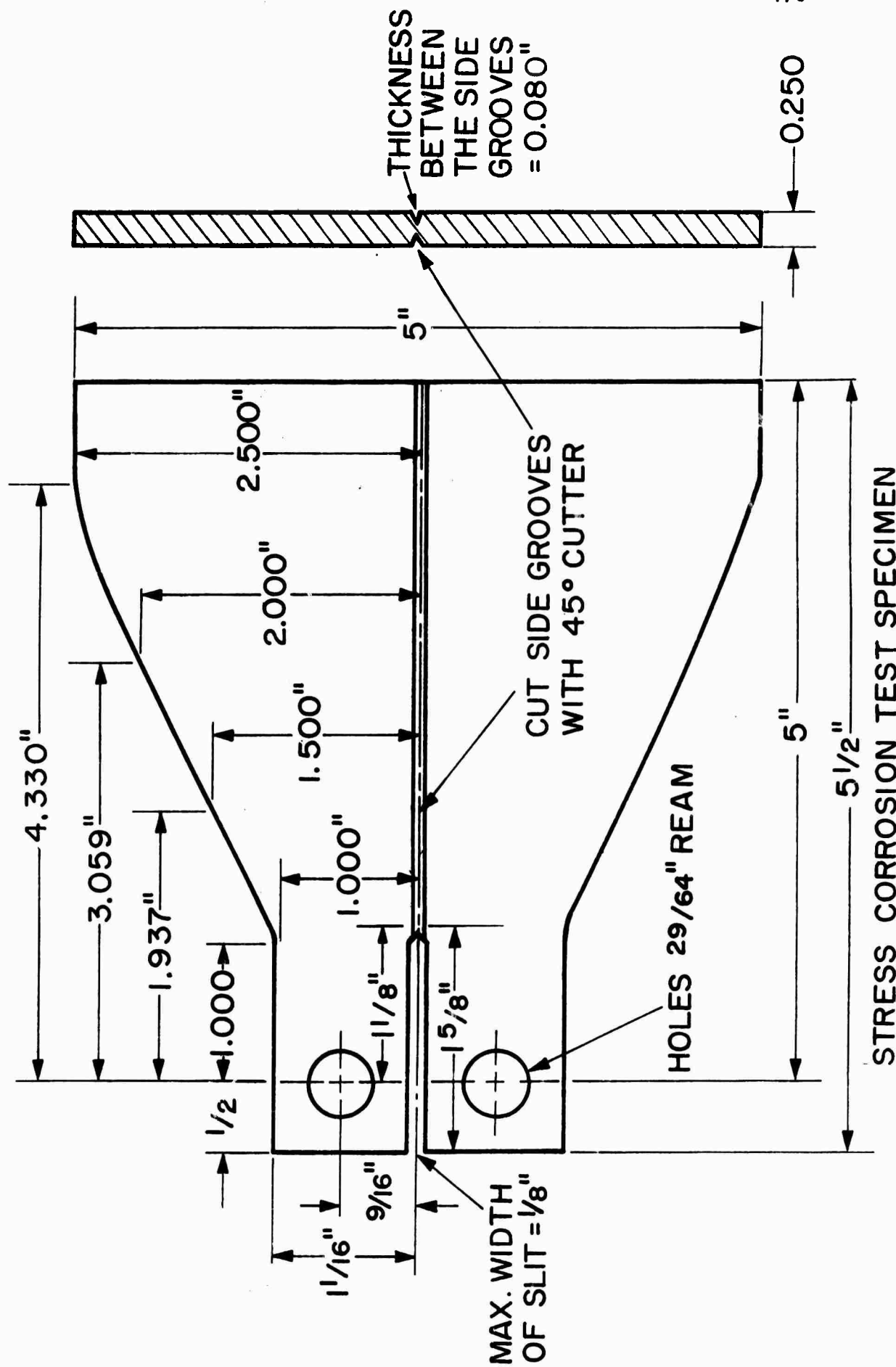


Fig. 19b Specimen chosen for the stress corrosion cracking measurements.

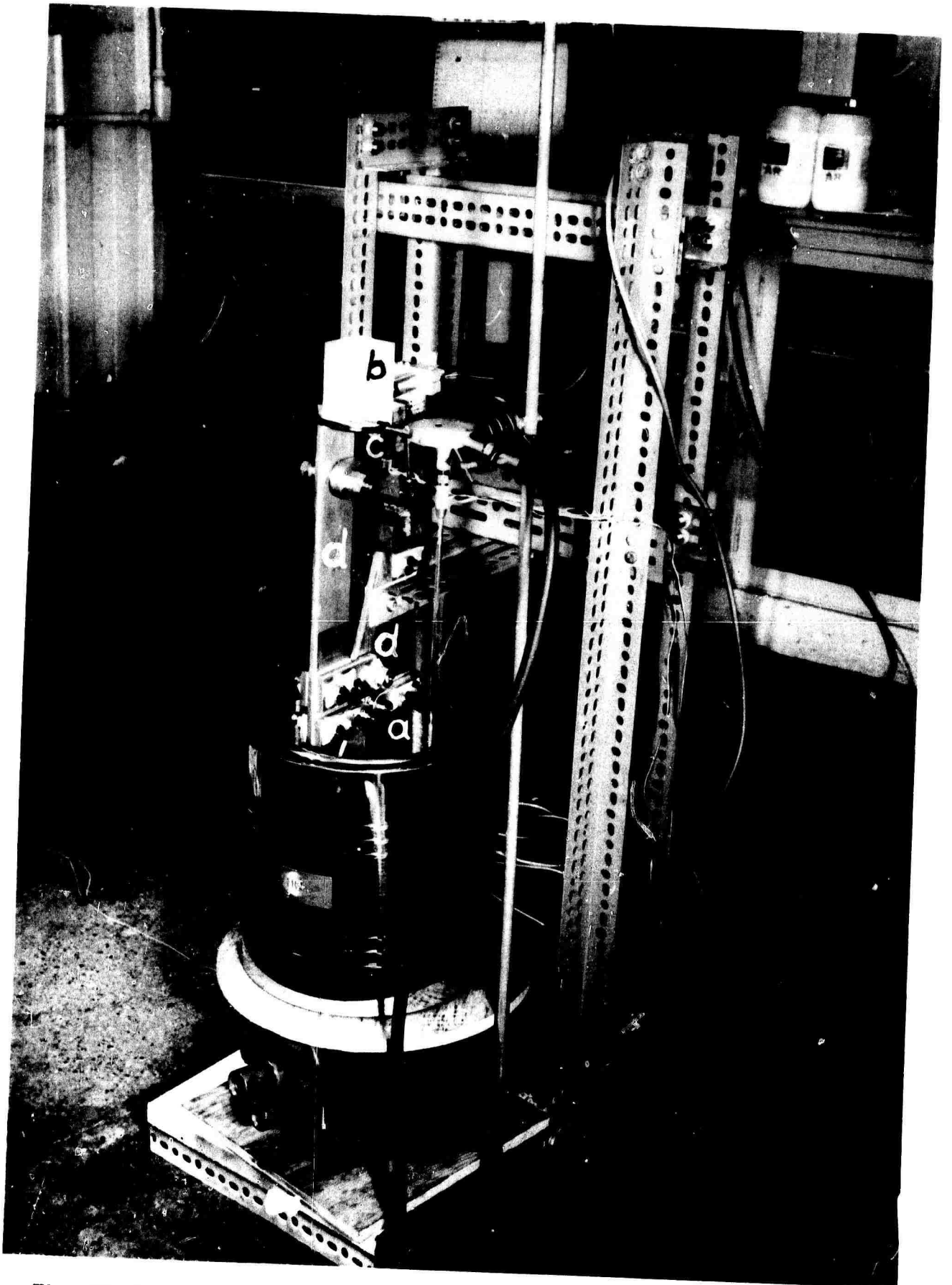


Fig. 20 Experimental apparatus showing (a) the specimen; (b) the LVDT extensometer; (c) the load cell; (d) two arms of the scissor shaped test frame.

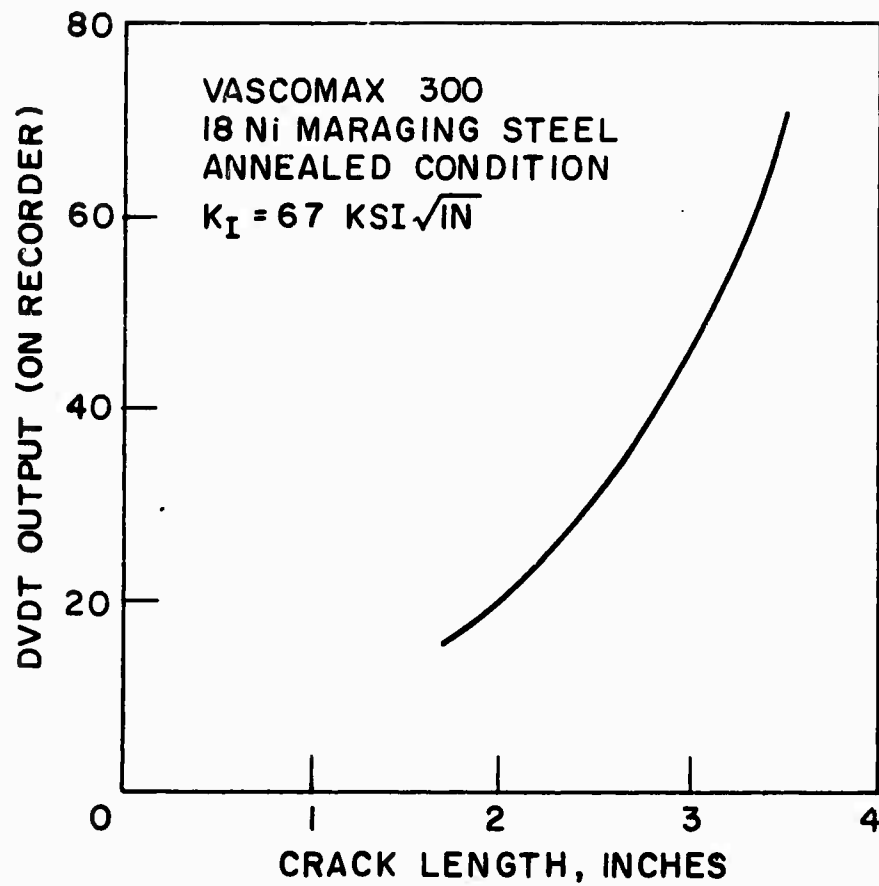


Fig. 21 Compliance of the crack-line loaded specimen.

189